ANNUAL REPORT 2004

Optoelectronics Department

University of Ulm

Contents

Preface 1

Articles

Lensed Top-Emitting VCSELs 3

High-Power VCSELs With One Preferred Polarization 9

M^2 Measurements of High-Power VCSELs 17

2-D 850 nm VCSEL Arrays With Redundant Pixel Designs 21

High-Performance Low-Cost Optical Link at 850 nm 27

40 Gbit/s Operation of Laser-Integrated Electroabsorption Modulator 31

Investigation of the Capacitance of Integrated DFB–EAMs 37

HVPE of Thick GaN 41

GaN FACELO Structures With Marker Layers 45

Epitaxial Growth of AlGaN Layers 51

InGaN QWs Grown on Facets 55

Longitudinal Mode Patterns in GaInN Lasers 59

MBE Growth of GaNAs and AlGaNAs Layers 65

Strain Compensated Disk Lasers Structures 71

Semiconductor Disk Laser on Microchannel Cooler 79

Optimization of Process Parameters for Low-Absorbing Optical Coatings 85

External-Cavity Tapered Semiconductor Ring Lasers 91

Lists of Publications

Ph.D. Theses 97

Diploma and Master Theses 98

Semester Projects 100

Talks 101

Publications and Conference Contributions 103

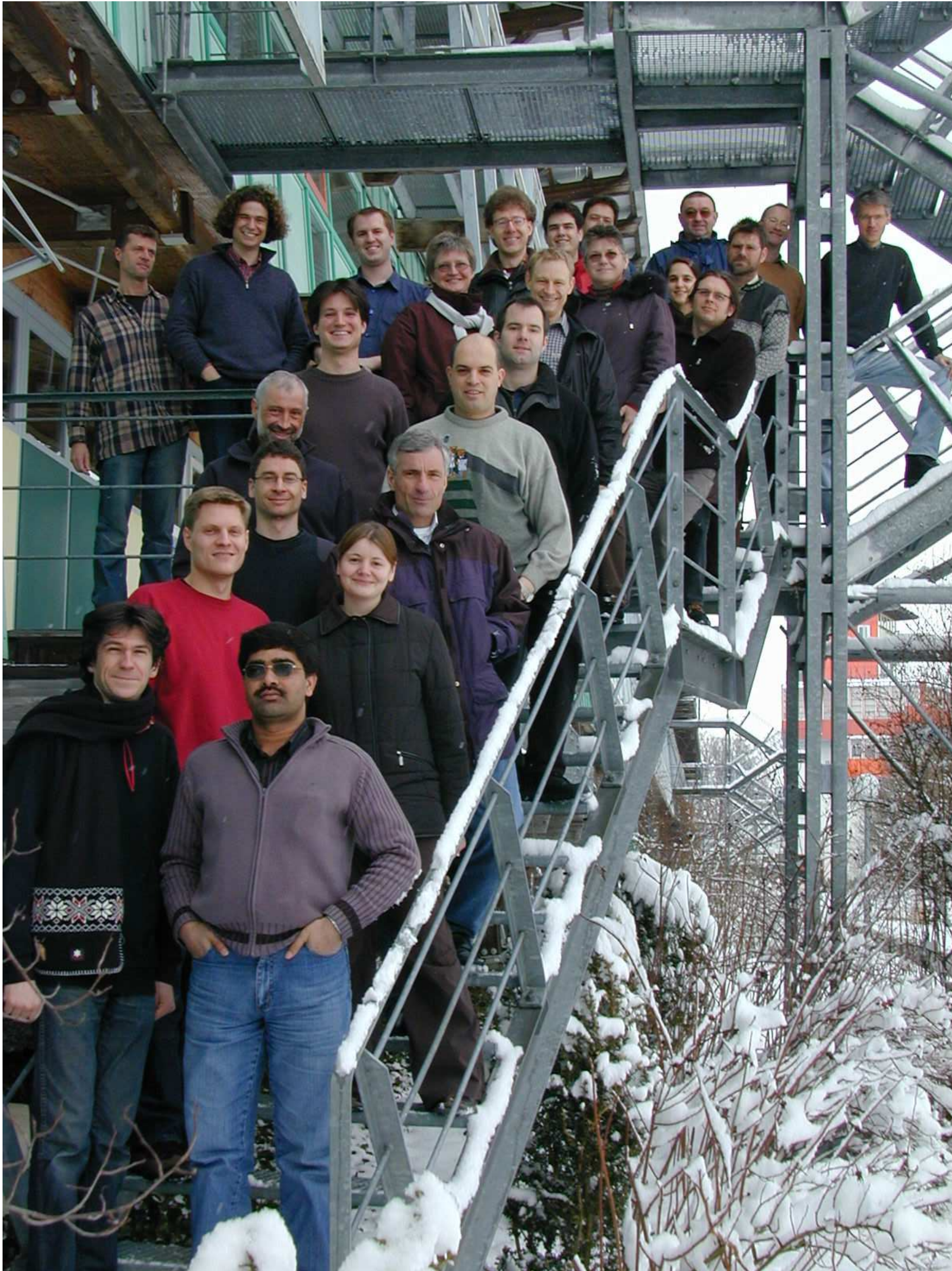

1: Rainer Blood
2: Johannes M. Ostermann
3: Peter Brückner
4: Martin Stach
5: Frank Habel
6: Christoph Kirchner
7: Josef Theisz
8: Jürgen Mähnß
9: Rainer Michalzik
10: Hildegard Mack
11: Hendrik Roscher
12: Gerlinde Meixner
13: Barbara Neubert
14: Peter Unger
15: Frank Demaria
16: Philipp Gerlach
17: Steffen Lorch
18: Rudolf Rösch
19: Ihab Kardosh
20: Eckart Gerster
21: Ferdinand Scholz
22: Michael C. Riedl
23: Andrea Kroner
24: Fernando Rinaldi
25: Manmohan S. Shishodia

Missing in the picture

26: Christine Bunk
27: Karl J. Ebeling
28: Daniel Hofstetter
29: Sükran Kilic
30: Susanne Menzel
31: Georgi Stareev

Optoelectronics Department University of Ulm

Albert-Einstein-Allee 45, D-89081 Ulm, Germany
URL: http://www-opto.e-technik.uni-ulm.de
Fax: +49–731/50–2 60 49
Phone: +49–731/50–

Head of Department			
Prof. Dr.	Peter Unger	–2 60 54	peter.unger@uni-ulm.de
Deputy Head			
Prof. Dr.	Ferdinand Scholz	–2 60 52	ferdinand.scholz@uni-ulm.de
President of the University of Ulm			
Prof. Dr.	Karl Joachim Ebeling	–2 60 51	karl.ebeling@uni-ulm.de
Senior Research Assistant			
Dr.-Ing.	Rainer Michalzik	–2 60 48	rainer.michalzik@uni-ulm.de
Cleanroom Management			
Dr.-Ing.	Jürgen Mähnß	–2 60 53	juergen.maehnss@uni-ulm.de
Secretaries			
	Christine Bunk	–2 60 50	christine.bunk@uni-ulm.de
	Sükran Kilic	–2 60 51	suekran.kilic@uni-ulm.de
	Hildegard Mack	–2 60 59	hildegard.mack@uni-ulm.de
Guest Scientist			
Dr.	Daniel Hofstetter	–2 60 51	daniel.hofstetter@uni-ulm.de
M. Tech.	Manmohan S. Shishodia*	–2 60 36	manmohan.shishodia@uni-ulm.de
Research Staff			
Dipl.-Ing.	Peter Brückner	–2 60 35	peter.brueckner@uni-ulm.de
Dipl.-Phys.	Frank Demaria	–2 60 46	frank.demaria@uni-ulm.de
Dipl.-Ing.	Christoph Eichler*	–2 61 95	christoph.eichler@uni-ulm.de
Dipl.-Ing.	Philipp Gerlach	–2 60 37	philipp.gerlach@uni-ulm.de
Dipl.-Ing.	Eckart Gerster*	–2 60 57	eckart.gerster@uni-ulm.de
Dipl.-Ing.	Frank Habel*	–2 64 52	frank.habel@uni-ulm.de
Dipl.-Ing.	Ihab Kardosh	–2 60 36	ihab.kardosh@uni-ulm.de
Dr.-Ing.	Christoph Kirchner	–2 60 35	christoph.kirchner@uni-ulm.de
Dipl.-Ing.	Andrea Kroner	–2 60 38	andrea.kroner@uni-ulm.de
Dipl.-Ing.	Steffen Lorch	–2 60 39	steffen.lorch@uni-ulm.de
Dipl.-Phys.	Manfred Mundbrod*	–2 60 39	manfred.mundbrod@uni-ulm.de
Dipl.-Ing.	Barbara Neubert	–2 64 54	barbara.neubert@uni-ulm.de
Dipl.-Phys.	Johannes M. Ostermann	–2 60 38	johannes-michael.ostermann@uni-ulm.de
Dipl.-Ing.	Michael C. Riedl	–2 60 36	michael.riedl@uni-ulm.de
Dipl.-Phys.	Fernando Rinaldi	–2 60 46	fernando.rinaldi@uni-ulm.de

Dipl.-Ing.	Hendrik Roscher	–2 60 44	hendrik.roscher@uni-ulm.de
Dipl.-Ing.	Sven-Silvius Schad*	–2 61 95	sven-silvius.schad@uni-ulm.de
Dipl.-Ing.	Martin Stach	–2 60 37	martin.stach@uni-ulm.de
Dr.-Ing.	Georgi Stareev	–2 64 53	georgi.stareev@uni-ulm.de

Technical Staff

	Rainer Blood	–2 60 44	rainer.blood@uni-ulm.de
	Gerlinde Meixner	–2 60 41	gerlinde.meixner@uni-ulm.de
	Susanne Menzel	–2 60 41	susanne.menzel@uni-ulm.de
	Josef Theisz	–2 60 30	josef.theisz@uni-ulm.de

* Member has left the department meanwhile

Preface

During 2004, the research activities of the Optoelectronics Department have been continuing in the areas of optical interconnect systems, vertical-cavity surface-emitting lasers, GaN-based electronic and optoelectronic devices, optically pumped semiconductor disk lasers, and high-power semiconductor amplifiers. Main achievements of the VCSELs and Optical Interconnects Group headed by Rainer Michalzik are first 40 Gbit/s signals generated by a 1300 nm InGaAlAs/InP-based DFB laser monolithically integrated with an electroabsorption modulator, flip-chip bonded two-dimensional 850 nm VCSEL arrays with threefold functional redundancy and down to 13.5 μm device pitch, as well as polarization-stable, high single- and multimode output power VCSELs incorporating specially tailored surface gratings. In the GaN Electronics and Optoelectronics Group headed by Ferdinand Scholz, high quality GaN layers could be grown by optimizing a multi-step growth procedure by the aid of marker layers. This together with our optimized HVPE process brought us closer to the realization of GaN wafers regarded as prerequisites for long-living short-wavelength laser diodes. Moreover, our investigations in modelling, mounting, and characterization of laser diodes helped to achieve new records in device lifetime by our project partners. In the High-Power Semiconductor Laser Group headed by Peter Unger, a continuous output power of 3.6 W in single spatial mode operation has been achieved with a semiconductor disk laser.

Four members of the Department, namely Irene Ecker, Marcus Scherer, Matthias Golling, and Jürgen Joos received their Ph.D. degrees. Furthermore, 11 Diploma or Master Theses and 5 Semester Projects have been carried out in 2004.

The Department further intensified the close collaboration with industrial partners. We also appreciate the financial support of national and European research organizations, which contribute the major part of our funding. Numerous publications at international conferences and a large number of articles in respected journals document the strong research activities of the Department. A detailed list can be found at the end of this report.

Peter Unger Ulm, August 2005

Integrated Focusing Photoresist Microlenses on AlGaAs Top-Emitting VCSELs

Andrea Kroner

We present 850 nm wavelength top-emitting vertical-cavity surface-emitting lasers (VCSELs) with integrated photoresist microlenses placed directly on the laser facet, with the intention to focus the output beam to some micrometer beam waist in a distance of at least 30 µm. Calculations lead to necessary radii of curvature in the range of 20 to 40 µm, depending on the diameter of the active region. The lenses are made of polymethyl-glutarimide (PMGI) and are fabricated by a thermal reflow process which was studied at different structure sizes and surface materials. Finally, basic measurements on first devices are presented.

1. Introduction

Microlenses have become an important component in many modern optical systems like optical disk players or fiber coupling setups. Nowadays, various fabrication techniques for microlenses are known and used, e.g., microjet printing, reflow processes or grey-scale lithography [1]. In the past years, different approaches have been presented to integrate VCSELs and microlenses to small-sized systems in order to shape the laser output beam [2], [3]. In most cases, the lenses were used to collimate the beam or at least to decrease its divergence. Here we present the use of photoresist microlenses to focus the output beam of top-emitting VCSELs to a desired diameter of the focal point of 4 µm at the most and a working distance of at least 30 µm. Figure 1 shows a schematic of the structure, where the lens is placed directly onto the p-contact ring of the VCSEL. On one side, the p-contact ring is connected to a bondpad, so the lens also has to cover this overlap region with the resulting difference in height.

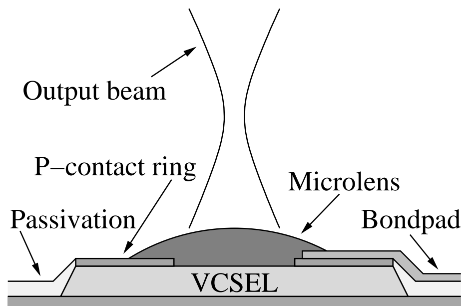

Fig. 1: Schemetic structure of the VCSEL with integrated microlens.

2. Design and Fabrication of Photoresist Microlenses

To calculate the necessary lens parameters, a Gaussian laser output beam was assumed. The shape of the beam and its propagation was calculated using the so-called matrix method, where every optical element, like interfaces or lenses, can be described by a transfer matrix [4]. Figure 2 shows the output beams of lensed VCSELs with an emission wavelength of 850 nm. On the left side, the internal beam waist, located at the oxide aperture, is assumed to have a diameter of 14 µm and a distance to the surface of 4 µm. The microlens on the surface of the VCSEL with a focal length of 50 µm in air focuses the beam to a waist of 3.7 µm at a working distance of 46.5 µm. On the right side, the internal beam waist is reduced to a diameter of 10 µm. To preserve an output beam waist of 4 µm at the most, the focal length of the microlens has to be decreased to 40 µm, which also lowers the working distance to 33.8 µm. Therefore, aiming for active diameters of 10 to 20 µm, the focal length of the lenses has to cover a range of 40 to 70 µm.

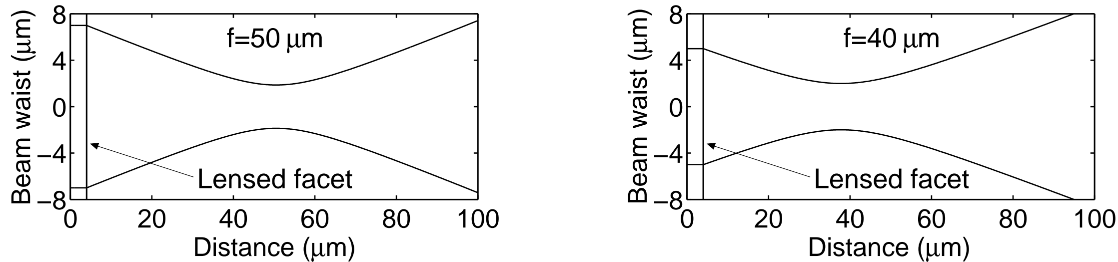

Fig. 2: Calculation of the output beam of lensed VCSELs. The left side represents a lensed VCSEL with a 14 µm active diameter and a focal length of $f = 50$ µm. On the right side, active diameter and focal length are reduced to 10 µm and 40 µm, respectively.

The microlenses were fabricated by a thermal reflow process and are made of PMGI, a positive photoresist which is photosensitive in the deep ultraviolet (DUV) regime. PMGI resist is transparent in the near infrared and shows a smooth reflow behavior at temperatures above 250 °C. Furthermore it shows an above-average chemical and mechanical stability compared to other resists, so it has been used as microlens material in the past [2].

During the process, the PMGI resist is exposed by a DUV flood exposure where no lithographic masks can be used, so a two layer process has to be applied. Therefore, after spinning and prebaking the PMGI resist, a second resist layer (AZ1512 HS) is spun on the wafer (see Fig. 3a). After a second prebake, this resist can be structured by contact lithography with a glass mask (Fig. 3b). It is important to note that the subjacent PMGI layer is not affected by the AZ developer. In the following flood exposure step, the AZ layer masks the unexposed areas (Fig. 3c). Since the AZ resist is not solved by the PMGI developer (Fig. 3d) it has to be removed with cold acetone, which does not affect the PMGI structures (Fig. 3e).

Afterwards, the sample is placed on a hot-plate at a temperature of more than 250 °C, where the cylindrical photoresist "islands" start to melt. Due to the surface tension, the

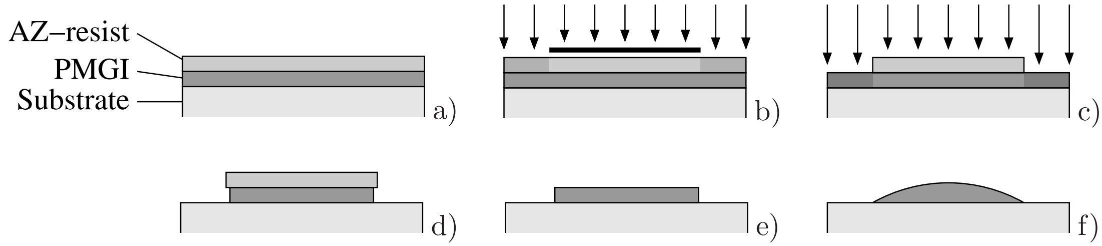

Fig. 3: Basic steps of the microlens fabrication process.

shape of the cylinders changes in order to minimize the surface energy (Fig. 3f). The resulting structure is in good approximation spherically shaped and has a focal length in air of

$$f = \frac{R}{\bar{n} - 1}, \tag{1}$$

where $\bar{n}$ is the refractive index of the PMGI resist, given as 1.535 at a wavelength of 850 nm. To reach the intended focal lengths, the radii of curvature R have to be in the range of 20 to 40 µm.

Assuming that the bottom diameter as well as the volume of the resist do not change during the reflow process, the resulting radius of curvature is only determined by the height and the diameter of the resist islands before the reflow [1]. Figure 4 shows the radius of curvature in dependence on the lens diameter for different resist thicknesses H_s. For the present VCSEL structures, the diameter of the lens has to be in the range of about 10 to 40 µm, otherwise it would be smaller than the output facet or larger than the mesa, respectively. Therefore, an initial resist thickness of about 2 µm is best suited to cover the interesting radius of curvature range.

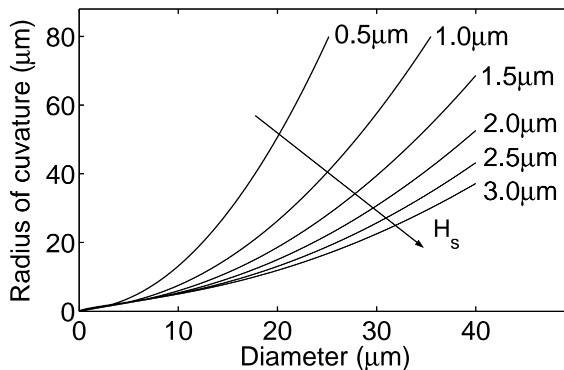

Fig. 4: Radius of curvature versus the diameter of the resist islands for different initial resist thicknesses H_s under the assumption that resist volume and diameter do not change during the reflow.

3. Microlens Fabrication Results

In Fig. 5 an optical microscope picture of a PMGI microlens on GaAs substrate with a diameter of 28 µm and an inital resist thickness of 1.8 µm can be seen. The concentric interference lines, so-called Newton rings, arise due to interference at thin layers and

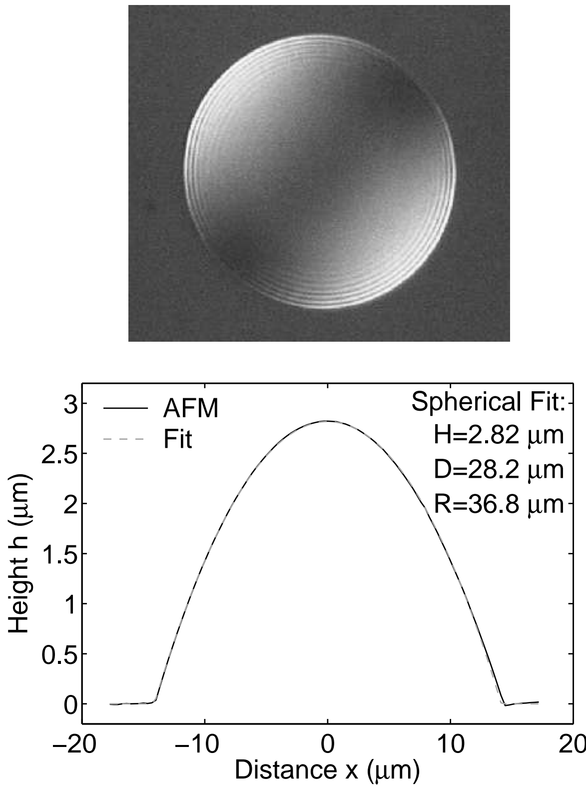

Fig. 5: PMGI microlens on GaAs substrate with a diameter of 28 µm (top left), AFM measurement of the height profile (top right), and a cross-section with a spherical fit (bottom left).

indicate the spherical shape of the lens. In the upper right corner a three-dimensional plot of the height profile measured by an atomic force microscope (AFM) is depicted. The bottom left side shows the cross-section of the profile in the center of the lens. The dashed line represents a spherical fit which reveals the nearly ideal spherical shape of the lens with a radius of curvature of 36.8 µm.

To study the reflow process more in detail, lenses with different diameters were fabricated at reflow temperatures of 250 °C and 270 °C. Furthermore, GaAs as well as gold was examined as surface material, with the latter being of special interest since the lenses will be placed directly onto the p-contact ring in the final structure. Figure 6 shows the measured radii of curvature for reflow temperatures of 250 °C and 270 °C, where the reflow time was kept constant at 20 min. The initial resist thickness for the structures on gold as well as on GaAs was 2.0 µm, so the results can be directly compared. The solid line describes the ideal behavior that was already shown in Fig. 4. For all structures a mismatch to this ideal curve can be observed, which is partly caused by a decrease of the resist volume during the reflow process due to evaporation of the solvents. This decrease was found to be in the range of 10 to 17 % for all structures, where no dependence on structure size was observed. The mean value for the sample with gold was found to be slightly smaller.

However, this could not explain the strong deviation that arises for the structures on gold, especially for small diameters and higher temperatures. Here, the radius of curvature is

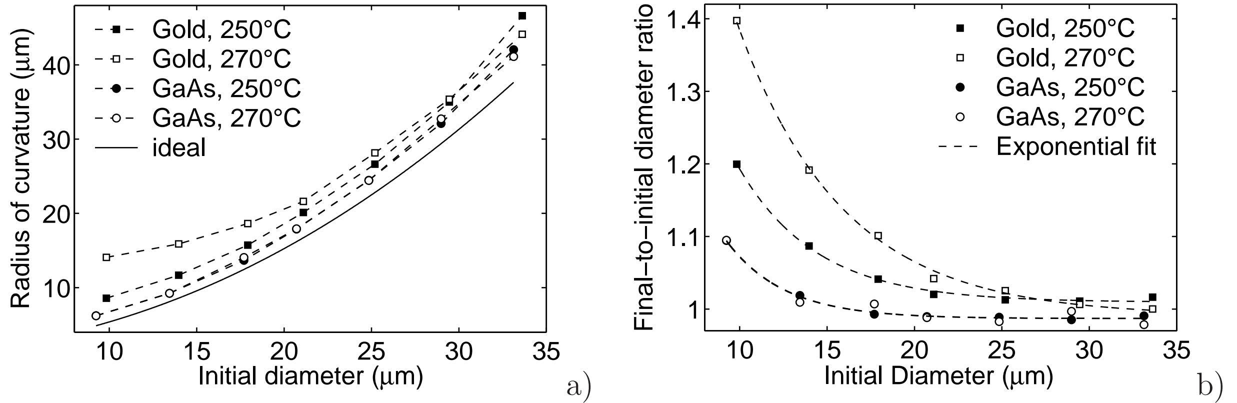

Fig. 6: Measured radii of curvature (left) and ratios between final and inital lens diameter (right) for different surfaces and reflow temperatures.

larger than expected since the diameter at the bottom of the lens does not remain constant as expected, but increases by a factor of up to 1.4 during the reflow (see right side of Fig. 6). These measurements indicate a difference in wetting between PMGI resist on GaAs and gold, where the wetting on gold seems to be stronger. However, the desired radius of curvature range can be still covered.

4. Integration of Microlenses on Top-Emitting VCSELs

The left side of Fig. 7 shows a PMGI lens with a diameter of 20 μm placed on the output facet of a top-emitting VCSEL. It can be seen that the lens does not only cover parts of the p-contact ring, but on one side also the overlap of p-contact and bond pad, which is about 200 nm thick. However this has no significant influence on the spherical shape of the lens, which can be seen in the AFM measurement of the cross-section in Fig. 7 (right).

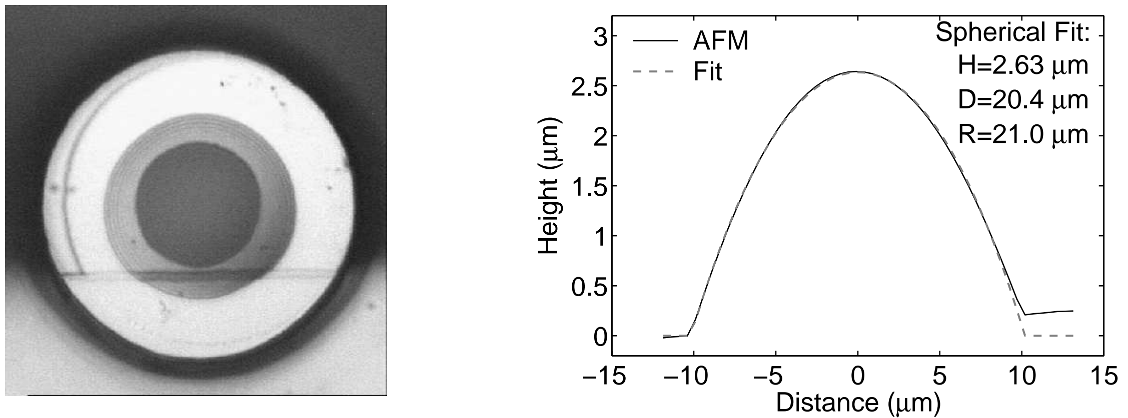

Fig. 7: PMGI microlens with a diameter of 20 μm on the output facet of a top-emitting VCSEL (left) and AFM-measured cross-section with a spherical fit (right).

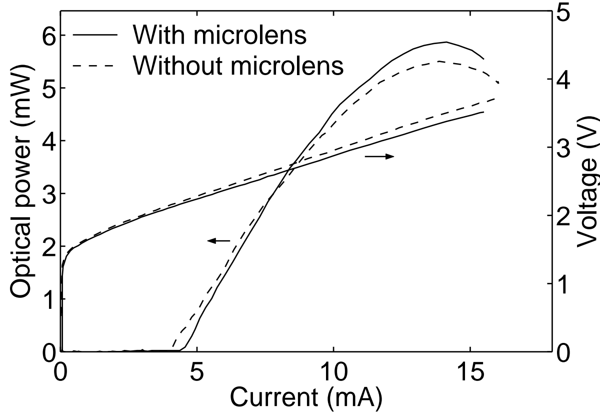

Fig. 8: Operation characteristics of a VCSEL with an oxide aperture of 5.5 µm before and after a PMGI lens was placed on its output facet. Due to the reduction of the mirror reflectivity, threshold current as well as output power have increased.

Figure 8 shows typical output characteristics of a VCSEL before and after a PMGI lens was placed on is output facet. The lens has a radius of curvature of 25 µm and the VCSEL has an oxide aperture of 5.5 µm. Here, an increase of the threshold current as well as of the maximum of output power can be observed. This indicates a reduction of the upper mirror reflectivity due to the lens material. However, the integration of the photoresist microlens does not lead to any significant performance degradation.

5. Conclusion

With PMGI photoresist subjected to thermal reflow, it is possible to deposit almost ideally shaped microlenses on top-emitting VCSELs. We have achieved radii of curvature in the range of 15 to 40 µm on GaAs as well as on gold surfaces, where a stronger wetting of resist on gold was observed. First measurements on lensed VCSELs show only a slight change of threshold current and output power. In the next step, the effects on the output field of the laser have to be determined.

References

[1] S. Sinzinger and J. Jahns, *Microoptics*. Weinheim: Wiley-VCH, 1999.

[2] M. Miller, *Aufbautechnik, Leistungsskalierung und Strahlformung oberflächenemittierender Halbleiterdiodenlaser*. PhD thesis, University of Ulm, Ulm, Germany, April 2002.

[3] S. Eitel, S.J. Fancey, H.-P. Gauggel, K.-H. Gulden, W. Bächtold, and M.R. Taghizadeh, "Highly uniform vertical-cavity surface-emitting lasers integrated with microlens arrays," *IEEE Photon. Technol. Lett.*, vol. 12, no. 5, pp. 459–461, 2000.

[4] W. Glaser, *Photonik für Ingenieure*. Berlin: Verlag Technik, 1997.

Shallow Surface Gratings for High-Power VCSELs With One Preferred Polarization for All Modes

Johannes Michael Ostermann and Pierluigi Debernardi†

Monolithically integrated full-aperture surface gratings are shown to control the polarization of all modes of even highly multi-mode 850 nm oxide-confined standard industrial vertical-cavity surface-emitting lasers (VCSELs). An orthogonal polarization suppression ratio (OPSR) of more than 11 dB up to thermal rollover is achieved for an output power of 23 mW. For devices with 8 mW output power, an OPSR of more than 20 dB at thermal rollover is observed, without major drawbacks to the overall laser performance.

1. Introduction

VCSELs show light emission lacking a strictly defined direction of polarization [1]. This is due to their isotropic gain, their usually circular resonator and the polarization-independent reflectivity of their Bragg mirrors. The electro-optic effect, induced by the doping in the Bragg mirrors, leads to a preferred polarization of the individual modes along the [011] and [0$\bar{1}$1] crystal axes [2]. In most cases the first higher order mode is polarized orthogonal to the fundamental mode. Further higher order modes can assume any of these two polarizations. If the current or the temperature changes or if optical feedback or strain is applied, a sudden change of the polarization direction of one or more modes from one of the preferred crystal axes to the other can take place. This is called a polarization switch [3].
Several approaches have been made to stabilize and control the polarization of VCSELs. These approaches can be classified in polarization-sensitive feedback (e.g. [4]), anisotropic gain (e.g. [5]), non-circular resonator geometries (e.g. [6]) or mirrors with polarization-dependent reflectivity (e.g. [7]). A main goal of our studies is to identify way of polarization control suitable for mass production. Direct incorporation into the fabrication sequence of standard industrial VCSELs grown on (100)-oriented GaAs substrates should be possible. Thus, many of the above mentioned methods have to be ruled out. As proposed in [8] we are using optical gratings which are etched into the cap-layer of the VCSELs. While previously pure metal or metal/semiconductor gratings have been used [7], simulations in [8] have shown that pure semiconductor gratings are more favorable due to smaller absorption.

†Pierluigi Debernardi is with the IEIIT-CNR c/o Politecnico di Torino, Torino, Italy.

2. Fabrication

The VCSELs were processed from standard epitaxial material for 850 nm wavelength oxide-confined VCSELs, supplied by U-L-M photonics. As the first step the full-aperture grating was realized using electron-beam lithography and wet-chemical etching. The etching process produces grating ridge edges having an angle of about 30 degrees with respect to the surface. The ratio between ridge width and grating period is approximately 65 %. In Fig. 1 an atomic force microscope (AFM) image of a grating with a period of 1.0 μm and an etching depth of 24 nm is shown. In contrast to previous suggestions [9] we use shallow surface gratings of only several tens of nanometers depth in order to not degrade the overall laser performance.

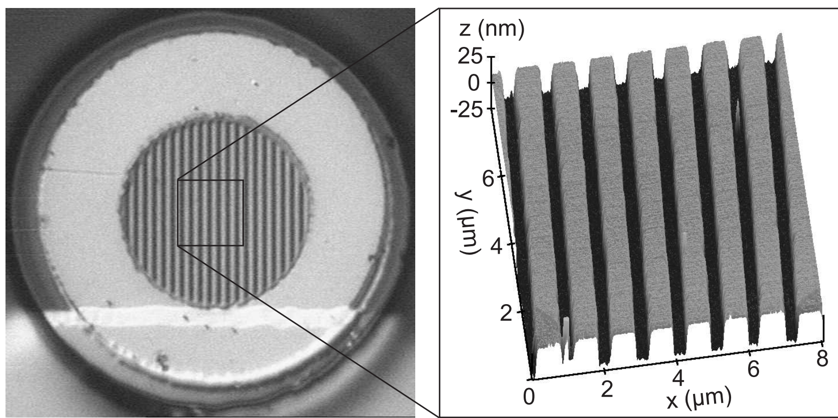

Fig. 1: Photograph of a VCSEL with an integrated surface grating (left) and an AFM measurement showing the grating in more detail (right, please note the change of scale between the x,y and the z-axis).

3. Electro-Optical and Spectral Characteristics

Figure 2 shows the polarization-resolved light–current–voltage (LIV) characteristics as well as the polarization-resolved spectra at a current of 15 mA of a standard VCSEL which is fabricated on the same chip adjacent to the grating devices. The spectra clearly reveal different modes to have different polarizations. As a consequence no polarization is preferred, which is also observed in the two LI curves recorded for the dominating [011] and [0$\bar{1}$1] crystal directions.

To be compared with Fig. 2, Fig. 3 shows the polarization-resolved LIV characteristics and polarization-resolved spectra at different currents of a VCSEL which is adjacent and nominally identical to the one shown in Fig. 2, but has an integrated surface grating as depicted in Fig. 1. This device clearly exhibits a preferred polarization orthogonal to the grating as predicted by the numerical simulations [10]. The difference between the measured total output power and the sum of the powers in both polarizations is due

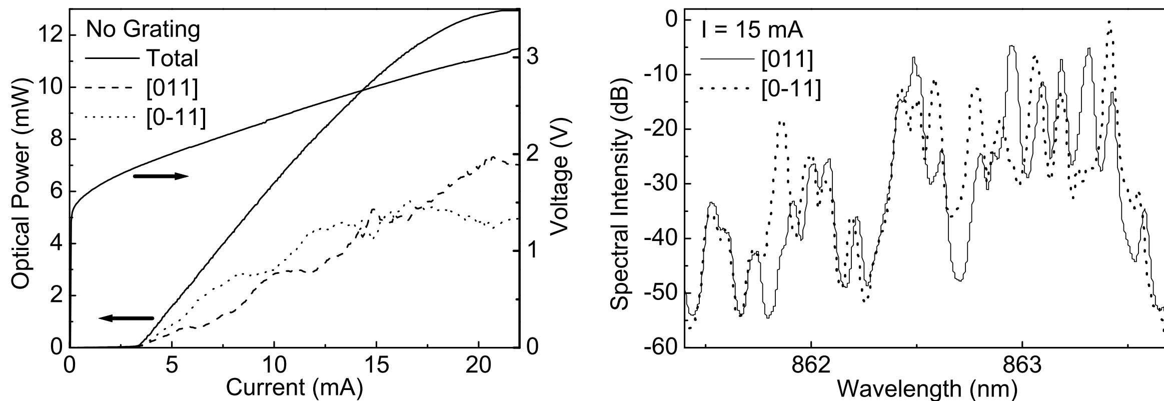

Fig. 2: Polarization-resolved LIV characteristics (left) and spectra (right) for a reference device with an active diameter of 9 μm.

to the transmission loss of the polarizer. Already below threshold (upper right graph in Fig. 3), one can see the two polarizations of one mode. They differ by 40 pm in wavelength due to the birefringence induced by the electro-optic effect and the surface grating. At a current of 15 mA the non-preferred polarization is well suppressed for all modes. The orthogonal polarization suppression ratio (OPSR) can either be defined by the peak-to-peak ratio between the strongest mode of the preferred polarization and the strongest mode of the suppressed polarization, which yields 24.9 dB for the present device at a current of 15 mA. Alternatively the OPSR may be understood as the optical power ratio which gives a reduced value of 18.6 dB. The difference is obviously due to the spectral integration done by the photodiode in the second measurement method. In what follows we will always refer to the OPSR calculated form the powers in the two polarizations.

The orientation of the polarization can be defined by the orientation of the grating grooves, as seen in Fig. 4. Both devices are nominally identical with the same grating parameters, but with their grating grooves oriented orthogonal to each other. While the polarization orientation of these two devices is therefore also mutually orthogonal, the other device properties remain essentially the same. In particular this is true for the OPSR, which for both devices exceeds 20 dB for currents above 11 mA.

As illustrated in Fig. 5, the grating even defines a preferred polarization for all modes of a high-power VCSEL with an output power exceeding 20 mW. However, the suppression for high-order modes by these shallow gratings is less effective than for low-order modes. This effect is already observed in the spectra taken at a current of 20 mA in Fig. 3 and explains the reduced OPSR for the device from Fig. 5. Nevertheless the OPSR remains larger than 11 dB up to thermal rollover.

The benefits from the surface gratings and their influence on other laser properties such as threshold current, differential quantum efficiency, and maximum output power is discussed in Fig. 6 for devices with oxide diameters between 7 and 18 μm. The open dots show the standard reference devices from the same sample, while the filled dots represent VCSELs with a surface grating with an etch depth of 24 nm and a period of 1 μm. For each oxide

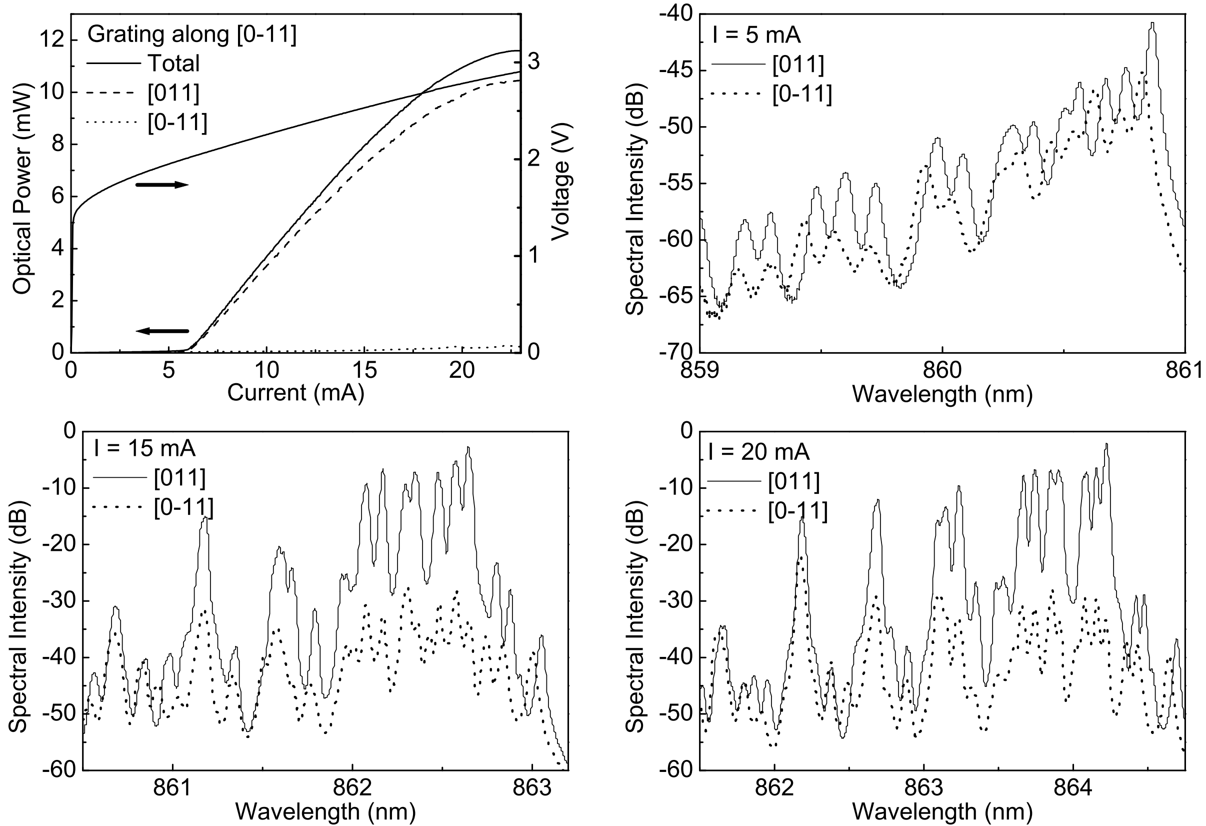

Fig. 3: Polarization-resolved LIV characteristics and spectra at different currents for a grating device with a grating period of 1.0 μm, a grating depth of 24 nm and an active diameter of 9 μm.

diameter we have measured all available VCSELs with this grating parameters on the chip, namely 5 or 6 reference devices and 5 to 7 grating devices. No reference VCSELs with 7 μm oxide diameter were processed. The OPSRs in the top–left graph are calculated from the polarization-resolved LI curves by averaging over the interval from 10 % of the maximum output power to thermal rollover. We define the OPSR as the power in the polarization parallel to the grating grooves divided by the power in the orthogonal polarization. As observed before and as expected by the simulations, the grating VCSELs are polarized orthogonal to the grating grooves, which leads to negative OPSRs. One can clearly see that VCSELs without a surface grating have no preferred direction of polarization, while VCSELs with a surface grating have a mean OPSR of -19.5 dB for the 7 μm devices. The mean magnitude of the OPSR decreases with increasing active diameter to 10.9 dB for 18 μm devices. As a drawback, depending on the epitaxial layer design, the surface grating can lead to an increase in threshold current, a small decrease of the differential efficiency and as a consequence to a smaller output power (see Fig. 6). But on one hand, in our opinion these drawbacks are not too severe in the present case. On the other hand, we have already shown that different epitaxial material VCSELs can yield increases of both the differential efficiency and the total output power as a result of grating integration [11].

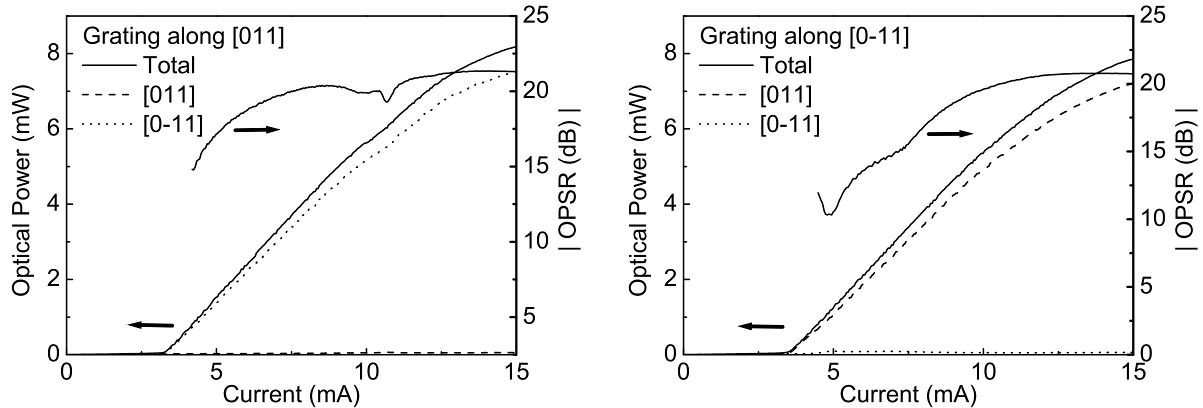

Fig. 4: Operation characteristics of two adjacent, nominally identical VCSELs with an active diameter of 6.5 μm and a nominally identical surface grating (1.0 μm period and 24 nm depth), but with their gratings turned by 90 degrees with respect to each other.

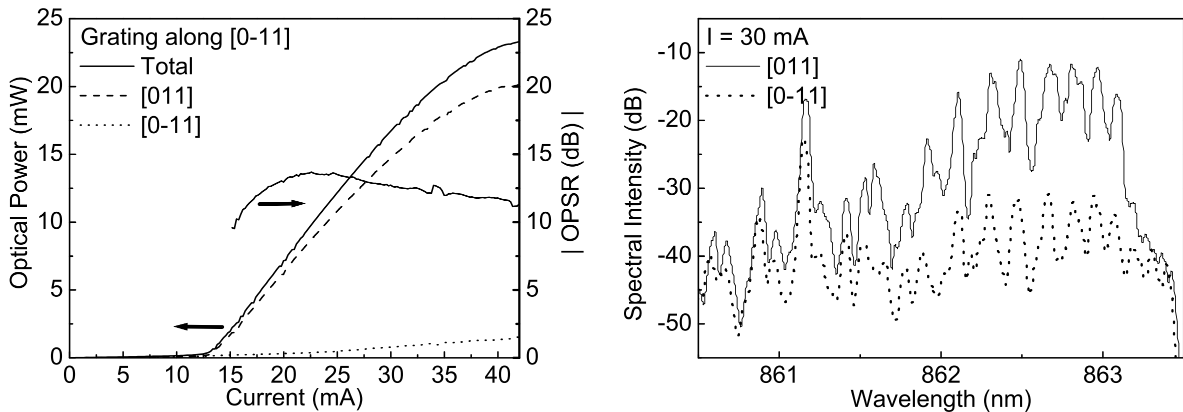

Fig. 5: Polarization-resolved LIV characteristics (left) and polarization-resolved spectra (right) for a high-power, highly multi-mode VCSEL with an active diameter of 18 μm.

4. Far-Field Emission

The left side of Fig. 7 shows the far-field of a 9 μm diameter standard VCSEL at an operating current of 15 mA. In the case of a grating VCSEL, one has to distinguish between the far-field orthogonal and parallel to the grating grooves. While no substantial difference to the reference device can be seen in Fig. 7 (right) in the far-field parallel to the grating grooves, the orthogonal far-field shows small side-lobes at an angle of approximately 50 degrees. For measuring the power of the VCSELs, the laser light is collimated with a AR-coated lens, which captures only the power within a ± 30 degrees angular interval. To some extent this explains the reduced output powers of the grating devices in the previous LI curves. The central far-field lobe itself remains undisturbed. As has been shown in [10], the far-field side-lobes vanish for grating periods smaller than the emission wavelength, which will be considered in future designs.

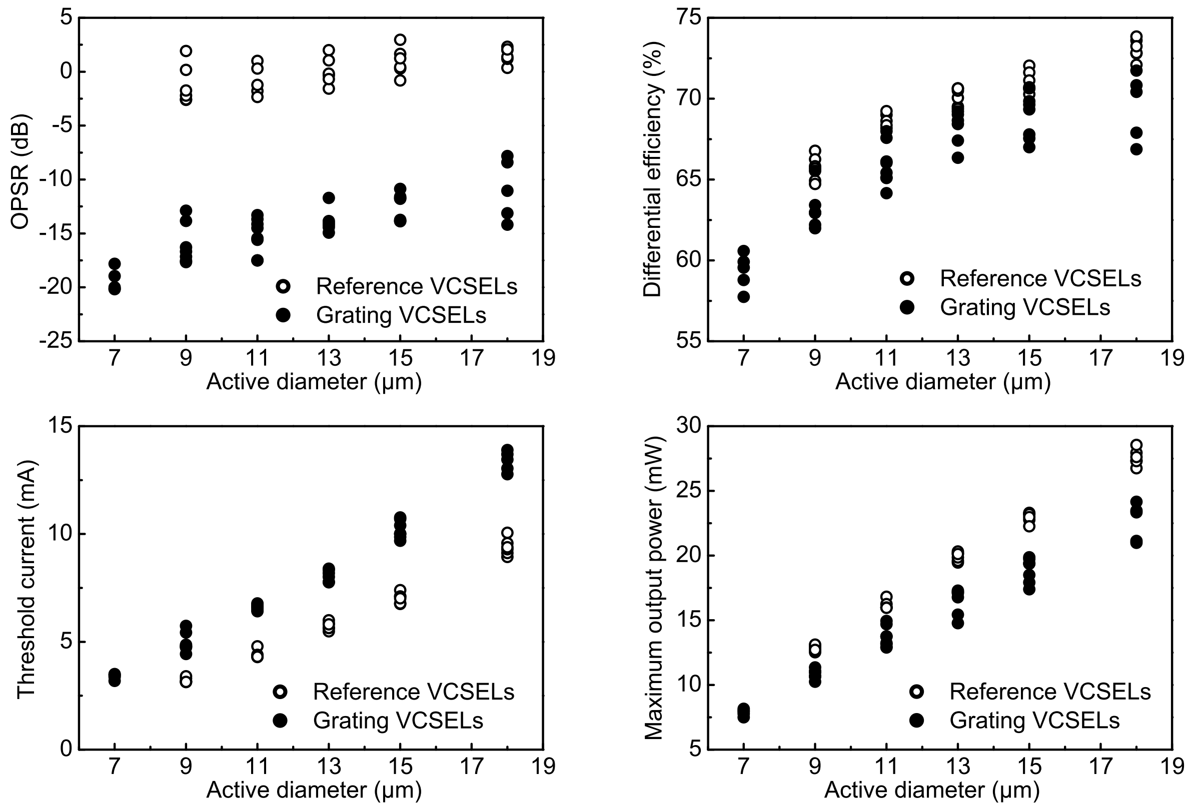

Fig. 6: Comparison of reference devices and grating devices with respect to OPSR (top–left), differential quantum efficiency (top–right), threshold current (bottom–left), and maximum output power (bottom–right).

5. Conclusion

High-power, highly multi-mode VCSELs with an integrated surface grating show one preferred and stable polarization for all transverse modes. Devices with 8 mW of output power have more than 20 dB OPSR. For carefully chosen grating parameters, especially for small etch depths, the overall performance with respect to threshold current, differential quantum efficiency, output power, and far-field properties decreases only slightly. With increasing active diameter and increasing number of modes the OPSR decreases. Nevertheless 11 dB are still achieved for an output power of more than 23 mW.

6. Acknowledgement

The authors would like to thank Christof Jalics for his help in processing the devices, U-L-M photonics GmbH, Ulm, Germany for providing the epitaxial material and Yakiv Men for performing the electron-beam lithography. The University of Ulm gratefully acknowledges the partial funding from the German Research Foundation (DFG).

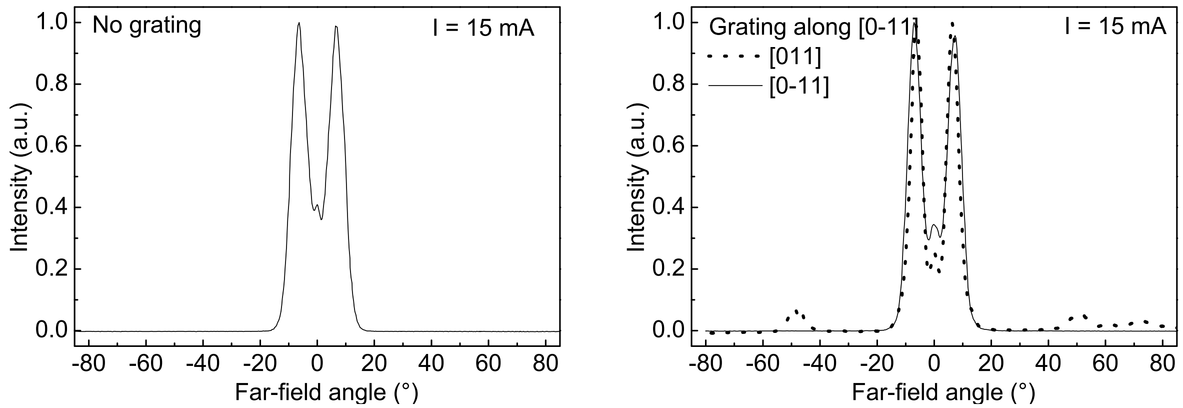

Fig. 7: The far-field of the standard VCSEL shown in Fig. 2 (left) and the parallel and orthogonal far-fields of the grating VCSEL from Fig. 3 (right), all at 15 mA current.

References

[1] C. Chang-Hasnain, J. Harbison, L. Florez, and N. Stoffel, "Polarisation characteristics of quantum well vertical cavity surface emitting lasers," *Electron. Lett.*, vol. 27, no. 21, pp. 163–165, 1991.

[2] M.P. van Exter, A.K. Jansen van Doorn, and J.P. Woerdman, "Electro-optic effect and birefringence in semiconductor vertical-cavity lasers," *Phys. Rev. A*, vol. 56, no. 1, pp. 845–853, 1997.

[3] M.S. Miguel, Q. Feng, and J.V. Moloney, "Light-polarization dynamics in surface-emitting semiconductor lasers," *Phys. Rev. A*, vol. 52, no. 2, pp. 1728–1739, 1995.

[4] C.I. Wilkinson, J. Woodhead, J.E.F. Frost, J.S. Roberts, R. Wilson, and M.F. Lewis, "Electrical polarization control of vertical-cavity surface-emitting lasers using polarized feedback and a liquid crystal," *IEEE Photon. Technol. Lett.*, vol. 11, no. 2, pp. 155–157, 1999.

[5] M. Takahashi, P. Vaccaro, N. Egami, A. Mizutani, A. Matsutani, F. Koyama, and K. Iga, "Oxide-confinement vertical-cavity surface-emitting lasers grown on GaAs (311)A substrates with dynamically stable polarisation," *Electron. Lett.*, vol. 11, no. 3, pp. 276–278, 1998.

[6] K.D. Choquette and R.E. Leibenguth, "Control of vertical-cavity laser polarization with anisotropic transverse cavity geometries," *IEEE Photon. Technol. Lett.*, vol. 8, no. 1, pp. 40–42, 1994.

[7] J.-H. Ser, Y.-G. Ju, J.-H. Shin, and Y.H. Lee, "Polarization stabilization of vertical-cavity top-surface-emitting lasers by inscription of fine metal-interlaced gratings," *Appl. Phys. Lett.*, vol. 66, no. 21, pp. 2769–2771, 1995.

[8] P. Debernardi and G.P. Bava, "Coupled mode theory: a powerful tool for analyzing complex VCSELs and designing advanced device features," *IEEE J. Select. Topics Quantum Electron.*, vol. 9, no. 3, pp. 905–917, 2003.

[9] S. Goeman, S. Boons, B. Dhoedt, K. Vandeputte, K. Caekebeke, P. Van Daele, and R. Baets, "First demonstration of highly reflective and highly polarization selective diffraction gratings (GIRO-gratings) for long-wavelength VCSEL's," *IEEE Photon. Technol. Lett.*, vol. 10, no. 9, pp. 1205–1207, 1998.

[10] P. Debernardi, J.M. Ostermann, M. Feneberg, C. Jalics, and R. Michalzik, "Reliable polarization control of VCSELs through a monolithically integrated surface grating: a comparative theoretical and experimental study," *IEEE J. Select. Topics Quantum Electron.*, vol. 11, no. 1, 2005, in press.

[11] J.M. Ostermann, P. Debernardi, C. Jalics, A. Kroner, M.C. Riedl, and R. Michalzik, "Surface gratings for polarization control of single- and multi-mode oxide-confined vertical-cavity surface-emitting lasers," *Opt. Comm.*, vol. 246, no. 4-6, pp. 511–519, 2005.

Beam Properties and M^2 Measurements of High-Power VCSELs

Ihab Kardosh and Fernando Rinaldi*

In this article, a measurement method to determine the beam quality factor of high-power VCSELs is presented. The experimental setup und the analysis method to calculate the beam parameters, M^2 factor, divergence angle, and the beam waist are described.

1. Introduction

For many industrial and scientific laser applications such as material processing, it is necessary to have a good laser beam quality for ease of fiber coupling, beam collimation, and beam focusing. In general, propagating laser beams deviate from an ideal Gaussian intensity distribution. The degree of deviation is conveniently quantified by a quality factor M^2 (called the "M-squared" factor or the "times diffraction limit number"). This factor has been defined so that $M^2 = 1$ for an ideal Gaussian beam. Real laser beams have factors greater than one. For example helium–neon lasers typically have $M^2 < 1.1$ while high-power vertical-cavity surface-emitting lasers (VCSELs) have M^2 values that can be as high as 20 and more due to their transverse multi-mode emission which results from large active diameters. Recently there has been some interest in applying high-power VCSELs for high-resolution printing and free-space optical data communication. Such applications require high optical output power and good beam quality, in other words specific M^2 factors at certain output powers. These characteristics are investigated in the present article.

2. Measurement Method and Setup

Figure 1 shows the experimental setup for the beam quality characterization. The laser beam of a mounted VCSEL is transformed through a lens system such as to form a beam waist along the propagation axis. A highly linear CCD camera is used to capture the beam image at different propagation distances. According to a procedure defined by the ISO [1], ten measurements along the propagation axis must be performed at least, where half of them should be within the Rayleigh length on both sides of the beam waist. The captured images are analyzed using a mathematical program which determines the pixel intensity from the bitmap image files and calculates the beam diameter using the second-moment

*Work performed in collaboration with U-L-M photonics GmbH, www.ulm-photonics.com

definition, where the beam diameter is four times the standard deviation. The beam radii are plotted versus the propagation distance. A Gaussian fit is used to determine the M^2 factor. In addition, the laser beam waist W_0 and the divergence angle Θ can be calculated when considering the magnification factor of the optical system. Figure 2 shows typical images from the CCD camera at different propagation distances around the beam waist.

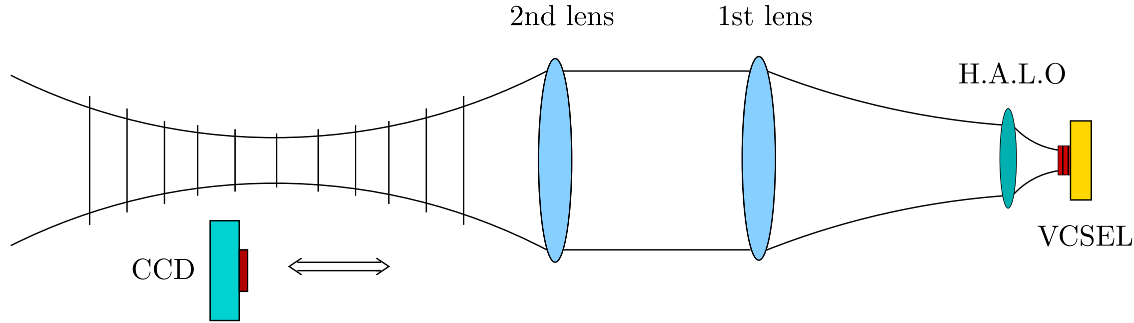

Fig. 1: Setup for the measurement of the beam quality of VCSELs. The laser beam is collimated using a high aperture laser objective lens (H.A.L.O) and a biconvex lens (1st lens). The second lens focuses the beam and thus generates a beam waist along the propagation axis.

Fig. 2: Captured images of a 80 μm active diameter VCSEL beam at different positions from the beam waist.

3. Experimental Results

Beam properties of 980 nm oxide-confined multi-mode VCSELs have been investigated. In this section we present measurement results of a 80 μm active diameter device. In Fig. 3 the light–current–voltage (LIV) and spectral characteristics are plotted. The maximum output power and the threshold current are about 190 mW and 70 mA, respectively. The spectral characteristic in Fig. 3 show a wide spectra with mode groups at different wavelengths. The mode groups at higher wavelength correspond to donut mode structures with higher intensity, while mode groups at lower wavelength correspond to outer ring structurs with lower intensity as can be seen in Fig. 2. The calculated beam radii versus the propagation distance are shown in Fig. 4. We use the Gaussian formula

$$w(z) = w_0\sqrt{1 + \left(\frac{z - z_0}{z_\mathrm{R}}\right)^2}$$

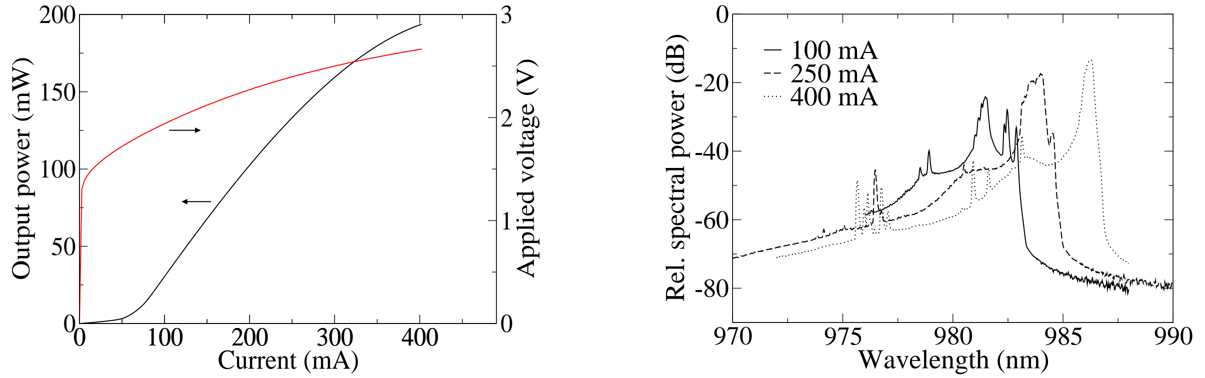

Fig. 3: LIV characteristics (left) and spectra (right) of the measured 80 μm device.

for fitting the measurement results, where $w(z)$ is the beam radius, w_0 the radius of the beam waist, z_0 the beam waist location, and

$$z_{\mathrm{R}} = \frac{\pi w_0^2}{M^2 \lambda}$$

the Rayleigh length.

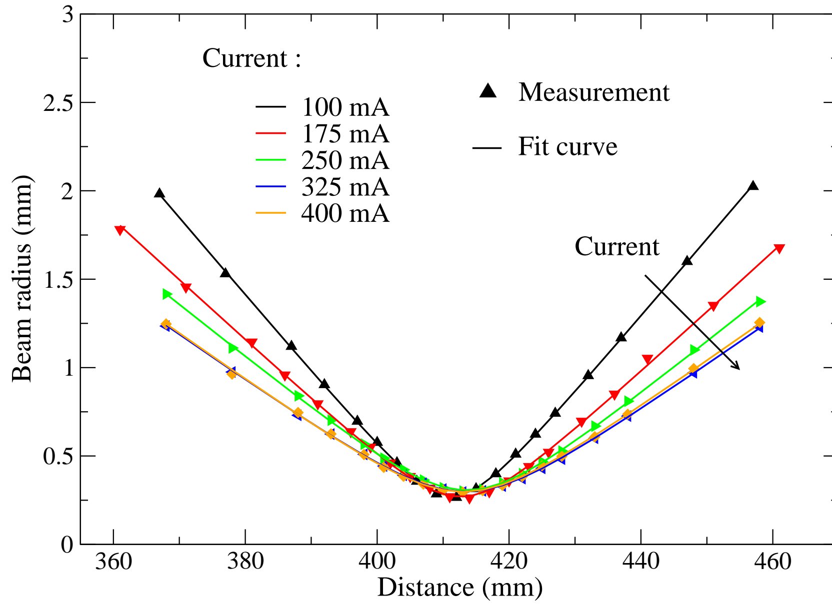

Fig. 4: M^2 measurement results for different currents.

Fitting parameters are M^2, w_0, and z_0. When considering the magnification factor m of the optical system, the far-field angle Θ of the VCSEL is approximated as

$$\Theta \approx m \frac{w_0}{z_{\mathrm{R}}},$$

and for the beam waist W_0 we obtain

$$W_0 = \frac{w_0}{m}\,.$$

Measurement results of beam quality factors and far-field angles at different currents are plotted in Fig. 5.

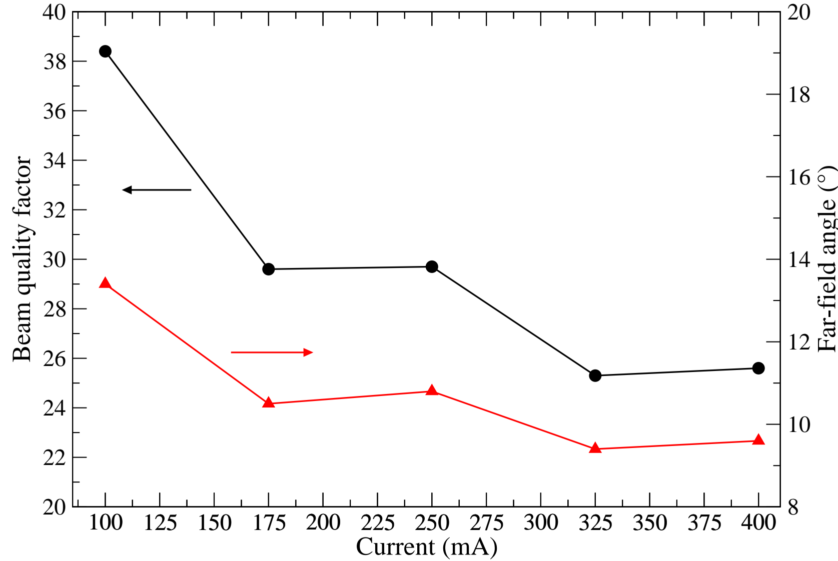

Fig. 5: M^2 values and far-field angles versus the laser current.

4. Conclusion

We have characterized high-power VCSELs regarding the beam quality. Measurement setup und analysis method have been developed to measure the M^2 factor. Beam properties of a 80 μm active diameter device have been investigated. M^2 measurements yield values ranging from about 25 to 38, where M^2 tends to decrease with increasing current. This trend is specific for this device, where other similar devices show a rather constant M^2. The far-field angle has a maximum of about 13° at 100 mA and a minimum of about 9° at 325 mA, corresponding to 170 mW optical power. The beam diameter $2W_0$ is 98 μm on average. Our aim is to get M^2 values of about 20 at output powers of around 150 mW, which is interesting, e.g., for high-resolution printing.

References

[1] International Organization for Standardization, *Lasers and laser-related equipment. Test methods for laser beam parameters, beam widths, divergence angle and beam propagation factor. ISO 11146*, 1996.

Small Pitch Flip-Bonded 850 nm 2-D VCSEL Arrays With Redundant Pixel Designs for Optical Datacom

Hendrik Roscher*

During this last year, record-high integration densities of oxide-confined vertical-cavity surface-emitting lasers (VCSELs) were achieved and implemented in two-dimensional (2-D) substrate-less 850 nm wavelength VCSEL arrays for short-distance parallel optical links. Individual high-frequency electrical input is provided over coplanar lines on a silicon flip-chip carrier substrate used as development platform. Mesa separations of only 1.5 µm and oxidation lengths below 3.5 µm enabled device pitches that are only 9 µm larger than the active diameters. Three VCSELs per fiber channel directly flip-bonded to the mesa were fitted entirely within circles of less than 28 µm diameter. To our knowledge, this results for the first time in a built-in redundancy where three equivalent VCSELs are butt-coupled to one and the same 50 µm core diameter graded index multimode fiber (50MMF) channel without additional coupling optics complicating the design. Such dense configurations preserve compactness and low module costs while markedly extending the lifetime especially of large VCSEL arrays in Tbit/s interconnect environments.

1. Introduction

Aggregate bandwidths of 2-D VCSEL arrays for space-parallel high-speed data transmission scale with the array size, i.e. the number of parallel channels. The oxide-confined high-speed VCSEL technology of such arrays has matured over the recent years with predicted VCSEL lifetimes of several hundred thousand hours, after which a distinct increase of device failures marks the onset of the wearout phase. However, there are concerns over still far too many spontaneous VCSEL failures occurring before the wearout phase at any time during the projected life. With conventional VCSEL arrays using a single laser per channel, these unpredictable premature device failures can drastically affect the reliability of transmitters for short-distance parallel optical links by lowering their overall throughput and thus requiring early replacement.

This situation can be largely alleviated by providing several alternative laser sources for each fiber channel. All VCSELs of the same channel can be either operated simultaneously with a large enough power budged to keep the channel operational as long as one of the VCSELs is still functioning. Or, alternatively, the VCSELs are activated sequentially which requires a feedback path in combination with smart driver electronic capable of

*Work performed in collaboration with U-L-M photonics GmbH, www.ulm-photonics.com

permanently switching to one of the channel's backup lasers on detecting a VCSEL failure. In order to eliminate the need for bulky and/or expensive optics combining multiple laser beams into one fiber, we fit three individually addressable VCSELs per channel directly flip-bonded to the mesa entirely inside circles as small as 28 µm in diameter. To our knowledge, this results for the first time in a built-in redundancy where three equivalent VCSELs are butt-coupled to one and the same 50 µm core diameter graded index multimode fiber (50MMF) channel hence enabling much longer lifetimes of parallel-optic transmitters.

2. Small Pitch Flip-Chip VCSEL Fabrication

The fabricated 4×4 arrays have 48 VCSELs substrate-side emitting at 850 nm. Each of the 16 segments is $250{\times}250\,\mu m^2$ in size and can transmit optical signals through one of 16 channels in a corresponding 2-D array of fibers with a typical fiber-to-fiber pitch of 250 µm. In contrast to conventional arrays with only a single laser per channel, each of the 16 array cells has three oxide-confined mesa-isolated high-speed VCSELs (see Fig. 1) so close-spaced that all three can equally butt-couple light into one and the same 50MMF. This results in a 3-per-channel redundancy of VCSEL sources. No further optics are needed to combine the multiple light beams into the same fiber. Hence, transceiver life expectancy is vastly extended while preserving compactness and low module costs.

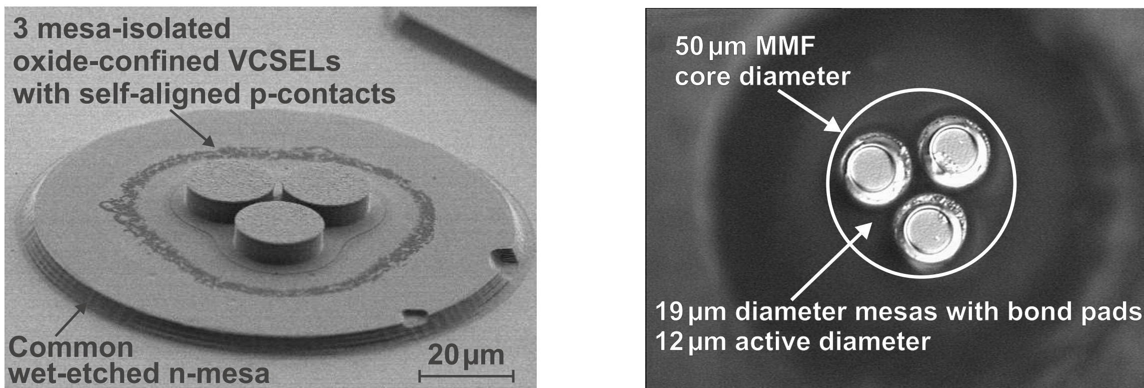

Fig. 1: SEM image (*left*) and CCD camera top view (*right*) of one array channel with a triple of the largest VCSELs. The two different fabrication stages shown are after lateral oxidation, and after completion of planarization and bond pad definition prior to indium solder deposition.

In order to achieve smallest possible pitches for mesa-isolated VCSELs, we had to depart from the usual process where p-mesa etching and the oxidation are done before the p-contact is lithographically defined with limited alignment precision. The key to the extremely small pitch VCSELs was the development of a multi-layer metal stack along with a tailored dry etch process. The metal layer stack already includes the p-contact metallization and at the same time serves as mask for dry etching. The mesa shape thus exactly follows the predefined shape of the p-contact resulting in a self-aligned full size

p-contact that utilizes the maximum possible contact area. Also, in contrast to the conventional processing sequence, the p-contact now has to withstand the high-temperature wet oxidation. The p-mesas are produced in a chemically assisted ion beam etch (CAIBE) process. The sputter component of the dry-etch process is adjusted to produce perfectly vertical mesa sidewalls, and for the etch rate in very narrow gaps to be practically the same as in wide open areas. The hard mask is etched at a rate about 30 times slower than is AlGaAs. The process leaves the p-contact on top of 6 μm high p-mesas.

In order to see what is technologically feasible in terms of close-spaced VCSEL fabrication as well as regarding direct-mesa flip-bonding of such VCSELs, the arrays were deliberately designed to be non-uniform. As many dimensions as possible were varied and within one 4×4 array, eight different VCSEL sizes are repeated twice with slightly different mesa gaps. The VCSELs have outer mesa diameters ranging from 19 to 12 μm. The mesas are separated by gaps as small as 1.5 μm. We are confident that separations below 1 μm, if needed, would be doable with this technology. The intra-cell pitches between redundant VCSEL triples hence are as small as 20.5 μm for 19 μm outer diameter lasers, and go down to only 13.5 μm pitch for 12 μm mesa diameters. To the best of our knowledge, this is the smallest separation between oxide-confined VCSELs achieved to date.

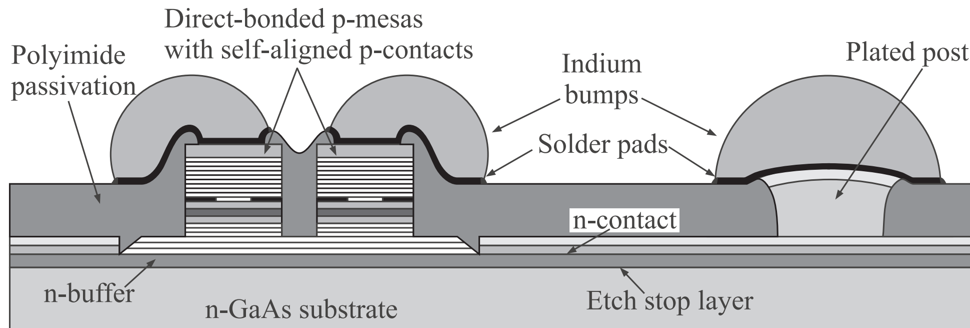

Fig. 2: Schematic cross-section depicting the elements of flip-chip ready VCSEL arrays with built-in redundancy of sources.

Electrical and optical confinement is done by selective wet oxidation of a 30 nm thick AlAs film inserted in the first quarter-wavelength layer above the p-type cladding of the inner cavity. Shallow oxidation of only 3 to 4 μm allows for a short process duration at relatively low temperatures. The schematic cross-section in Fig. 2 indicates the further device level packaging done to create flip-chip ready small pitch VCSELs. For n-contact formation on the front side, as is required for flip-chip bonding, a 3 μm thick highly n-doped AlGaAs buffer epi-layer is added between n-DBR and the substrate to laterally feed the current to the active region. Large area Ge:Au:Ni:Au-metallization self-aligned to the bottom of the shared wet etched n-mesas makes an ohmic contact to the buffer layer. A single polyimide layer serves as passivation and for elevation of the n-bond pads. The n-opening in the polyimide is filled by electroplating. The n- and p-bond pads are not at exactly the same mean elevation and the difference in standoff height is accommodated for by different indium bump sizes. Several bond pad sizes were tested. The smallest

p-pads have a diameter of only 14 µm and are confined to the mesa tops as in the right hand photo of Fig. 1. The corresponding indium bumps are only 10 µm high. Larger pad versions are partially overlapping with the mesas and extend further to the outside as indicated in Fig. 2. The soft indium solder has the capacity to compensate stresses arising between the flip-chip joined substrates. It thus enables direct-mesa bonding which ensures high signal integrity for data transmission, and it provides an efficient heat flow path keeping the device's thermal resistance at low values.

3. Flip-Chip VCSEL Demonstrators

As a platform for demonstration of direct-mesa flip-bonding of small pitch VCSELs, an $8{\times}8\,\mathrm{mm}^2$ silicon carrier substrate was implemented. It replaces an electronic chip which, in anticipated implementations, would provide the fast logic, as well as the drive currents. The photograph in Fig. 3 shows the high trace density on the carrier. There are 48 coplanar lines routed from the outer perimeter to each of three VCSELs in each of 16 segments. The traces can deliver electrical high frequency input to the individual VCSELs. Prior to flip-chip integration, the VCSEL arrays were aligned with their cleaved edges along alignment elbows on the carrier substrate by simply pushing them using precision translation stages under a stereo microscope. The two crosses visible in the center area of the carrier were intended for infrared backside alignment of the parts in case the limited precision of the cleaved edges would lead to imprecise pre-alignment and impede good bond results. This was, however, not needed especially when the bonding was done without a prior reflow.

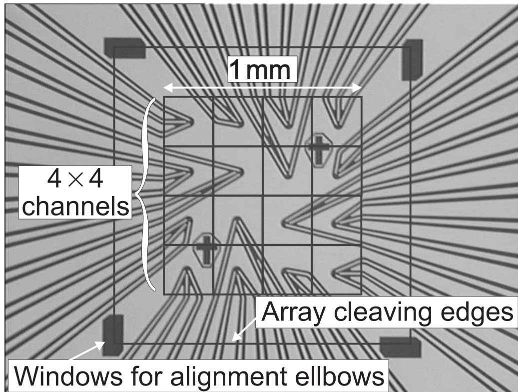

Fig. 3: Photograph of the central section of the silicon flip-chip carrier substrate. The added black lines indicate where the cells of the VCSEL array and its cleaved edges will be. The two crosses for backside alignment were only needed to verify proper self alignment of the parts during bonding.

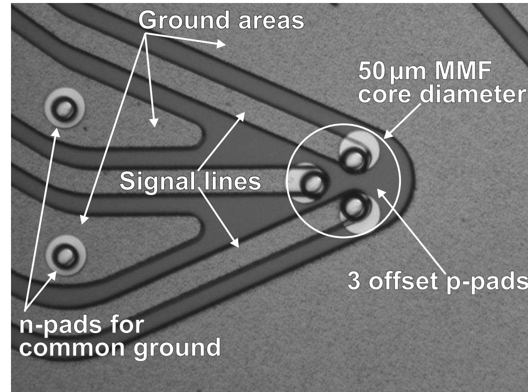

Fig. 4: Close-up photo of the approximate area on the carrier underneath one VCSEL array segment (corresponding to one fiber channel). The 50 µm-circle indicates the p-contact positions with respect to high bandwidth multimode fiber core diameters.

A 300 nm thick intermediate dielectric layer of SiO_2 between the semi-insulating silicon substrate and the gold metallization minimizes leakage currents. The tracks layer is protected by a polyimide coating also serving as a non-wettable layer for the flip-chip process. Figure 4 shows the completed carrier chip close-up for one channel. For long-term reliability of the solder joints a stable under bump metallurgy is crucial. Thick electroplated pads can, however, not easily be used for such very closely spaced contacts since the lateral plating will tend to create electrical shorts between them. In order to still get a stable foundation for the solder balls, the polyimide opening is first filled with electroplated nickel followed by a gold finish. The top of this little metal post was already successfully used as a tiny bond pad. Alternatively, larger offset pads were evaporated on top of the planarized polyimide openings to give the solder joints more stability. Because of the small dimensions, ground potential for some areas between the traces had to be maintained by connecting them to the common ground on the VCSEL array via n-contacts.

The VCSEL arrays are flip-bonded onto the silicon carrier in a high temperature process of about 5 min including cool-down. Since the GaAs substrate very effectively absorbs the light of 850 nm wavelength produced inside the GaAs active region, it is completely removed in a H_2O_2 based spray etch process. The process has a high selectivity to high Al-content AlGaAs which is used to stop etching at a defined interface. The etch stop layer is then etched away by an HF solution, leaving an epitaxially defined out-coupling facet. Those post-assembly etching steps reduce the VCSEL wafer to only the structured epitaxial layers. Figure 5 shows details of the VCSEL array hybrid integration process.

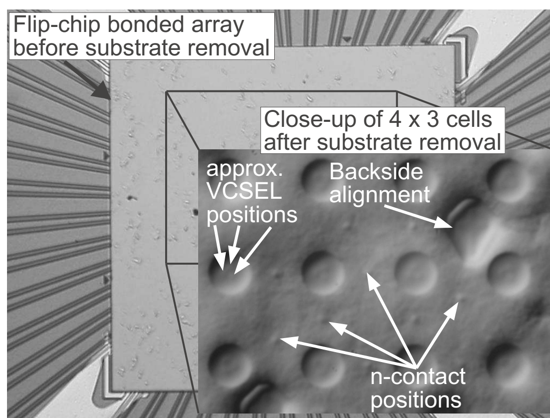

Fig. 5: Photo of VCSEL array immediately after flip-chip attachement It is overlaid by a CCD photo of a 4 × 3 array section after complete substrate removal. Structures on the underside of the remaining 3 µm thick buffer layer are made visible with special microscope filters.

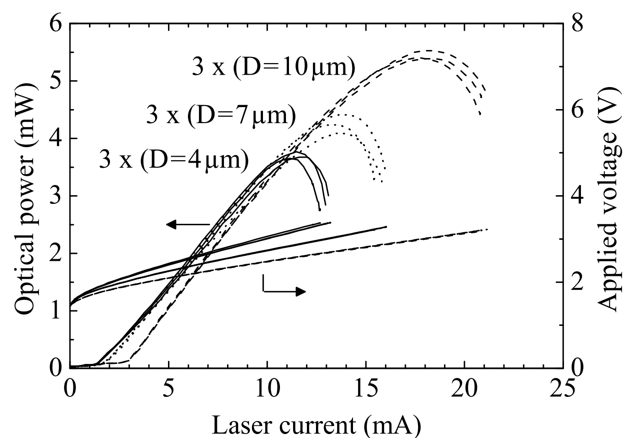

Fig. 6: LIV curves of three VCSEL triples in three cells of the (4×4)×3 VCSEL array in Fig. 5. Outer mesa diameters and mesa gaps for the 10, 7, and 4 µm active diameter VCSELs are 17 and 3.5 µm, 14 and 2.5 µm, 12 and 1.5 µm, respectively.

4. Results

About ten VCSEL arrays were flip-bonded to carrier substrates so far. Because of the small size of the processed piece from a VCSEL wafer the thick lift-off resist for the indium solder was faulty in some places causing some of the solder deposits to merge even before bonding and thus leading to shorts. In several bonded arrays there was only one short occurring between two of the 48 VCSELs. All other lasers were working including the third devices in the affected cells. Due to the direct mesa bonding technique, the small pitch VCSELs also have quite a competitive thermal performance. A thermal resistance R_T of 1.34 K/mW was reached for 12 μm active diameter circular devices. Low thermal resistance values generally increase the maximum achievable output power and thus allow to reach high channel data rates. Figure 6 shows exemplary light–current–voltage (LIV) output characteristics of three VCSEL triples in three cells of the array shown in Fig. 5. The differential quantum efficiencies are between 29 and 31 %. Depending on the VCSEL size the differential resistances are 77, 95, and 126 Ω with lasing thresholds of 3, 1.8, and 1.3 mA. High thresholds generally lead to higher power consumption of transmitters. The devices should therefore be optimized for lower thresholds. Unfortunately, there are no conventional devices processed from the same VCSEL wafer available at this point. It is therefore not possible to quantify the impact the very short oxidation length has on key parameters such as lasing threshold, slope efficiency and the like.

5. Conclusion

Record-high integration densities of flip-bonded oxide-confined VCSELs in 2-D arrays enabled a 3-per-channel VCSEL redundancy for strong lifetime improvements of parallel-optic transmitters. Compactness and low module costs are preserved by still permitting butt-coupling to 50MMFs. High-density VCSEL fabrication was made possible by a dry etch process utilizing the p-contact metallization as an etch mask. To test the technological feasibility, the dimensions of the VCSEL triples were varied between channels within (4×4)-channel arrays. In one array, there are triples of mesa-isolated VCSELs with outer diameters varying from 19 to 12 μm. Each VCSEL has a self-aligned full-size p-contact which is present during high-temperature wet oxidation. Mesa separations as small as 1.5 μm and oxidation lengths below 3.5 μm enabled, to the best of our knowledge, the highest integration density of oxide-confined VCSELs ever achieved to date with device pitches that are only 9 μm larger than the active diameters.

Acknowledgment

Special thanks to M. Bou Sanayeh, S. B. Thapa, and G. Wendrock who worked with me during this last year toward their theses. Their many contribution are much appreciated. Partial funding from the German Research Foundation (DFG) is also acknowledged.

High-Performance Low-Cost Optical Link at 850 nm With Optimized Standard Singlemode Fiber and High-Speed Singlemode VCSEL

Martin Stach*

Quasi error-free 9 Gbit/s data transmission experiments are presented over 1 km of ITU-T G.652 compliant 9 μm core diameter singlemode fiber with high bandwidth at 850 nm using a high-speed singlemode VCSEL.

1. Introduction

Multimode fibers (MMFs) optimized for data transmission at 850 nm wavelength are increasingly referenced and used by applications, cabling, and fiber standards [1]. Such fibers enable the lowest total system cost for interconnect distances between 150 m and 600 m by using vertical-cavity surface-emitting laser (VCSEL) transceivers at speeds up to 10 Gbit/s. It would be of much interest to extend the cost benefit of short-wavelength VCSELs to longer distances of up to a few kilometers while exploiting the standard singlemode fiber (SMF), which is so far the cheapest and most widely used fiber on the market. However, currently available VCSELs emit in multiple transverse modes which is very beneficial to meet the encircled flux conditions (as specified in the 10-GbE standard) for the power launched into a MMF. The latter intend to avoid the region close to the fiber axis which often shows a rather poor differential mode delay (DMD) behavior. Obviously, the coupling efficiency of multimode VCSEL emission into SMFs is very low. Another limit in using VCSELs with SMFs is imposed by the poor modal bandwidth of a standard SMF at 850 nm. In this paper it is shown how these drawbacks can be overcome by using a singlemode VCSEL and a specially designed SMF, optimized for 850 nm operation. With this combination, transmission up to 9 Gbit/s is demonstrated over 1 km of G.652 compliant fiber. The work has been presented at ECOC 2004 [2].

2. Fiber Description

ITU-T G.652 compliant singlemode fibers are optimized for operation above 1310 nm and usually feature a very low intermodal bandwidth in the wavelength region around

*Work performed in collaboration with Pirelli Cables and Systems Telecom SpA, Milano, Italy (www.pirelli.com) and U-L-M photonics GmbH, Ulm (www.ulm-photonics.com)

850 nm, where at least the LP_{01} and LP_{11} modes are well guided by the core. Two-mode fiber systems based on intermodal delay equalization have been widely studied [3]-[6] in order to address several different applications. Various refractive index profiles have been suggested to achieve zero-modal dispersion at 1300 nm [5] or in the 800 to 900 nm wavelength range [6]. The fiber used in the experiments achieves equalization at 850 nm through careful optimization of a slightly graded profile, capable of yielding G.652 compliant characteristics in the 1260 to 1625 nm region. Typical intermodal delay at 850 nm is less than 0.3 ps/m over a wide wavelength range, which inherently guarantees a 3 dB worst-case modal bandwidth higher than 1000 MHz · km. The feasibility of quasi error-free transmission using such a fiber at 1.25 Gbit/s over 2 km and at 155 Mbit/s over 7.4 km while employing commercially available multimode VCSELs has already been demonstrated in previous papers [7],[8]. Nonetheless, so far, the lack of high-bandwidth singlemode VCSELs has prevented the exploration of higher bit rates.

3. Singlemode VCSEL Operation Characteristics

For the purpose of this study, oxide-confined 850 nm GaAs based VCSELs with optimized singlemode behavior have been fabricated. As shown in Fig. 1 (left), the lasing threshold is found at 0.5 mA and 1.6 V. Maximum singlemode and multimode output powers are 3.1 mW and 4.3 mW, respectively.

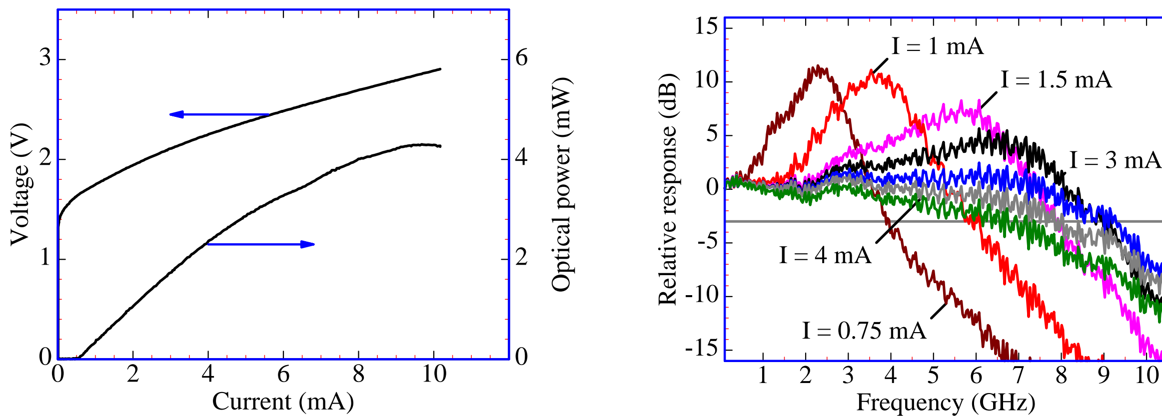

Fig. 1: CW operation characteristics (left) and small-signal frequency response curves of the oxide-confined GaAs singlemode VCSEL (right).

The bias current for the small-signal as well as data transmission experiments was chosen as 3 mA, where the differential resistance amounts to 154 Ω. As illustrated in Fig. 1 (right), the 3-dB bandwidth is then maximized at 9 GHz, which makes the device capable for 10 Gbit/s data transmission. At the receiving end, a multimode fiber pigtailed InGaAs pin-photoreceiver with above 8 GHz bandwidth was used.

4. DMD and Digital Data Transmission

In order to get quantitative insight into the modal delay properties of the SMF, the DMD characteristics at 850 nm wavelength have been determined. Here, a 5 μm core diameter singlemode fiber is scanned over the 9 μm SMF input at a distance of about 10 μm (in accordance with the IEC pre-standard 60793-1-49, Sect. 3.3.) and the impulse response at the output end is recorded for each offset position. A gain-switched 850 nm singlemode VCSEL delivering pulses with less than 40 ps full width at half maximum is employed for this purpose. The results in Fig. 2 (left) reveal that the DMD is below 0.1 ps/m, which clearly enables data rates in the range of 10 Gbit/s.

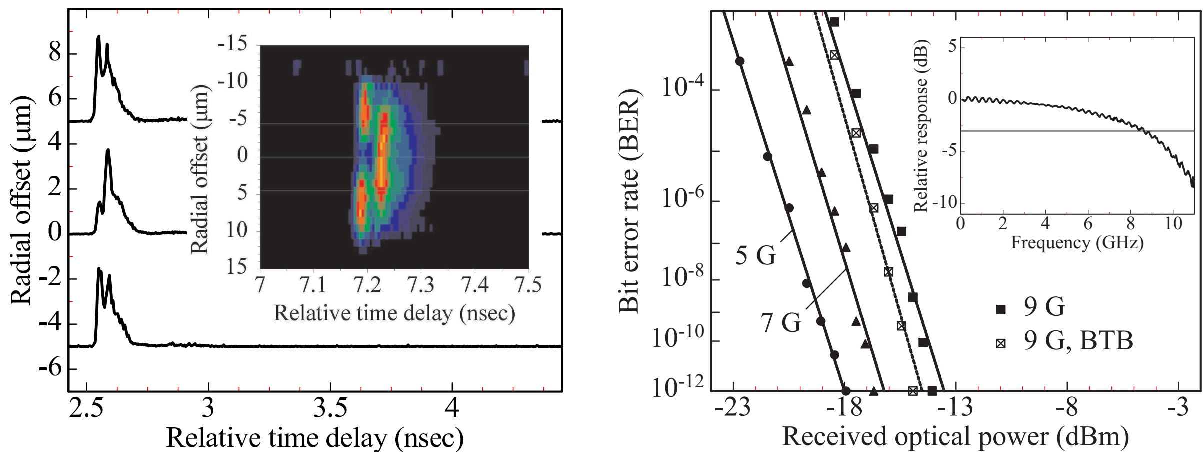

Fig. 2: DMD characteristics for the 1 km-long SMF (left) and BER characteristics for 1 km SMF transmission at data rates of 5, 7, and 9 Gbit/s (right). The inset shows the small-signal fiber response.

Data transmission experiments have been carried out under non-return-to-zero $2^7 - 1$ and $2^{31} - 1$ word length pseudo random bit sequence modulation using the aforementioned singlemode VCSEL driven with $U_{\text{pp}} = 0.6\,\text{V}$. Figure 2 (right) summarizes the obtained bit error rate (BER) curves for $2^7 - 1$ word length. With the longer word length, power penalties of 1.7 and 1.9 dB are observed at data rates of 5 and 7 Gbit/s, respectively. Low-frequency cut-offs of electronic components have probably prevented 9 Gbit/s transmission in this case. The power penalty versus back-to-back (BTB) operation is about 0.9 dB at a BER of 10^{-12} for the transmission of the 9 Gbit/s signal. There is almost no power penalty versus BTB operation for the transmission of data rates below 7 Gbit/s. The observations are in agreement with the small-signal measurement results of the fiber which are depicted in the inset in Fig. 2 (right). These show a bandwidth–length product of 9 GHz · km, so that the VCSEL might appear as the limiting factor of the high-speed data transmission.

5. Conclusion

For the first time, quasi error-free transmission of a 9 Gbit/s digital data signal at 850 nm over a specially designed standard singlemode fiber of as much as 1000 m length has been demonstrated by means of a high-speed singlemode VCSEL.

References

[1] R. Michalzik, R. King, F. Mederer, M. Kicherer, G. Giaretta, and K.J. Ebeling, “Short-wavelength vertical-cavity surface-emitting laser applications: from high throughput multimode fiber links to two-dimensional interchip interconnections,” *Opt. Eng.*, vol. 40, no. 7, pp. 1179–1185, 2001.

[2] M. Stach, F.I. Pomarico, D. Wiedenmann, and R. Michalzik, “High-performance low-cost optical link at 850 nm with optimized standard singlemode fiber and high-speed singlemode VCSEL,” in Proc. *30th Europ. Conf. on Opt. Commun., ECOC 2004*, vol. 3, pp. 712–713. Stockholm, Sweden, Sept. 2004.

[3] K. Suto, E. Yoneda, T. Hayakawa, and T. Tuchiya, “0.78 μm digital transmission characteristics using 1.3 μm optimized single-mode fiber for a subscriber loop,” *Elec. and Comm. in Japan*, part 1, vol. 75, no. 2, pp. 38–47, 1992.

[4] K. Kitayama, Y. Kato, S. Seikai, N. Uchida, and M. Akiyama, “Transmission bandwidth of the two-mode fiber link,” *IEEE J. Quantum Electron.*, vol. QE-18, no. 11, pp. 1871–1876, 1982.

[5] L.G. Cohen, W.L. Mammel, C. Lin, and W.G. French, “Propagation characteristics of double-mode fibers,” *Bell Syst. Techn. J.*, vol. 59, pp. 1061–1072, 1980.

[6] V.A. Bhagavatula, J.C. Lapp, A.J. Morrow, and J.E. Ritter, “Segmented-core fiber for long-haul and local-area-network applications,” *J. Lightwave Technol.*, vol. 6, no. 10, pp. 1466–1469, 1988.

[7] F.I. Pomarico, M. Artiglia, E. Besozzi, and S. Cozza, “BER measurements using 850 nm VCSEL on optimized SMF with ultra-low inter modal dispersion at short wavelengths,” in Proc. *7th European Conf. on Networks & Opt. Comm., NOC 2002*, pp. 205–209, Darmstadt, Germany, June 2002.

[8] F.I. Pomarico and M. Artiglia, “1.25 Gb/s enhanced transmission performance on standard single-mode fiber optimized for operating at 850 nm using single-mode VCSEL,” in Proc. *51st IWCS/Focus Symposium*, pp. 471–474, Lake Buena Vista, FL, USA, November 2002.

Up to 40 Gbit/s Operation of Laser-Integrated Electroabsorption Modulator Using Identical InGaAlAs Quantum Wells

Philipp Gerlach*

The modulation performance of InP-based 1.3 µm wavelength laser-integrated electroabsorption modulators using an identical InGaAlAs quantum well stack in both device sections is investigated. A typical device shows a threshold current of 22 mA, 35 dB side-mode suppression ratio and about 25 GHz modulation bandwidth. Open eye diagrams at 10 Gbit/s non-return-to-zero (NRZ), 20 Gbit/s return-to-zero (RZ) and 40 Gbit/s NRZ modulation have been measured.

1. Introduction

Electroabsorption modulators (EAMs) are attractive devices for modern telecommunication systems owing to their potential for high-speed modulation [1], high extinction ratio at low driving voltage, low chirp as well as small size. To avoid high coupling losses, EAMs can be monolithically integrated with other semiconductor components such as distributed feedback (DFB) laser diodes (LDs) [2] or semiconductor optical amplifiers (SOAs). Using the same active layer in all device sections, critical technological steps like selective epitaxy or quantum well intermixing are avoided which greatly simplifies device fabrication.

2. Device Design

Investigated devices are based on a 2 µm wide ridge-waveguide structure grown on a semi-insulating InP wafer. The devices contain ten 5 nm thick InGaAlAs quantum wells (QWs). They have a 370 µm long DFB-LD section and a 130 µm long EAM section, which are electrically isolated by an etch trench. Local DFB gratings in the LD section have been realized by holographic lithography followed by epitaxial overgrowth. A second mesa has been etched to get access to n-InP from the top side. In order to minimize the effective capacitance, the mesa width in the EAM section is only 2 µm and thus as narrow as the ridge-waveguide. The back and front facets are high-reflection (HR) and anti-reflection (AR) coated, respectively. A schematic of a device is shown in Fig. 1. Within the LD

*Work performed in collaboration with Infineon Technologies AG, Munich, Germany

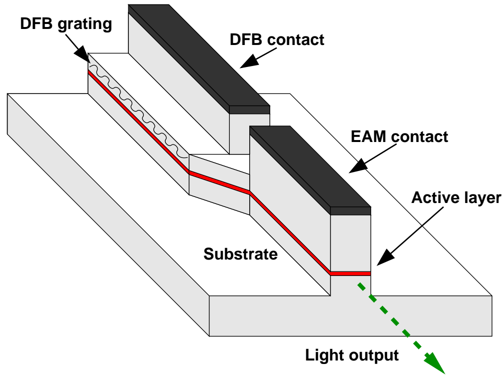

Fig. 1: Schematic of laser-integrated electroabsorption modulator.

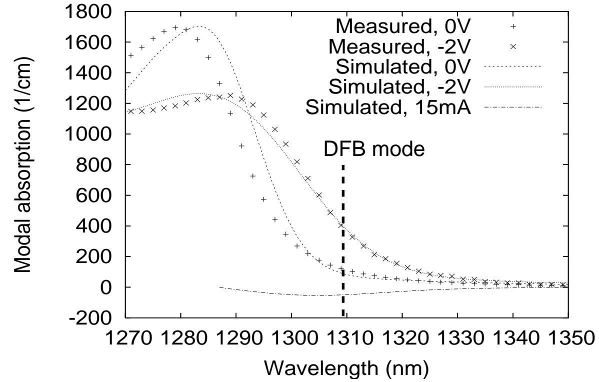

Fig. 2: Simulated and measured modal absorption as well as simulated gain at 15 mA. The DFB laser operating wavelength is indicated at 1309 nm.

the QWs provide gain under forward bias and in the EAM the absorption changes under reverse bias due to the quantum confined Stark effect. The design of an identical active layer in the LD and the EAM is challenging because low threshold current in the LD and low residual absorption in the EAM appear to be contradicting design criteria [3]. Further details concerning device fabrication are found in [4]. Simulated and measured modal gain and absorption spectra are displayed in Fig. 2. The operating wavelength of 1309 nm is defined by the DFB grating. Positive detuning with respect to the gain peak has been chosen.

3. Static Characteristics

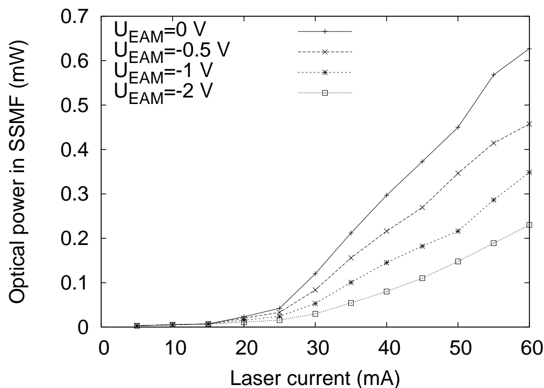

Fig. 3: SSMF-coupled optical power for different EAM bias voltages U_{EAM}.

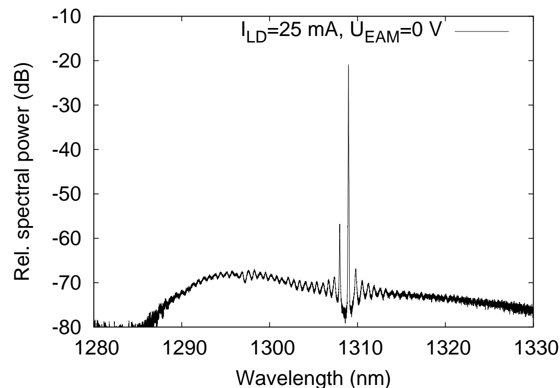

Fig. 4: Measured optical output spectrum at 25 mA LD current and 0 V EAM bias.

The optical output power has been coupled into a standard single-mode fiber (SSMF) using a lens-integrated isolator with 50 % coupling efficiency. The fiber-coupled optical

power is shown in Fig. 3. The threshold current amounts to 22 mA and the static extinction is 4 dB for a voltage swing of 2 V. An optical output spectrum at 25 mA is depicted in Fig. 4, exhibiting a side-mode suppression ratio of more than 35 dB.

4. Modulation Response

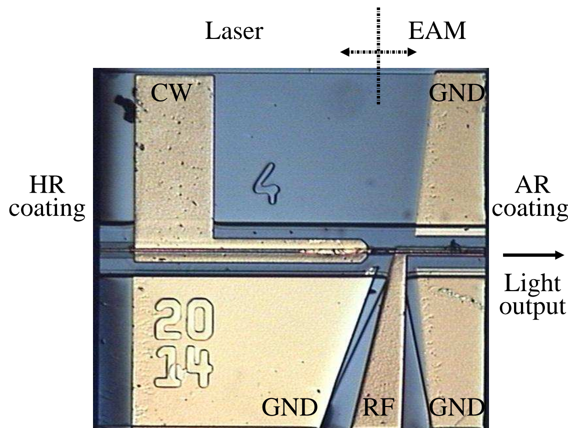

Fig. 5: Photograph of DFB-LD–EAM. Total device length is 500 µm.

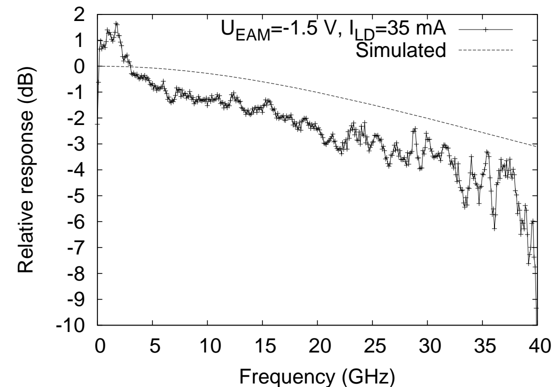

Fig. 6: Measured electro-optical response at 35 mA laser current and −1.5 V EAM bias as well as simulated response.

Because even at 40 GHz modulation the electrical wavelength is much shorter than the length of the EAM, we consider the EAM to be lumped and assume travelling wave effects to be negligible. To measure the electro-optical response, a constant LD current of 35 mA and an EAM bias of −1.5 V is applied to the LD and EAM contact pads, respectively. The p-contact pads, as well as the n-ground pads can be seen in the photograph in Fig. 5. The coplanar EAM pad is connected by a 50 Ω microwave probe. The determined modulation response is shown in Fig. 6 and indicates the 3-dB modulation bandwidth to be about 25 GHz. A simulation result at low optical input power is plotted in the same diagram, where the simulation model from [5] has been employed.

5. Non-Return-to-Zero Modulation at 10 Gbit/s

Figure 7 shows the schematic setup which has been used to measure large-signal modulation. For data rates of 10 Gbit/s NRZ modulation a pattern generator which is specified up to 12.5 Gbit/s operation is used as a pseudo-random bit sequence data source. On the receiving side a photoreceiver module with an electrical bandwidth of 40 GHz is connected to a wideband sampling oscilloscope. As can be seen in Fig. 8, an open eye diagram with fast transition times of about 25 ps is measured.

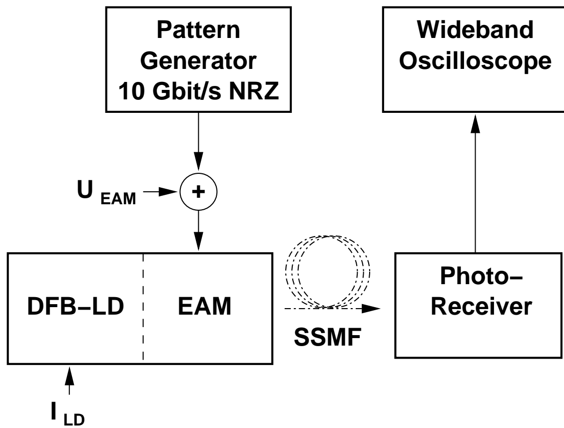

Fig. 7: Schematic setup for large-signal NRZ modulation at a data rate of 10 Gbit/s.

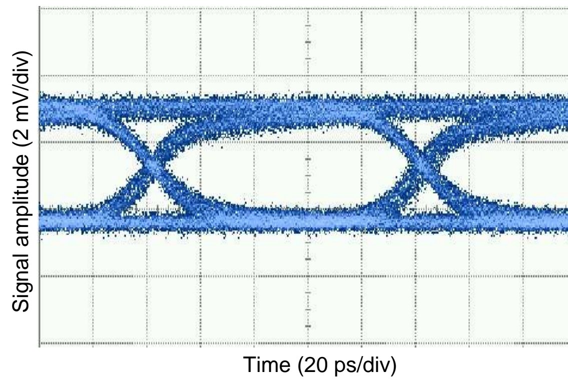

Fig. 8: Measured eye diagram at 10 Gbit/s NRZ modulation.

6. Return-to-Zero Modulation at 20 Gbit/s

A commercial RZ signal source operating at data rates above 10 Gbit/s is not available in the department. Therefore the pattern generator indicated in Fig. 7 is exchanged by the multiplexer setup depicted in Fig. 9. It splits the 10 Gbit/s signal and delays one of them in order to multiplex two different, almost uncorrelated signals up to a data rate of 20 Gbit/s. Another multiplexer with a constant zero at one of its inputs converts these 20 Gbit/s NRZ signals to 40 Gbit/s RZ signals. Incorporating this multiplexer system, an open optical eye diagram shown in Fig. 10 has been achieved.

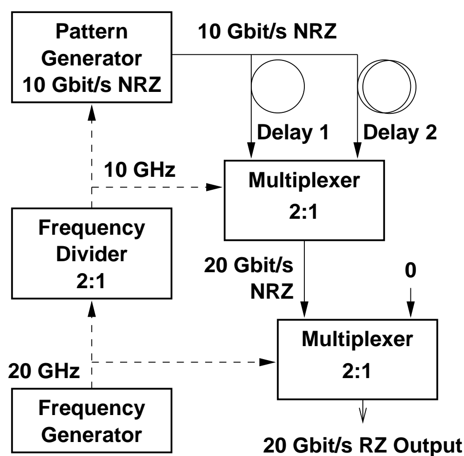

Fig. 9: Schematic multiplexer setup for the generation of electrical RZ signals at a data rate of 20 Gbit/s.

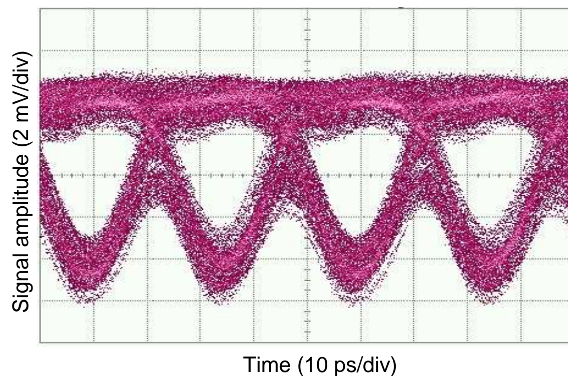

Fig. 10: Measured optical eye diagram at 20 Gbit/s RZ data rate. LD current and EAM bias are 70 mA and −2 V, respectively.

7. Non-Return-to-Zero Modulation at 40 Gbit/s

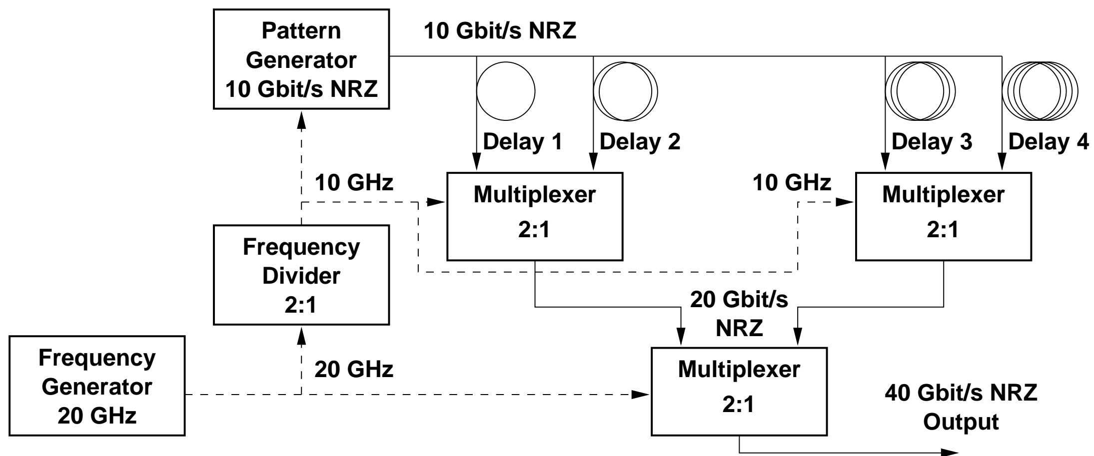

Fig. 11: Schematic multiplexer setup for the generation of electrical NRZ signals at a data rate of 40 Gbit/s.

An electrical 40 Gbit/s NRZ signal is generated by a two-stage multiplexer system which is schematically shown in Fig. 11. An additional 40 GHz bandwidth amplifier is used and its saturated output (see Fig. 12) is attenuated to 1 V_{pp} and fed with a microwave probe to the ground–signal–ground contacts of the EAM (see Fig. 5). The EAM is biased by means of a second microwave probe which is connected to a bias tee and an RF load terminating the electrical path. Data transmission with an open eye diagram according to Fig. 13 has been achieved at low optical power using averaging. At present, the eye opening is limited by the 3-dB modulation bandwidth of 25 GHz which is expected to increase with a more advanced microwave design in the future.

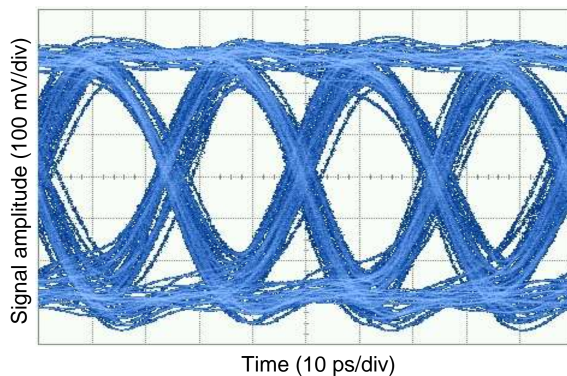

Fig. 12: Measured eye diagram of the electrical NRZ signal at a data rate of 40 Gbit/s.

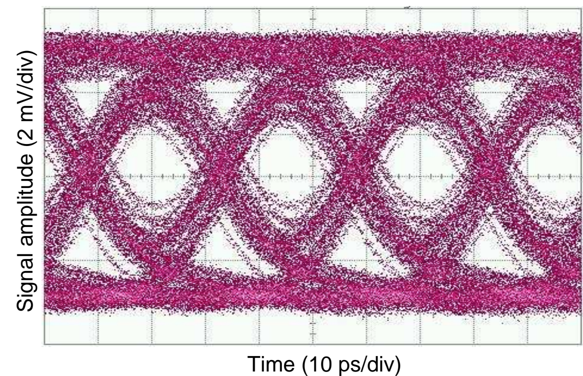

Fig. 13: Measured optical eye diagram of the NRZ signal at a data rate of 40 Gbit/s. Laser current and EAM bias are 50 mA and −1 V, respectively.

8. Conclusion

We have demonstrated that monolithically integrated DFB-LD–EAMs using an identical InGaAlAs QW structure show sufficiently fast transitions for 40 Gbit/s applications. The eye opening is well correlated to the simulated and measured electro-optical response. Due to the small signal-to-noise ratio (SNR) at the detector, quasi error-free data transmission has not been achieved up to now. Incorporating an additional SOA, which might be monolithically integrated as well, an improved SNR is to be expected from future device generations.

References

[1] R. Lewén, S. Irmscher, U. Westergren, L. Thylén, and U. Eriksson, "Ultra high-speed segmented traveling-wave electroabsorption modulators," in Proc. *Optical Fiber Communications Conf., OFC 2003*, postdeadline paper PD38. Atlanta, GA, USA, February 2003.

[2] B. Stegmueller and C. Hanke, "Integrated 1.3 μm DFB laser electroabsorption modulator based on identical MWQ double-stack active layer with 25 GHz modulation performance," *IEEE Photon. Technol. Lett.*, vol. 15, no. 8, pp. 1029–1031, 2003.

[3] M. Peschke, T. Knoedl, and B. Stegmueller, "Simulation and design of an active MQW layer with high static gain and absorption modulation," in Proc. *Numerical Simulation of Semiconductor Devices, NUSOD-03*, pp. 15–16. Tokyo, Japan, October 2003.

[4] T. Knoedl, C. Hanke, B.K. Saravanan, M. Peschke, R. Schreiner, and B. Stegmueller, "Integrated 1.3 μm InGaAlAs–InP laser-modulator with double-stack MQW layer structure," in *Integrated Optics and Photonics Integrated Circuits,* G.C. Righini, S. Honkanen (Eds.), SPIE Proc. 5451, pp. 1–7, 2004.

[5] P. Gerlach, M. Peschke, C. Hanke, B.K. Saravanan, and R. Michalzik, "High-frequency analysis of laser-integrated lumped electroabsorption modulators," *IEE Proceedings Optoelectronics*, vol. 152, 2005, in press.

Investigation of the Capacitance of Integrated DFB–EAMs with Shared Active Layer for 40 GHz Bandwidth

Martin Peschke*

Laser-integrated electroabsorption modulators with shared active area are potentially inexpensive high-speed light sources but suffer from certain design drawbacks. It is shown how to increase the cut-off frequency beyond 40 GHz without losing fabrication simplicity.

1. Introduction

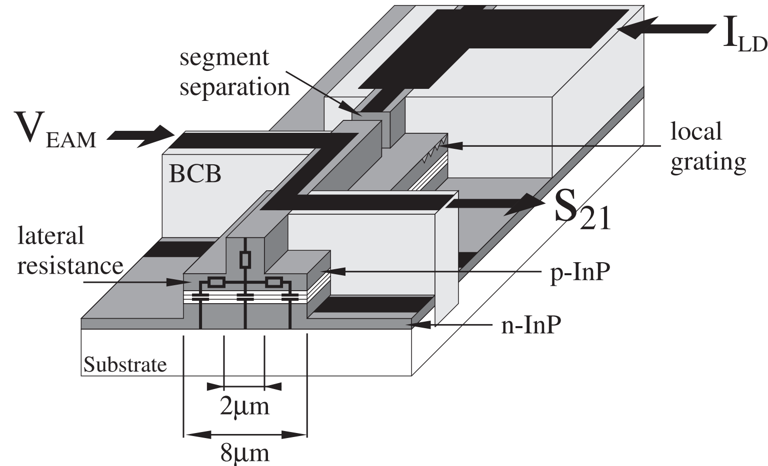

Fig. 1: Integrated DFB–EAM device layout.

Electroabsorption modulators (EAMs) integrated with distributed feedback (DFB) lasers are attractive light sources for modulation speeds up to the 40 Gbit/s regime and beyond. In contrast to other realizations [1], devices with a common active area are of particular interest as their growth and fabrication complexity is comparable to standard DFB lasers. However, the concept of a single grown active area imposes two major challenges on the EAM design: First, the operating wavelength has to be close to the bandgap in order to achieve sufficient gain in the DFB section for low laser threshold currents. Therefore, the residual absorption in the EAM is high and the bias voltage is limited to low values

*Work performed in collaboration with Infineon Technologies AG, Munich, Germany

for sufficient output power. Both can result in serious carrier pile-up effects. Second, the DFB grating layer acts as an etch stop layer during the ridge fabrication process in both sections. The spacing between the grating layer and the waveguide is d_{sp} =150 nm to optimize the coupling coefficient in the laser section. The consequence is an unwanted lateral conductance in the EAM section. With decreasing modulation frequency the effective capacitance gets larger and degrades the RF performance ('field spreading'). After recognizing a poor RF performance of the first generation DFB–EAMs, a model was developed that considers intrinsic and extrinsic device parameters. With this model, the small-signal measurements could be verified and design rules were identified.

2. First Device Generation

The reported investigations were carried out on a monolithically integrated DFB–EAM. The device schematic is displayed in Fig. 1. A detailed report on the fabrication steps is given in [1]. The active area consists of a single grown AlGaInAs double quantum well (QW) stack on n-InP substrate that is able to deliver high gain with forward current injection and high absorption swing with reverse bias voltage at 1308 nm operation wavelength [2]. The intrinsic area is 270 nm thick. A local buried grating is introduced in the 380 µm long DFB section. Lateral waveguiding is performed by a 2 µm wide ridge on top of a 8 µm wide second mesa. The EAM section is 100 µm long. The specific resistance of the p-region is $\rho_{\mathrm{p}} = 0.25\,\Omega\mathrm{cm}$. The device showed a threshold current of 18 mA, a maximum output power of 1 mW and an extinction ratio of 10 dB/V in the EAM section.

3. Simulation and Measurement Results

In a well designed EAM, the steady state carrier distribution is reached after a few ps. For the modulation behavior up to 50 GHz, the active area can be modeled as a variable capacitor $C(V_{\mathrm{EAM}}, P_{\mathrm{abs}})$ depending on the absorbed optical power P_{abs} and the reverse bias V_{EAM}. Stationary reverse band diagrams (Fig. 2) were calculated by a 1D drift-diffusion semiconductor simulation [2] that additionally features a carrier generation term, field dependent QW escape time constants and carrier mobilities including saturation velocity. Figure 3 displays the simulated capacitance per area of the active region together with measurement results. Without input light, the capacitance decreases with reverse bias as the space charge region (SCR) increases. With optical input, photo carriers are generated and separated by the electrical field. Similar to a dielectric in a capacitor they create a screening field that weakens the initial field and increases the capacitance. For low reverse bias voltages and high optical power, the effect escalates as soon as the screening field gets into the order of magnitude of the initial field and carriers do not reach saturation velocity anymore. In the next step, the calculated capacitance is introduced into the equivalent circuit model of Fig. 4 that accounts for field spreading, parasitic pad capacitance and the electrical measurement setup. Figure 5 shows simulated and measured electrical small-signal graphs of the EAM traveling wave contact which are in excellent agreement. While

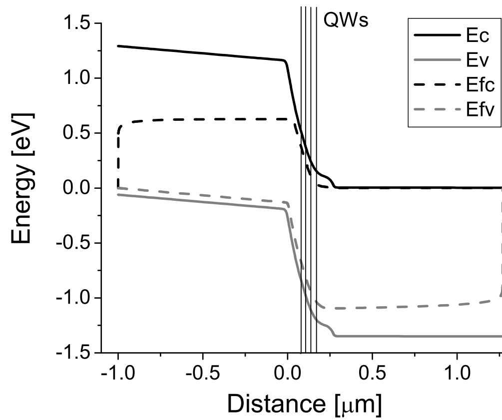

Fig. 2: Band structure of EAM at $V_{\text{EAM}} = 0\,\text{V}$ and $P_{\text{abs}} = 10\,\text{mW}$.

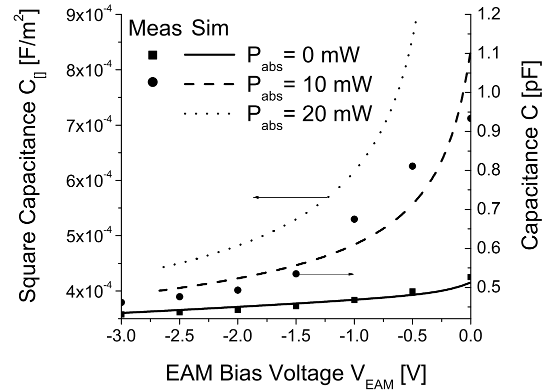

Fig. 3: Measured and simulated capacitance of the pin-structure.

the bandwidth is almost independent of the optical power at −2 V EAM bias, it is cut in half at 0 V bias and 60 mA laser current due to carrier pile-up. All graphs show a major decrease in response below 10 GHz caused by field spreading at low frequencies. With the first layout, the bandwidth is limited to approximately 18 GHz.

4. Redesign

For the redesign, three major changes were introduced: First, the structure was grown on semi-insulating substrate reducing the pad capacitance. Second, the 2 μm wide EAM ridge was etched through the active region with a nitrogen-based dry-etching process.

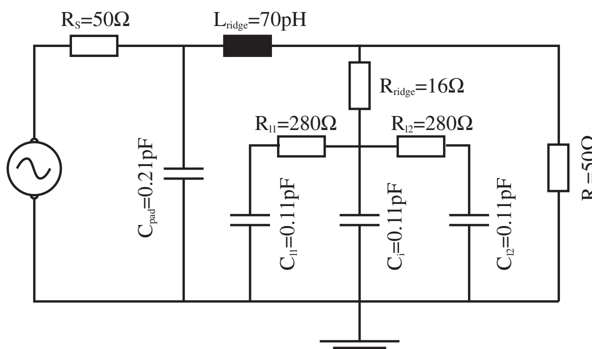

Fig. 4: Equivalent circuit model of the EAM.

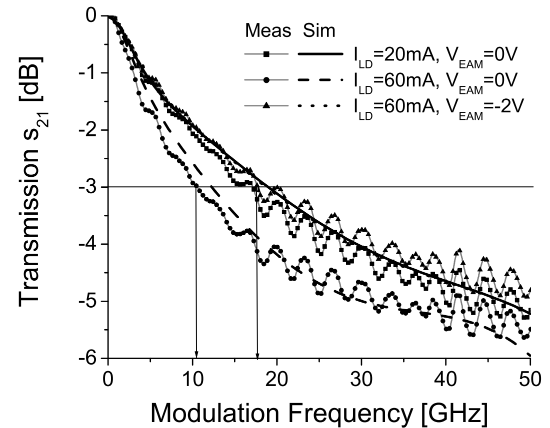

Fig. 5: Measured and simulated electrical transmission s_{21}.

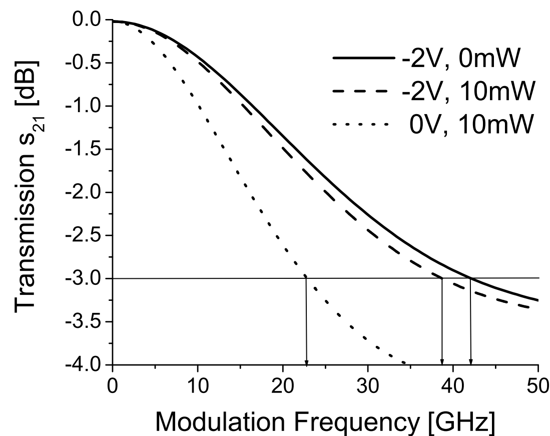

Fig. 6: Prediction of s_{21} with 2 µm wide ridge and feedlines on semi-insulating substrate.

Third, the detuning of the DFB wavelength to the QW photoluminescence was increased, thus sacrificing laser threshold for less residual absorption at reverse EAM bias voltage. The corresponding small-signal predictions are shown in Fig. 6. Modulation bandwidths of 40 GHz are accessible with reasonable output power and laser threshold. In fact, first experimental results have shown 41 GHz optical bandwidth, 31 mA laser threshold current and 1 mW optical output power.

5. Conclusion

We have developed a simulation tool to study the small-signal performance of EAMs taking into account intrinsic carrier phenomena as well as extrinsic parasitics. Simulation results are in excellent agreement with measured data and allow for detailed insight in carrier pile-up and field spreading related effects. By design optimization, the 3 dB bandwidth of the device was boosted from 18 to 41 GHz. To our knowledge, this is the first integrated DFB–EAM at 1300 nm operating wavelength exceeding 40 GHz in bandwidth.

References

[1] B. Stegmueller and C. Hanke, "Integrated 1.3 µm DFB laser electroabsorption modulator based on identical MQW double-stack active layer with 25 GHz modulation performance," *IEEE Photon. Technol. Lett.*, vol. 15, no. 8, pp. 1029–1031, 2003.

[2] M. Peschke, T. Knoedl, and B. Stegmueller, "Simulation and design of an active MQW layer with high static gain and absorption modulation," in Proc. *Numerical Simulation of Semiconductor Devices, NUSOD-03*, pp. 15–16. Tokyo, Japan, October 2003.

Hydride Vapor Phase Epitaxial Growth of Thick GaN Layers With Improved Surface Flatness

Peter Brückner

Thick GaN layers have been grown by hydride vapor phase epitaxy (HVPE) on different GaN templates grown by metalorganic vapor phase epitaxy. Crack formation could be reduced by using a hydrogen/nitrogen carrier gas mixture. By carefully optimizing the growth conditions in the final stage of the process, excellent surface morphologies could be obtained at still acceptably high growth rates. Up to 300 μm thick crack-free HVPE layers with a mirror like surface could be grown on our FACELO templates.

1. Introduction

Although the recent years have seen a tremendous development of short wavelength opto-electronic and electronic devices based on GaN and related materials, the further improvement of such devices is still limited by the fact that epitaxial structures have to be grown on foreign substrates like sapphire, SiC, or Si, because high quality bulk GaN wafers are not yet really available. Therefore, the heteroepitaxial growth of thick GaN layers by hydride vapor phase epitaxy (HVPE) has been developed in several groups [1] which can be used as substrates for subsequent device epitaxy. As we have observed on thin GaN layers grown by metalorganic vapor phase epitaxy, the residual strain depends strongly on the nucleation method: When an AlN nucleation layer is used, the GaN layer exhibits large compressive strain whereas samples with a low temperature GaN nucleation layer - the mostly used method - show much lower strain at room temperature. GaN layers of these types are often used as templates for the deposition of thicker GaN layers by HVPE. Thus, it is interesting to evaluate whether the strain state of these templates may influence the final strain or other properties of the HVPE layers.

Therefore, we have investigated the HVPE growth of thick GaN layers on different GaN templates. Besides the cracking behavior, our studies focus also on the surface morphology problem and its relation to the template properties. Such studies require an optimization of all growth parameters to achieve an excellent surface morphology.

2. Experimental

All HVPE layers have been grown on GaN templates grown on 2-inch-sapphire by MOVPE. This enabled an efficient optimization of the basic growth parameters without the need to optimize the HVPE nucleation process. In order to investigate the influence of the template type and quality, up to 4 different templates could be overgrown simultaneously in one HVPE run to get rid of the parameter drift in the reactor. The bare templates and the overgrown samples with typical layer thicknesses between 40 and 140 µm have been characterized by standard tools like optical microscopy, high resolution x-ray diffraction (HRXRD), low-temperature photoluminescence (PL) and atomic force microscopy (AFM).

3. Results and Discussion

3.1 Influence of the growth conditions

We have first studied the influence of some basic epitaxial parameters as it is described in [2]. These parameters are the mixture of the carrier gas, the V/III ratio and the reactor pressure. We found that the composition of the carrier gas is of major importance for the growth of thick layers, whereas it has only a small influence on the surface morphology. The most important parameters for a change in the surface morphology are the V/III-ratio and the reactor pressure. At higher V/III-ratio more hillocks are visible, but for lower ratios the growth rate decreases. At lower pressures, the surface morphology could be improved, whereas higher pressures resulted in larger growth rates due to the reduced gas velocity. Similar trends have peen observed for the V/III-ratio.

These findings led us to the optimization of a 2-step growth procedure: The main part of our thick GaN layers was growth at those conditions favoring large growth rates, whereas in the very last stage, we reduced pressure and V/III-ratio which resulted in significantly improved surface morphologies.

3.2 Influence of the template

As already pointed out, we have done these growth studies on templates, i.e. on thin GaN layers grown by MOVPE in order to get rid of the difficulty of developing a nucleation process in our HVPE system. Several templates were available for these studies which had been grown in different laboratories, but had nominally very similar structures. Standard characterization methods also seemed to confirm their equivalence. However, we observed strong differences of the HVPE grown GaN layers regarding surface morphology and cracking behavior.

As mentioned, low temperature PL and HRXRD measurements showed that the GaN templates grown on AlN nucleation layers are strongly compressively strained: We found the PL signal of the donor bound exciton (D_0, X) typically at 3.492 eV (fig. 1), which

corresponds to a relative dilatation of the c lattice constant of $\epsilon_\perp = \Delta c/c \approx 1.3 \cdot 10^{-3}$ as a consequence of the biaxial compressive strain in the c-plane. This strain is probably mainly due to the thermal mismatch between the GaN layer and the sapphire substrate, indicating that the layer is fairly unstrained at the growth temperature. In contrast, the templates with a GaN nucleation layer show much lower strain of $\epsilon_\perp \approx 7 \cdot 10^{-4}$, corresponding to a (D_0, X) peak position of about 3.482 eV (fig. 1).

Besides the different nucleation, the templates were grown identically. Indeed, the HVPE layers grown on these two types of templates show very similar surface morphology. As measured by PL, the strain difference is still seen after epitaxy, although both layers are now fairly unstrained with the (D_0, X) peak being close to 3.471 eV (fig. 1 b). However, the tendency to form cracks, if not grown under perfect conditions, is much more pronounced for the template U1 (GaN nucleation) whereas template U2 is still free of cracks. This may be a consequence of the strain-free situation at growth temperature, whereas the layers on the GaN nucleation are obviously strained tensely at these high temperatures and thus may form cracks during cool down.

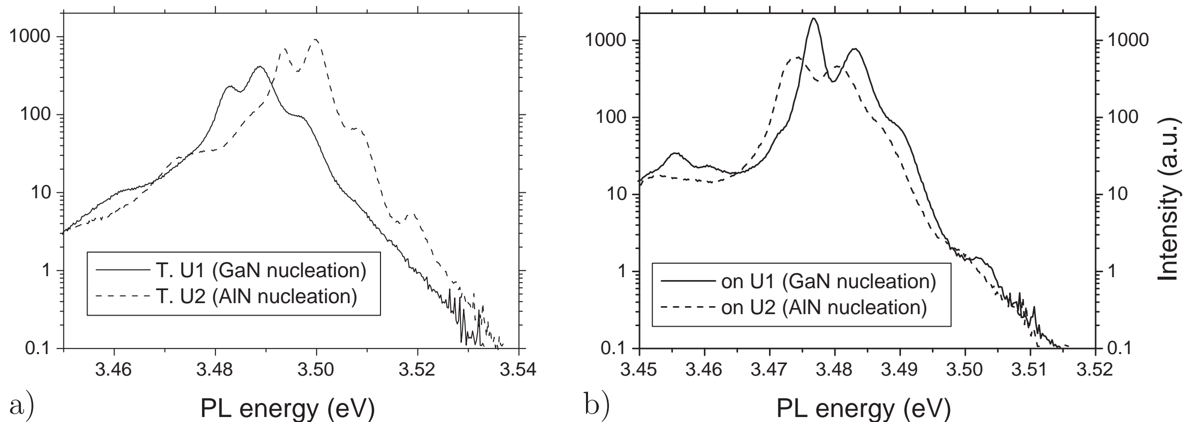

Fig. 1: PL spectra ($T = 15$ K) of the bare templates (a) and 40 μm thick HVPE layers grown on them (b).

3.3 Growth on a FACELO-template

When we apply the optimized HVPE process on our FACELO-templates, we were able to increase the final thickness before cracking significantly. The FACELO-process itself is described more precisely in [3].

Even if we start with a fairly rough surface (fig. 2 (a)) more than 130 μm thick HVPE layers (fig. 2 (b)) with improved surface morphology and better crystalline quality compared to the FACELO-template could be grown. On the FACELO-templates, a typical wing-tilt of 0,5° was observed, whereas no wing-tilt was measurable after the HVPE growth.

Finally, we were able to grow up to 300 μm GaN directly on such a FACELO-template. For the evaluation of these layer, we have to take care about the wafer curvature, which

is mainly caused by the different thermal expansion coefficients between sapphire and GaN during cool down. Because of the non circular symmetry of our stripe-mask for the FACELO-template, two different bowing radius developed with 75 cm parallel to the stripes and 40 cm perpendicular to them. In spite of the strong curvature these layers are stable and crack free.

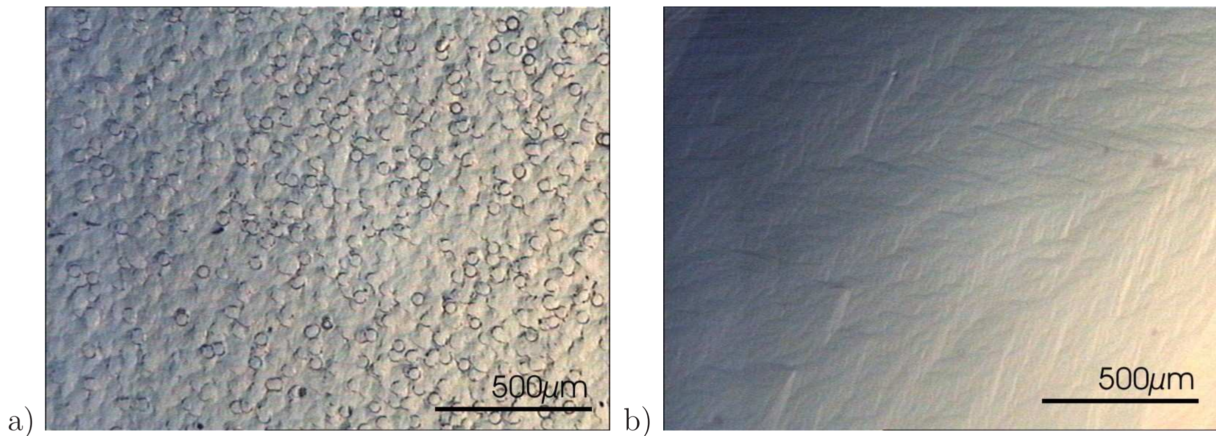

Fig. 2: Optical Nomarski interference micrograph of the surface of a 130 μm HVPE layer (b) grown on a lower quality FACELO-template (a)

4. Summary

By optimizing the growth parameters of our HVPE process, we could significantly improve the quality of thick GaN layers. The tendency to form cracks could be further reduced by applying compressively strained GaN templates grown on an AlN nucleation layer. We could demonstrate that a thorough optimization at the end of the growth-process could significantly improve the surface morphology. Therefore we were able to grow up to 300 μm GaN crack-free on a FACELO-template.

References

[1] X. Xu, R.P. Vaudo, C. Loria, A. Salant, G.R. Brandes, and J. Chaudhuri, "Growth and characterization of low defect GaN by hydride vapor phase epitay," *J. Crystal Growth*, vol. 1-3, no. 246, p. 223, 2002.

[2] F. Habel, "Investigations of the Carrier Gas Composition for HVPE of GaN," *Annual Report 2003, Optoelectronics Department, University of Ulm*, pp. 77–80, 2003.

[3] F. Habel, "Optimization of GaN FACELO Structures using Marker Layers," *Annual Report 2004, Optoelectronics Department, University of Ulm*, 2004.

Optimization of GaN FACELO Structures Using Marker Layers

Frank Habel

The FACELO technique was used to further reduce the dislocation density of GaN layers. AlGaN and Si-doped GaN layers were implemented as marker layers during GaN epitaxial growth in order to get a deeper scientific understanding of the growth process. Both types of marker layers show a good visibility without any parasitic influences on the crystal structure or growth behavior. These marker layers were used to study the development of the different crystal facets as growth proceeds. This technique provided access to a precise control of a multistep growth sequence, enabling a thorough optimization of our FACELO process by inserting additional properly designed growth steps.

1. Introduction

Due to the rapid progress in the development of high-end GaN based devices such as laser diodes, ultra violet light emitting diodes and field effect transistors, the role of threading dislocations is getting more and more important. The dislocation density in common heteroepitaxially grown GaN on sapphire or silicon carbide substrates is in the order of 10^8-10^{10} cm^{-2}, due to the lattice mismatch between these substrates and GaN together with the resulting columnar structure of the grown layers. Dislocations have several strong effects on devices. Especially for laser diodes, a low dislocation density is a prerequisite for long device lifetimes. Moreover, dislocations act as non-radiative recombination centers [1], reducing the efficiency of optoelectronic devices especially in the violet and UV range [2]. Carrier mobility is affected by scattering at charged dislocation lines. The formation of V-defects during growth of InGaN quantum wells is correlated with dislocations [3]. One of the most promising techniques to reduce the dislocation density is the growth on structured substrates. The basic method is epitaxial lateral overgrowth (ELOG) [4], which benefits from the fact, that dislocations usually run vertically from the substrate interface right to the surface of the semiconductor layer, whereas laterally grown crystal areas are nearly dislocation free. An advanced method is the facet assisted epitaxial lateral overgrowth (FACELO), where the propagation of the dislocations is affected by appropriate control of the dominating crystal facets during growth. This method requires a fairly complex variation of the epitaxial parameters during growth to enable optimized vertical and lateral growth at different times of the process. However, from the final layer properties, it is very difficult to judge the success of some optimization procedure of an intermediate growth step. This problem can be overcome by the use of marker layers

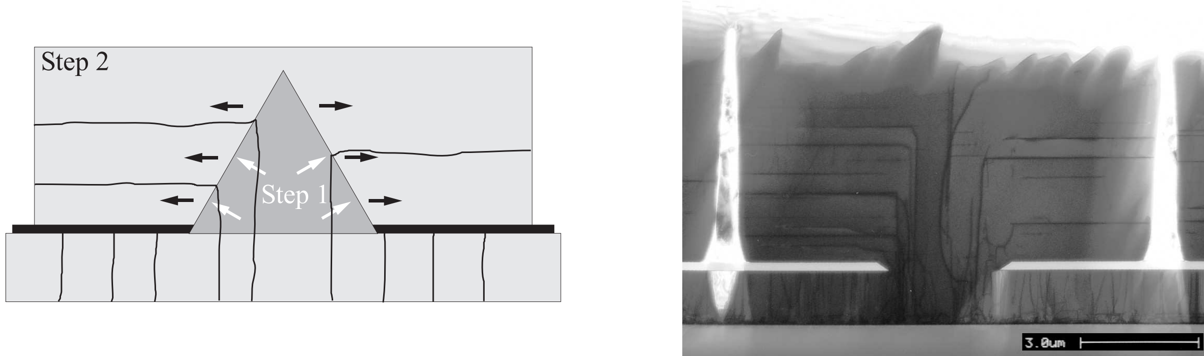

Fig. 1: Schematic drawing of a FACELO structure (left) and corresponding TEM image (right) showing the bending of the threading dislocations.

which make visible how the growth proceeds [5]. Therefore, we have studied AlGaN and Si doped marker layers in order to optimize our FACELO process by implementing additional, specially designed growth steps.

2. FACELO

The FACELO process is a further development of the ELO technique. Therefore, the samples have to be prepared in the same way. For the structured substrates 1 μm thick GaN layers on sapphire were used as templates. They were covered with a 250 nm thick SiO_2 mask deposited by PECVD. By standard lithography and dry etching in a CF_4 RIE system 3–8 μm wide stripes have been opened. The structured growth was performed by metalorganic vapor phase epitaxy in an Aixtron 200/4 RFS horizontal reactor system. The basic investigations of structured growth have already been published [5]. For the FACELO process at least two growth steps are required as it is shown in figure 1a. In the first step, a triangular shaped cross section is formed, confined by $\{11\bar{2}2\}$ facets. This structure is achieved using a low growth temperature of about 1020°C. In the next step the temperature is raised and the growth parameters are adjusted to obtain a high lateral growth rate. This change form vertical to lateral growth leads to a change of the propagation direction of the threading dislocations. The dislocations are bent at the interface of the triangular structure and continue horizontally, the material above this structure is completely dislocation free (fig. 1b).

In figure 2 the distribution of dislocations of FACELO samples is shown. For 8 μm wide mask openings the triangular structure was not completed yet, so a stripe with a high dislocation density is still found. In contrast, above the 4 μm wide mask openings almost no dislocations were found, the dislocation density in this are is in the range of $10^6 cm^{-2}$. This excellent value demonstrates the successful realization of the FACELO process.

Unfortunately, these samples showed a macroscopically rough surface morphology. This challenge can be overcome by implementing additional growth steps to level the surface.

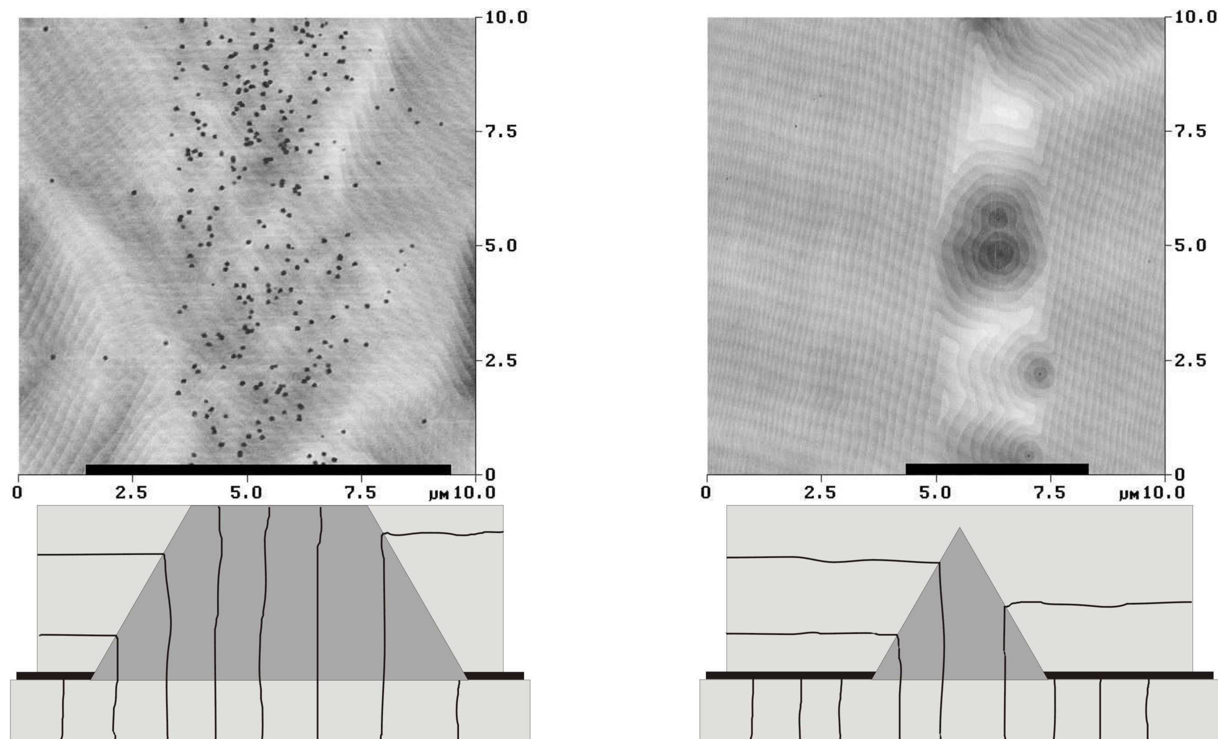

Fig. 2: Distribution of dislocations of FACELO samples depending on the mask opening determined using an HCl etching technique. Mask opening is marked by black bar.

In order to optimize and control several growth steps, it is necessary to have a method to analyze every single step. Therefore we implemented the marker layer technique.

3. Marker Layers

During epitaxial growth TMAl or silane was periodically added to the reactor for 1.5 minutes in order to form a periodic pattern of AlGaN or Si-doped GaN, respectively. The resulting thickness of these marker layers was between 50 and 200 nm , depending on the different growth rates for different crystal facets and growth parameters. After growth the cross sections of the samples were analyzed using a scanning electron microscope. The AlGaN layers could be detected for an aluminium content of 3% and were clearly visible for an aluminium content of 10%. Similarly, the n-doped layers were already visible for a silicon concentration of $1{\times}10^{19}\mathrm{cm}^{-3}$ and showed a good visibility for a higher silicon concentration of $5{\times}10^{19}\mathrm{cm}^{-3}$ (figure 3a). The given numbers are nominal values corresponding to growth of plane layers in c-direction, as the exact concentration values may be different for growth in different crystal directions and depend also on the mask structure.

These concentrations obviously did not affect the normal GaN growth process, as has been checked additionally by cathodoluminescence (CL, performed by T. Riemann and

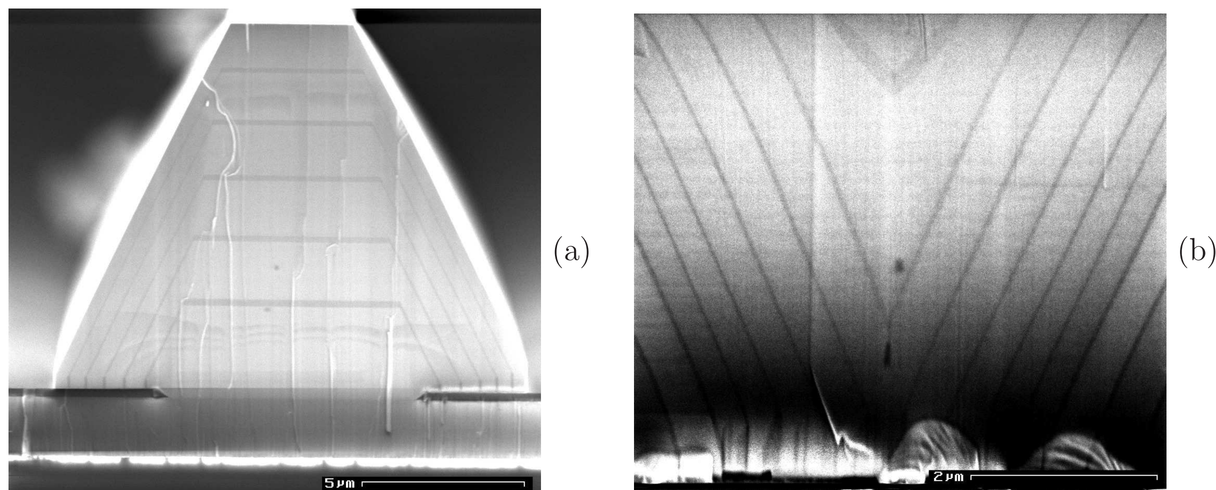

Fig. 3: GaN:Si marker layers make the propagation of the facets visible (a). Increased growth rate at coalescence region (b).

J. Christen, Otto-von-Guericke University Magdeburg): The marker layers could also be detected, but for both types neither a decrease in CL intensity nor a strain induced shift of the CL wavelength was found in the GaN material between the marker layers. The surface morphology was investigated using an optical microscope. Again no difference in morphology was found between samples grown with and without marker layers. Nevertheless, we did not study higher concentrations in order not to introduce any parasitic growth effects.

In cross sectional SEM scans of the samples, each marker layer directly indicates the position and shape of the growing facet for the respective point in time. As the growth time between two marker layers is known and the thickness of the deposited material can easily be measured, the growth rates can be calculated. If several growth steps with different parameters are used, this method provides direct access to the growth rates for each crystal direction and each set of parameters in only one growth run. Therefore the number of growth experiments can be drastically reduced, which otherwise would be necessary to study the influence of different growth parameters on the local growth rate. This technique also allows deeper insight in several growth details. For example, an increase of the growth rate was observed at the coalescence region (fig. 3b). Moreover, the development of some unwanted growth features could be monitored. We could unambiguously observe that the propagation of inverse pyramidal shaped growth defects originate already from the template surface. The full potential of the marker layer technique becomes evident when epitaxial growth consisting of several different growth steps is developed.

3.1 Multi-Step Growth

Obviously, an improvement of these FACELO structures is possible when a growth sequence consisting of even more steps is used. For example, the low temperature growth

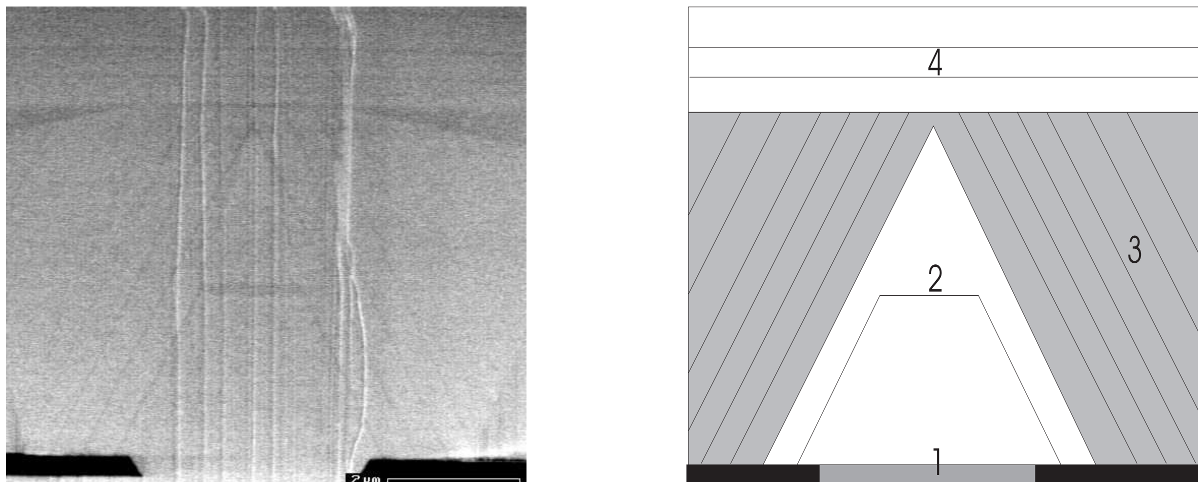

Fig. 4: SEM scan and schematic of a multi step FACELO sample.

step used for the triangular structures may cause growth defects when carried out as first step directly on the structured template. As the crystal quality decreases when the growth rate becomes too high, a reduced growth rate during coalescence leads to improved results. After coalescence another set of growth parameters may be used to get an improved surface morphology. On the other hand, the control of the growth sequence gets more difficult when the number of growth steps is increased. The accurate timing of a multi step growth sequence is much more sensitive. Although the basic effects of the main growth parameters like temperature, pressure and V-III ratio on growth in different crystal directions are fairly well known [4], these data are not precise enough to describe the exact behavior of the propagating facets when the main parameters are changed during growth. In order to develop a multi step growth sequence using conventional tools, a tremendous number of experiments is necessary, as each step has to be optimized in a separate series of growth runs. The marker layer technique allows the optimization of all growth steps simultaneously in a few experiments, as a correlation between the different growth steps and the grown facets is possible for every point in time. Based on that technique we further improved our FACELO structure. In figure 4 a SEM scan and the corresponding schematic of the cross section of such a multi step FACELO sample are depicted. Due to the marker layers, all growth steps are clearly visible. At first, growth is initiated with standard GaN parameters (high temperature, standard pressure, standard V-III ratio). Then the triangular section is formed using a decreased growth temperature. In the next step, the lateral overgrowth is favored by lowering the reactor pressure and increasing the V-III ratio. In the final growth step, the temperature is raised again after coalescence in order to level the surface and to improve the morphology. Every single step has been individually optimized in a few preceding experiments. As can be easily seen, the triangular structure has been completed up to the tip, so the FACELO technique was carried out completely. Therefore the marker layer method enabled us to develop a multi step growth sequence to grow complete 2 inch wafers with low dislocation density and excellent surface morphology (figure 5).

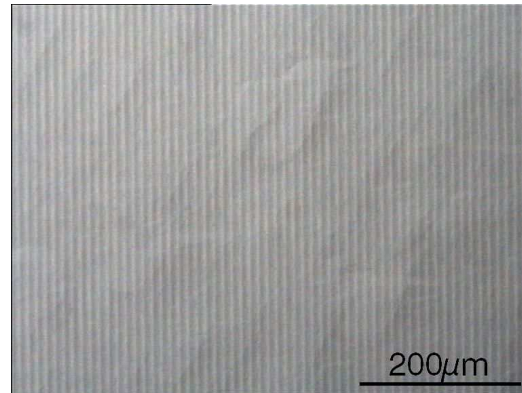

Fig. 5: Excellent surface morphology of a multi step FACELO sample.

4. Conclusion

GaN:Si and AlGaN layers were implemented as marker layers for the epitaxial growth of GaN on structured substrates. For a silicon concentrations of $5 \times 10^{19}\mathrm{cm}^{-3}$ or an aluminium content of 10%, the marker layers are well visible in SEM scans. On the other hand, no parasitic side effects on the crystal quality or surface morphology were found. The marker layers provide direct access to the propagating growth facets in different crystal directions and under different growth conditions. Therefore, this technique is an outstanding tool for the development of multistep growth sequences thus enabling us to grow low dislocation density GaN with excellent surface morphology on full 2 inch structured substrates.

References

[1] D. Cherns, S.J. Henley, and F.A. Ponce, "Edge and screw dislocations as nonradiative centers in InGaN/GaN quantum well luminescence," *Appl. Phys. Lett.*, vol. 78, no. 18, pp. 2691–2693, 2001.

[2] T. Stephan, M. Kunzer, P. Schlotter, W. Pletschen, H. Obloh, S. Müller, K. Köhler, and J. Wagner, "Importance of Nonradiative Recombination Processes in Violet/UV InGaN Light Emitting Diodes," *phys. stat. sol. (a)*, vol. 194, no. 2, pp. 568–571, 2002.

[3] J.S. Speck and S.J. Rosner, "The role of threading dislocations in the physical properties of GaN and its alloys," *Physica B*, vol. 273–274, pp. 24–32, 1999.

[4] B. Beaumont, Ph. Vennegues, and P. Gibart, "Epitaxial Lateral Overgrowth of GaN," *phys. stat. sol. (b)*, vol. 227, no. 1, pp. 1–43, 2001.

[5] F. Habel, "Dislocation Reduction by GaN MOVPE Growth on Structured Substrates," in *Annual Report, Optoelectronics Department, University of Ulm*, pp. 3–6, 2002.

Epitaxial Growth of High Al-Containing AlGaN and AlN Layers With MOVPE

Christoph Kirchner

We report on the epitaxial growth of AlN- and high aluminum containing AlGaN-layers with MOVPE. The growth process of such layers is much more crucial than for GaN growth. The difficulties like achieving a good material quality, undesired prereactions in the gas phase and low growth rates are discussed. Layers of $Al_xGa_{1-x}N$ with Al-contents x up to 80 % and pure AlN have been succesfully grown. First results of epitaxial layer characterization are presented.

1. Introduction

High aluminum containing AlGaN an AlN layers are of increasing interest for the III-V nitride device technology. Important applications are e.g. UV-LEDs and solar blind UV-detectors [1], [2]. Such devices have a broad application range on the field of sensors and spectroscopy, e.g. environmental analytics, UV-desinfection of water or as excitation source for photochemical reactions (hardening of polymers). For emission wavelengths below 365 nm it is mandatory to use AlGaN layers in the active regions as recombination areas. Depending on the desired wavelenght, Al-contents up to 50 % are necessary (UV-LEDs with $\lambda_p = 270$ nm emission wavelength). Due to enhanced absorption in the p-type GaN layers for wavelenghts below 350 nm, the outcoupling of light must be realized trough the transparent sapphire substrate. This means, that all layers between the active region and the substrate must be transparent, too. Therefore, the Al-contents in these layers must be higher than in the active layers, in extreme cases pure AlN is mandatory. Another interesting field of applications are AlN/GaN quantum cascade lasers, which are using intersubband transitions for near-, mid- and far infrared emission [3]. Fabrication of such device structures becomes more and more critical with decreasing wavelenghts, because crystalline and optical quality of nitride layers decreases with increasing Al-contents [4].

One major problem during epitaxy of AlN and AlGaN with high Al-content by MOVPE is the strong reactivity of the metalorganic aluminum source TMAl (trimethylaluminum): parasitic reactions between ammonia and TMAl result in depletion of the gas phase leading to a strongly reduced growth rate. In extreme cases, formation of small AlN crystallites in the gas phase occur, which are falling on the substrates and strongly influence the layer quality. Our experiments show that the prereactions can be reduced by appropriate choice of the growth parameters, but not completely avoided. A very important parameter is the reactor pressure, which has to be strongly reduced for AlN growth. In spite of this parameter optimization, growth rate remains quite small.

2. Experimental

Epitaxial growth of high Al-containing compound AlGaN and AlN semiconductor films is conducted in a single wafer, radio-frequency heated, horizontal type, water cooled quartz reactor MOVPE system (Aixtron AIX 200 RF) operated at low pressure. The MOVPE system is equipped with a reflectometer system consisting of a white light source and a CCD spectrometer. This measurement system allows in situ reflectometry during epitaxial growth for determining growth rates and surface development, which is a helpful tool for process development. Trimethylgallium (TMGa), trimethylaluminum (TMAl) and ammonia (NH_3) are used as group III and group V precursors, respectively. All growth experiments are performed on c-plane sapphire (Al_2O_3), using a low temperature nucleation layer process before the main layer growth.

2.1 Epitaxial growth of AlGaN

A low pressure epitaxy process allows successful growth of AlGaN with Al-contents up to 80%. Fig. 1 shows Al-incorporation in the solid (determined by high resolution x-ray diffraction (HRXRD)) vs. the molar TMAl/TMGa ratio at a pressure of 50 mbar. Molar flows of TMGa and TMAl were varied in a range of 3.5 - 45 μmol/min and 25 - 90 μmol/min, respectively. As can be seen, a very high Al/Ga ratio in the gas phase is necessary even at such low pressures to achieve a high aluminum content in the solid. Problems arise from the high reactivity of TMAl: Only low growth pressures allow significant Al-incorporation. Pressures, which are usually used for the growth of GaN (150 - 200 mbar), result in nearly zero growth rate. Pressures above 300 mbar result in spontaneous formation of small AlN crystallites in the gas phase, which are falling on the substrates, destroying the layer surface. The crystal quality of the low-pressure grown AlGaN-layers is quite good, which can be seen from fig. 2, where a 2Θ - ω HRXRD scan is plotted. The measured structure consists of a 1 μm thick undoped GaN layer, grown on sapphire with a low temperature GaN nucleation layer, and a 100 nm thick $Al_{0.8}Ga_{0.2}N$ layer. The peaks from the underlying GaN-layer and the AlGaN peak can be clearly resolved. FWHM is 230 arcsec for the GaN layer and 350 arcsec for the AlGaN-layer, respectively.

2.2 Epitaxial growth of AlN

The above mentioned problems are even more significant for the growth of pure AlN. Epitaxial growth of AlN shows a very low growth rate. Enhanced prereactions in the reactor are depleting the gas phase before reaching the substrate. Only at pressures of 50 mbar and below, significant growth rates are observed. At 25 mbar, a fairly large growth rate of 550 nm/hr could be achieved. With even lower reactor pressures a higher growth rate might be reached, but the minimum reactor pressure is limited by the pumping system. In fig. 3, the AlN growth rate is plotted against the reactor pressure, while the other parameters are kept konstant. All AlN-layers are grown with a low temperature

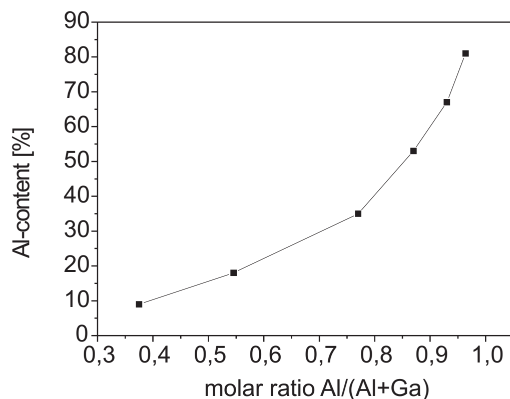

Fig. 1: Al-content in $Al_xGa_{1-x}N$ vs. molar TMAl/TMGa-ratio at a reactor pressure of 50 mbar.

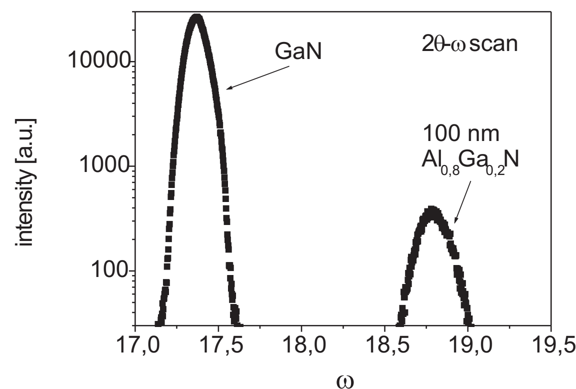

Fig. 2: HRXRD-scan (2Θ - ω) of 100 nm thick $Al_{0.8}Ga_{0.2}N$, grown on GaN.

AlN-nucleation layer. The analysis of the AlN layers with HRXRD reveals a quite good crystal quality, as can be seen from fig. 4, where a rocking curve of undoped AlN is shown.

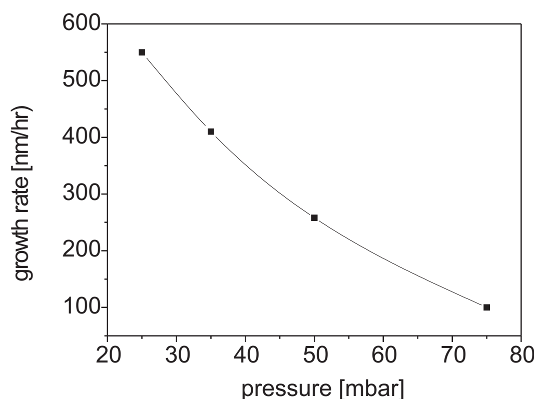

Fig. 3: MOVPE growth rate of epitaxial AlN plotted versus reactor pressure.

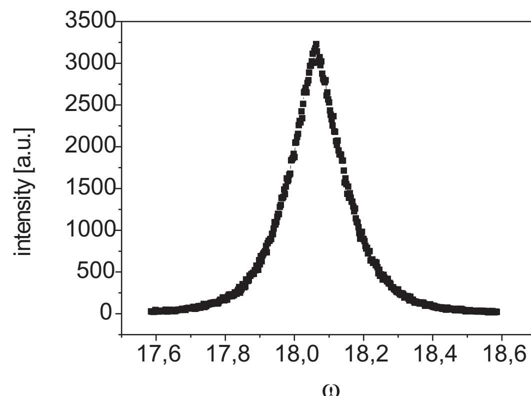

Fig. 4: Rocking curve (0002-reflex) of 500 nm AlN, grown on sapphire. FWHM is 600 arcsec. Peak position is at 18.06°.

For examination of the spectroscopic quality, low temperature cathodoluminescence (CL)-measurements were performed. In fig. 5, the CL-spectrum of the 500 nm thick AlN-layer is displayed. The near-bandedge transition at 6.017 eV is clearly resolved with a FWHM of 30 meV. The logarithmic insert makes the LO-phonon replica visible, which indicate a high optical quality of the AlN-layer.

3. Conclusion

We presented epitaxial growth of AlGaN and AlN layers with MOVPE. Implementation of a low pressure growth process allows fabrication of layers with good optical and crystalline

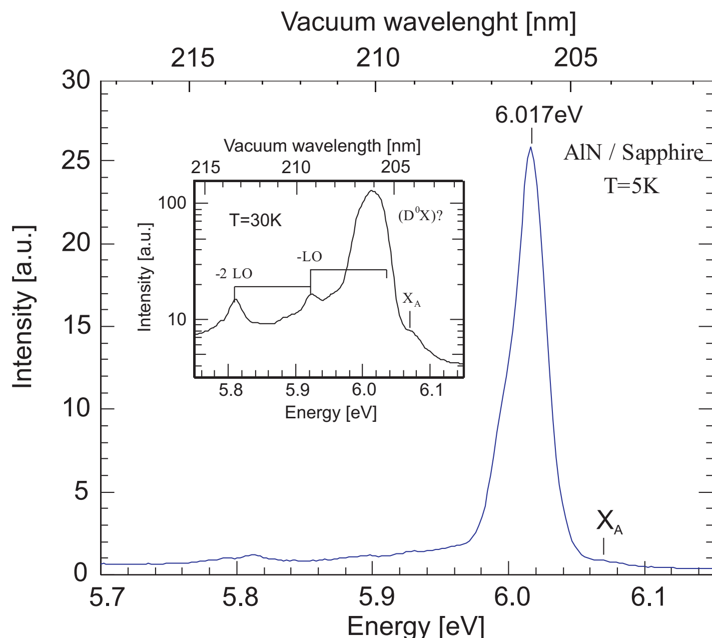

Fig. 5: Low temperature CL-spectra of a 500 nm thick undoped AlN layer, grown on sapphire. The neutral donor bound exciton D^0X and a free exciton (X_A) can be resolved. The insert in logarithmic scale shows the LO-phonon replica, indicating high optical material quality (Measurements performed by G. Prinz, Dept. of Semiconductor Physics, Univ. Ulm).

quality. The prereactions in the gas phase can be sufficiently suppressed but not completely avoided, resulting in reduced growth rates. Our experiments show, that epitaxial growth of AlN and $Al_xGa_{1-x}N$ with high Al-fractions x up to 80 % can be succesfully performed with our MOVPE system.

References

[1] H. Sun, V. Adivarahan, S. Wu, J.P. Zhang, A. Chitnis, M. Shatalov, V. Mandavilli, J.W. Wang and M. Asif Khan, "AlGaN-based 280 nm light-emitting diodes with continuous wave powers in excess of 1.5 mW", *Appl. Phys. Lett.*, vol. 85, p. 531, 2004.

[2] Y. Jung, J. Lee, J. Kim, Y. Lee, M.-B. Lee, J.-H. Lee and S. Hahm "Pt/AlGaN Metal Semiconductor Ultra-Violet Photodiodes on Crack-Free AlGaN Layers" *Jpn. J. Appl. Phys.*, vol. 42, p. 2349, 2003.

[3] Y. Inoue, H. Nagasawa, N. Sone, K. Ishino, A. Ishida, H. Fujiyasu, J.J. Kim, H. Makino, T. Yao, S. Sakakibara and K. Kuwabara, "Fabrication and characterization of short period AlN/GaN quantum cascade laser structures", *J. Crystal Growth*, vol. 265, p. 65, 2004.

[4] N. Nakada, H. Ishikawa, T. Egawa and T. Jimbo, "Suppression of Crack Generation in GaN/AlGaN Distributed Bragg Reflector on Sapphire by the Insertion of GaN/AlGaN Superlattice Grown by Metal-Organic Chemical Vapor Deposition", *Jpn. J. Appl. Phys.*, vol. 42, p. L144, 2003.

Electroluminescence From GaInN Quantum Wells Grown on Non-(0001) Facets of Selectively Grown GaN Stripes

Barbara Neubert and Peter Brückner

Non-(0001) GaInN QWs have been grown by low pressure MOVPE on side facets of triangular shaped selectively grown GaN stripes. By analysing low temperature photoluminescence and room temperature electroluminescence, we found strong indications, that both, In and Mg are less efficiently incorporated on these side facets compared to the common (0001) plane with even lower efficiency for stripes running along $\langle 1\bar{1}00 \rangle$ *compared to* $\langle 11\bar{2}0 \rangle$*. Nevertheless, we observed strong light emission from these quantum wells, supposed to be at least partly caused by the reduced piezo-electric field.*

1. Introduction

The group III nitrides play an important role for light emitting devices, because their spectra reach from UV to visible wavelengths. High brightness LEDs and laser diodes have been fabricated. Due to their strong polarity, group III nitrides show large piezoelectric constants along the ⟨0001⟩ axis. Therefore strong piezoelectric fields (PFs) are induced in biaxially strained GaInN quantum wells (QWs) grown on such ⟨0001⟩-oriented GaN. This gives rise to a spatial separation of the electron and hole wave functions what hampers their radiative recombination. A higher probability for radiative recombination can be expected for QWs grown along directions other than the most commonly used ⟨0001⟩ [1], thus potentially leading to improved optical characteristics for light emitting devices. To this end, some groups have investigated the growth of a-plane structures on r-plane sapphire. However, up to now only lower quality layers with a large dislocation density could be grown [2]. Therefore, we have grown GaInN QWs on non-(0001) facets of selectively deposited GaN stripes with triangular cross-section, where we expect reduced PFs with still low defect densities, in order to evaluate their geometry and facet dependent optoelectronic properties.

2. Experiment

The samples under study have been grown by low pressure metal organic vapor phase epitaxy (MOVPE) in a conventional horizontal reactor. A 1.5 µm thick GaN template was grown first on c-plane sapphire, then was covered with a 200 nm SiO_2 mask by plasma

enhanced chemical vapor deposition (PECVD) and structured by conventional optical lithography and reactive ion etching (RIE) to serve as regrowth mask. We patterned the SiO_2 with two stripe directions perpendicular to each other. The dimensions of the mask openings and mask periods ranged from 4 to 8 µm and from 6 to 300 µm, respectively. We generated silicon doped GaN stripes with triangular shape having $\{11\bar{2}2\}$-facets for $\langle 1\bar{1}00 \rangle$-orientation and $\{1\bar{1}01\}$-facets for $\langle 11\bar{2}0 \rangle$-orientation. Stripes between narrow masks developed a trapeze-like cross-section due to their locally lower growth rate. On these n-doped GaN stripes we have grown a period of 5 nominally 3 nm thick GaInN QWs, containing about 10% In, separated by 10 nm thick GaN barriers followed by a p-doped GaN top layer. For comparison, the same structure was grown without any Si and Mg doping. These samples have been characterized by scanning electron microscopy (SEM), photoluminescence (PL), cathodoluminescence (CL) both at low temeperature and electroluminescence (EL) at room temperature (RT).

3. Results and Discussion

SEM cross-section micrographs showed that the QWs were grown on the side facets of our stripes as well as on the top facet of the trapeze-like stripes. We found that the former were typically 2 to 3 times thinner than the top QWs, obviously due to strong interfacet material migration, first transmission electron microscopy studies confirmed these findings.

The dependence of the PL signal at 20 K on the mask stripe width of the undoped sample is shown in fig. 1. We observed a red shift of the PL maximum for increasing mask width at fixed opening of 6 µm. Similar results have been obtained by CL spectra taken over these different stripes. This shift is probably due to the locally increasing growth rate as a consequence of the increasing mask area [3], further enforced by the more efficient In incorporation with increasing growth rate [4]. Obviously, more In is incorporated into the QWs on the stripes running along the $\langle 11\bar{2}0 \rangle$ direction. For trapeze shaped stripes in $\langle 1\bar{1}00 \rangle$ direction, we find a second maximum of lower intensity at longer wavelengths (fig. 2).

We attribute the short wavelength emission to the GaInN QWs on $\{11\bar{2}2\}$-facets while the weaker emission at longer wavelengths stems from the GaInN (0001) top QWs. Comparable results have been obtained by Nishizuka et. al. [5] by PL microscopy. Due to the large wavelength difference observed in our samples, we think that this shift can only partly be attributed to the different PFs in these QWs, whereas their different thickness mentioned above and changed In incorporation may be also important factors. Even compared to unstructured (0001) reference QWs which emit at 421 nm, the signal of the top QWs is shifted to longer wavelengths confirming increased In incorporation. Probably, interfacet diffusion of In from the side facets to the top facet plays a major role.

For first electroluminescence (EL) experiments we deposited In and Ni/Au test structures on top of the stripes by e-beam evaporation after activation of Mg at 800°C for 10 min in nitrogen ambient. The Ni/Au metallisation was annealed at 400°C for 10 min in nitrogen

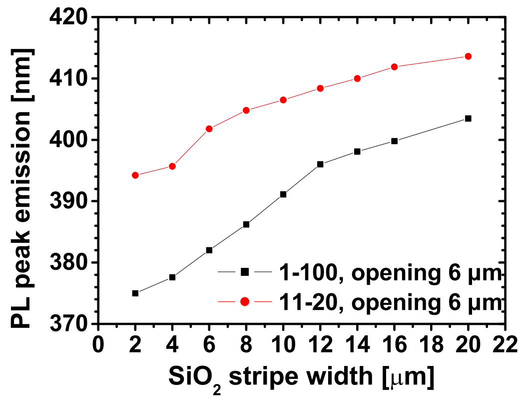

Fig. 1: PL peak positions for stripes along $\langle 1\bar{1}00\rangle$ and $\langle 11\bar{2}0\rangle$.

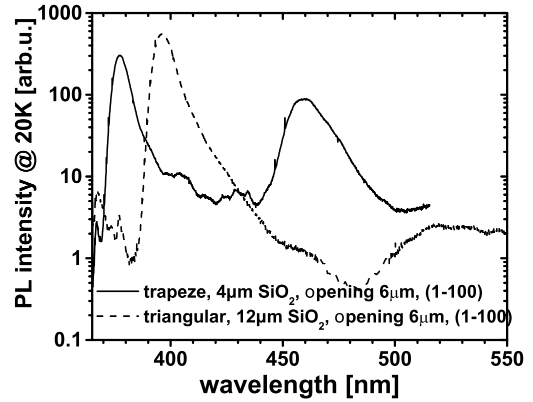

Fig. 2: PL signal for trapeze (solid line) and triangular shaped stripes (interrupted line).

ambient. Due to the large area of our p-type contacts, several stripes were excited simultaneously inhibiting EL studies on single stripes. Even with this simple contact geometry, we measured fairly large light output powers of nearly 1 mW at 20 mA (figure 3). The fairly high resistivities of these structures may be explained by lower Mg incorporation efficiency into the side facets compared to the (0001) layers [6]. Similar as in PL, trapeze stripes in $\langle 1\bar{1}00\rangle$ direction show two maxima (fig. 4). The higher intensity of the longer wavelength peak may support the hypothesis that the Mg incorporation is reduced on the side facets emitting at shorter wavelength. However, strong spectra obtained on pure triangular facets (fig. 4 dotted line) demonstrate that also on these side facets pn junctions have been formed.

4. Conclusion

Our studies show that LED structures can be grown on side facets of selectively grown stripes with triangular cross-section. The observed strong light emission of GaInN QWs on these facets may be partly a consequence of the reduced piezo-electric field in these layers. By analysing different luminescence experiments, we conclude that the In incorporation efficiency depends on the stripe direction and is lower on these side facets as compared to the (0001) plane. We found some indications that the Mg incorporation follows similar trends.

Acknowledgments

We like to thank J. Christen and T. Riemann of Otto-von-Guericke-University in Magdeburg and M. Schirra of University Ulm for CL measurements and M. Beer and J. Zweck

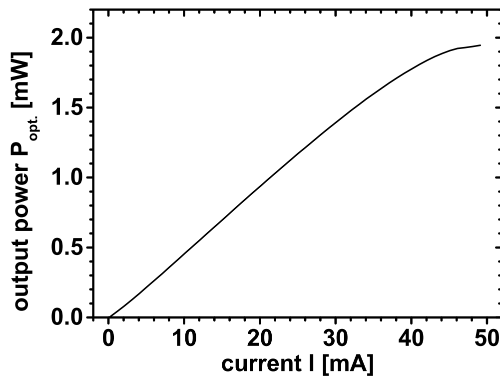

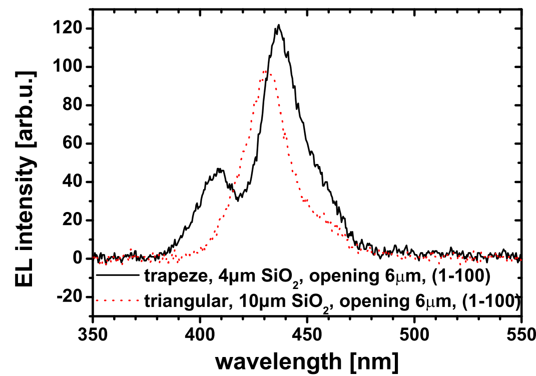

Fig. 3: EL intensity of stripes in $\langle 11\overline{2}0\rangle$ direction.

Fig. 4: EL spectra of trapeze (solid line) and triangular (dotted line) shaped stripes.

of University in Regensburg for TEM measurements.

References

[1] T. Takeuchi, S. Lester, D. Basile, G. Girolami, R. Twist, F. Mertz, M. Wong, R. Schneider, H. Amano, and I. Akasaki, "Polarization control in nitride-based semiconductor," in Proc. *Int. Workshop of Nitride Semiconductors IPAP Conf. I.*, Tokyo, Japan, pp. 137–140, September 2000.

[2] M.D. Craven, S.H. Lim, F. Wu, J.S. Speck, , and S.P. DenBaars, "Structural characterization of nonpolar $(11\overline{2}0)$ a-plane GaN thin films grown on $(1\overline{1}02)$ r-plane," *Appl. Phys. Lett.*, vol. 81, no. 3, pp. 469–471, 2002.

[3] Y.D. Galeuchet, P. Roentgen, and V. Graf, "GaInAs/InP selective area metalorganic vapor phase epitaxy for one-step-grown buried low-dimensional structures," *J. Appl. Phys.*, vol. 68, no. 2, pp. 560–568, 1990.

[4] S. Keller, B.P. Keller, D. Kapolnek, A.C. Abare, H. Masui, L.A. Coldren, U.K. Mishra, and S.P. DenBaars, "Growth and characterization of bulk InGaN films and quantum wells," *Appl. Phys. Lett.*, vol. 68, no. 22, pp. 3147–3149, 1996.

[5] K. Nishizukaand M. Funato, Y. Kawakami, Sg. Fujita, Y. Narukawa, and T. Mukai, "Efficient radiative recombination from $\langle 11\overline{2}2\rangle$-oriented $In_xGa_{1-x}N$ multiple quantum wells fabricated by the regrowth technique," *Appl. Phys. Lett.*, vol. 85, no. 15, pp. 3122–3124, 2004.

[6] T. Akasaka, S. Ando, T. Saitoh, and N. Kobayashi, "Current-confining structure of InGaN hexagonal microfacet lasers by selective incorporation of Mg during selective-area MOVPE," *J. Crystal Growth*, vol. 248, pp. 537–541, 2003.

Observation of Longitudinal Mode Patterns in Violet-Blue GaInN-Based Laser Diodes

Christoph Eichler and Daniel Hofstetter

We report on temperature-independent longitudinal mode patterns in GaInN-based violet diode lasers. The lasers were operated at cw lasing threshold; and the emission spectra were analyzed at a range of temperatures using a high resolution Fourier transform spectrometer. The envelopes of the longitudinal modes showed a characteristic irregular pattern which tuned with temperature at the same rate as the modes themselves. A simulation of the longitudinal modes supports the idea that we see the signature of quantum well thickness fluctuations or indium clusters.

1. Introduction

Optoelectronic devices based on nitride semiconductors have seen a decade of rapid progress which culminated in the successful commercialization of visible light-emitting diodes (LEDs) and violet-blue laser diodes (LDs). Despite of this success, the nitrides are still a material system with many unknown material parameters. This is in particular true for the ternary compound GaInN which plays an important role in state-of-the-art optoelectronic devices [1]. Its considerable lattice mismatch with respect to GaN has obvious consequences like strain or piezo-electric polarization. Other problems arise from the thermodynamic immiscibility of GaN and InN over a wide range of compositions and temperatures [2] leading to problems such as segregation during growth and carrier localization in a nominally two-dimensional electronic system [3]. Especially with respect to the last two points, there has been considerable effort to clarify the role of quantum-dot like carrier confinement for the efficiency of visible light emission.

Using photoluminescence (PL) and various transmission electron microscopy (TEM) approaches, several researchers found strong carrier localization due to In-rich clusters within GaInN quantum wells. The size of the clusters is typically about 3 nm, with an In content reaching values of 60–80% [4, 5, 6]. Although electron beam treatment produces inhomogeneous strain which might result in an over-estimation of the In clustering [7], there appears clear evidence for such a clustering mechanism. On the other hand, thickness fluctuations of the quantum wells can provide significant carrier localization too, supposedly leading to improved efficiency [8].

In this article, we present spectral investigations on GaInN laser diodes which may shed light on this open question from a quite unusual approach. When the lasers are driven

continuously slightly above threshold, they show a specific longitudinal mode pattern, which shifts at the same temperature rate as the longitudinal modes themselves. Although different explanations are possible, we strongly believe that this spectral modulation is the result of carrier localization due to In clustering and/or well thickness fluctuations.

2. Experimental

We investigated a commercial laser diode from Nichia, Inc. grown on sapphire and a device fabricated at OSRAM Opto Semiconductors grown on SiC. The latter device structure is described elsewhere [9]. During the experiment, spectral measurements were carried out at different cw currents and at a range of different temperatures. Special attention was paid to the operating point which remained close to the cw threshold for all temperatures. The output of the laser diode was collimated to a parallel beam and coupled into a Nicolet 870 Fourier transform spectrometer. Measurements were carried out at the maximum resolution of $0.1\,\mathrm{cm}^{-1}$, averaged over 100 single scans, and detected using the internal Si-photodiode.

3. Experimental Results and Discussion

Under these conditions, two sets of longitudinal modes could be resolved which belong to two different lateral mode families (inset of fig. 1). In order to highlight the relevant information, all other spectra contain the maxima of each longitudinal mode only, thus representing the envelope of each spectrum (fig. 2). As seen in fig. 1, currents well below threshold imply a smooth spectral envelope without modulation. Increasing the current leads to an almost linear blue shift of the peak emission wavelength due to band filling while maintaining the smooth shape of the envelope. As the current approaches lasing threshold, the carrier density gets pinned and thus the peak wavelength rests at a nearly constant value. At the same time, the spectral envelope starts to show some modulation features. As shown schematically in fig. 3 (top), we believe that this ripple is due to In composition or well width fluctuations, which again result in a modulation of the quantum well depth. In those well regions with an energetically deep 'hole', carriers get localized, thus leading to a modulation of the carrier density across the well. For low currents, carriers in ALL areas will contribute to spontaneous emission and nonradiative recombination, i.e. the modulation just broadens the emission spectrum. As the current gets closer to lasing threshold, the carrier density in the deep areas of the well becomes sufficiently high to produce gain. Different longitudinal modes then benefit differently from each such gain center, as depicted in fig. 3. At position "1", mode m has a node and thus does not see any amplification at this point within the resonator. But mode $m+1$ has a maximum at position "1", so it benefits fully of the amplification at this point. Likewise, at position "2" mode $m+1$ has a node and sees no amplification, whereas mode m still is amplified. At position "3" finally, both modes see the same amplification. Added up

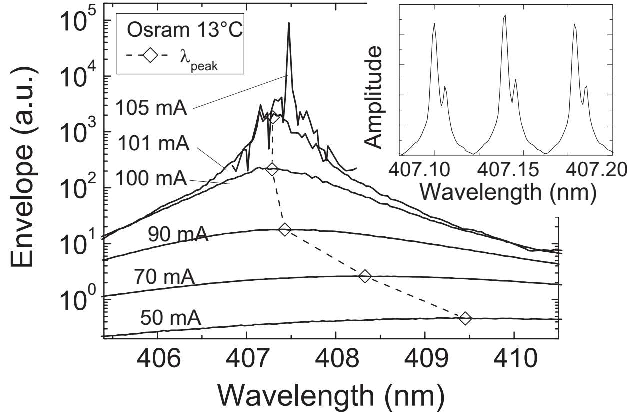

Fig. 1: Envelopes of a series of emission spectra versus current. Below threshold, an almost linear decrease of emission wavelength is observed due to band filling. The inset exemplarily shows three longitudinal modes in full resolution.

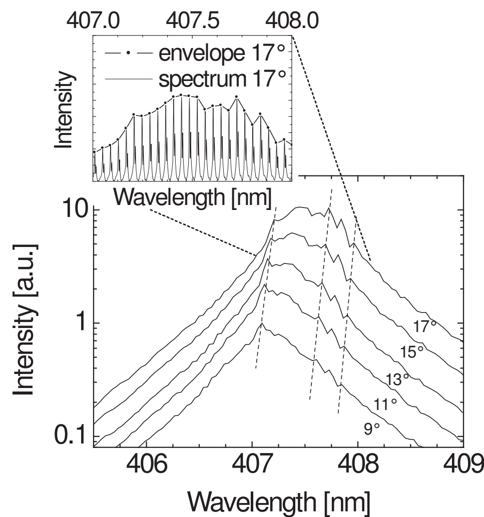

Fig. 2: Diagram on top shows how to obtain the envelope spectra (displayed in the bottom diagram) from the original highly resolved data.

along the ridge, each mode will see its very own amount of amplification, depending on how the gain fluctuations are distributed.

This produces a characteristic envelope of the longitudinal mode pattern, which is a signature of how much additional gain a specific mode experiences when traversing the complicated topography of the spatial gain distribution. According to the analysis presented above, fig. 1 shows the evolution of the spectral modulation versus current for the laser diode on SiC. To separate the pure modulation pattern from the general shape of the spectrum, we smoothed the spectrum using the Fourier transform of its lowest order Fourier component and divided the original spectrum by this smoothed curve. This mathematical procedure yields curves like those shown in fig. 4. They contain the information of how much additional gain or loss a certain longitudinal mode experiences with respect to the average modal gain. fig. 4 (a) shows the modulation of the laser on sapphire for three different currents. As in fig. 1, it is clearly seen that the features of the modulation stay almost constant in shape but get amplified as current increases.

To prove that the observed modulation is a cavity inherent property, we measured spectra

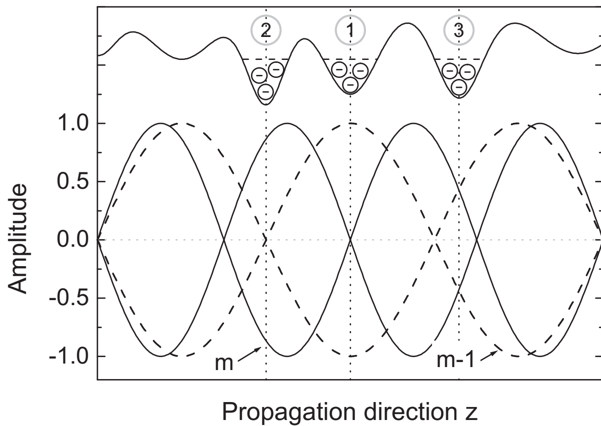

Fig. 3: Schematic representation of the quantum well depth as a function of cavity length. In the lower half, two representative longitudinal modes along with their relative intensity are shown.

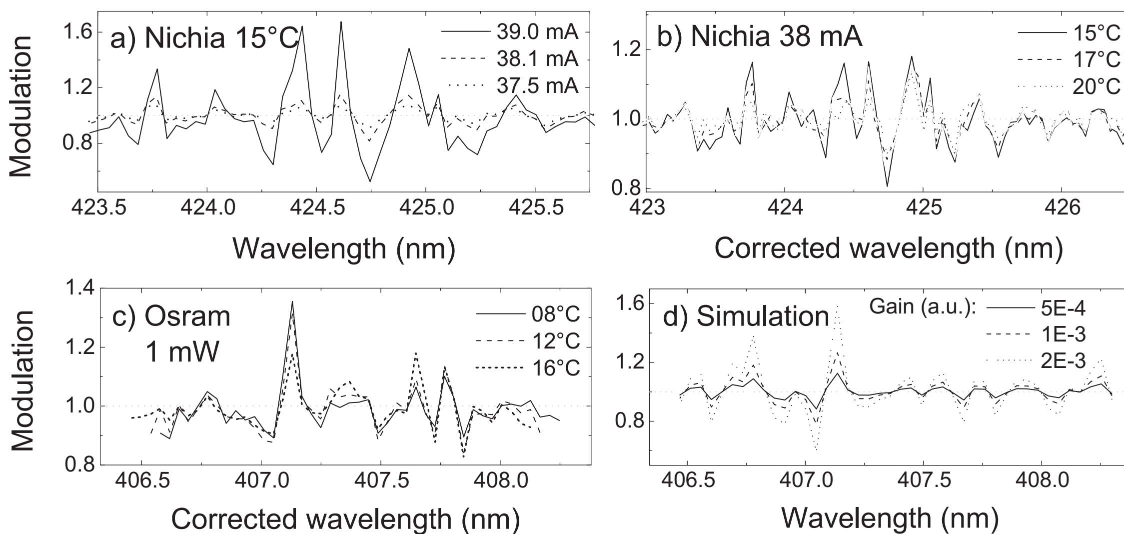

Fig. 4: Spectral envelope: All features are nicely reproduced for different drive conditions: current (a) and temperature (b,c) on sapphire and SiC, respectively; (d) simulated mode patterns.

of the laser diodes at different temperatures, while keeping the current constant for the device on sapphire. When measuring the laser on SiC, we maintained a constant output power of 1 mW. It is obvious that the 'center of mass' of the spectrum shifts with temperature according to the shift of the gain spectrum ($d\lambda_g/dT = 0.04$ nm/K) [10]. Likewise, the comb of longitudinal modes shifts at a much slower rate characteristic for the temperature tuning of the refractive index in nitride semiconductors ($d\lambda_{FP}/dT = 0.015$ nm/K) [10]. In order to visualize the behavior of the modulation pattern without the temperature-related effects of the gain curve, we corrected our data for the influence of the different tuning rates, and extracted the modulation patterns from the spectra as described above. Figs. 4 (b) and (c) show a characteristic pattern which remains nearly unchanged for all investigated temperatures. Since this pattern shifts at the same rate as the longitudinal modes, it is evident that a cavity-inherent property must be at its ori-

gin. As mentioned above, the excess gain/loss experienced by the individual modes and caused by composition/well width fluctuations are very likely responsible for the observed modulation patterns. The described experimental technique thus probes quite sensitively the depth (and therefore the compositional and thickness) fluctuations of the quantum wells.

4. Simulation

Interestingly, the devices on sapphire from Nichia and on SiC from Osram show a very similar behavior. Having a different layer structure and geometry and being grown on substrates with and without defect reducing techniques, we consider the occurrence of the mode patterns in both lasers as a further argument for an GaInN material quality related issue. Although a direct proof is beyond the scope of this article, we present a naive simulation of the experimental findings. Assume that we have a cavity with a length L and a certain number m of point-like gain centers at random positions $0 \leq x_i \leq L$ within the cavity. Assume further that each of these centers introduces a statistically distributed, well-defined amount of gain $g \cdot w_i$, $0 \leq w_i \leq 1$ which is weighted by the individual field intensities $\left|\sin\left\{\frac{2\pi}{\lambda_k}x_i\right\}\right|$. Now we compute how much each longitudinal mode with its respective wavelength λ_k benefits from these gain centers after having travelled through the laser cavity n times:

$$I(\lambda_k) = I_0 \cdot \left[n \prod_{i=0}^{m-1} \left(g w_i \left| \sin\left\{ \frac{2\pi}{\lambda_k} x_i \right\} \right| + 1 \right) \right]^2 \tag{1}$$

The result of this procedure is a mode-specific number which corresponds in first approximation to the relative modal intensity $I(\lambda_k)$. As fig. 4 (d) shows, the obtained mode pattern resembles qualitatively the ones found in the experiments. In this example, we used $m = 60000$, $n = 1$ and varied the gain around $g = 0.001$, but the same qualitative behavior is obtained for entirely different numbers of defects m and roundtrip times n, as long as the gain g is adjusted correspondingly. In agreement with the experiment, increasing the amount of amplification per gain center leads to an exponentially amplified modulation. This corresponds to an increase of current as shown in fig. 4 (a).

5. Conclusion

In conclusion, we see characteristic, temperature-independent longitudinal mode patterns on GaInN laser diodes. Given first that the temperature tuning rates of both these patterns and the Fabry-Perot modes are identical, the former must be due to a cavity-inherent effect. Second, we see that the observed mode patterns are random, i.e. every laser reveals its very own fixed characteristic pattern. Third, we showed that the effect is very sensitive to the amount of gain in the cavity. These three facts together point clearly towards a non-uniform 'depth' of the quantum well due to In clustering or well thickness fluctuations.

References

[1] S. Nagahama, M. Sano, T. Yanamoto, D. Morita, O. Miki, K. Sakamoto, M. Yamamoto, Y. Matsuyama, Y. Kawata, T. Murayama, and T. Mukai, “GaN-based laser diodes emitting from ultraviolet to blue-green,” *Proceedings of SPIE*, vol. 4995, pp. 108–116, 2003.

[2] I.H. Ho and G.B. Stringfellow, “Solid phase immiscibility in GaInN,” *Appl. Phys. Lett.*, vol. 69, no. 18, pp. 2701–2703, 1996.

[3] S. Chichibu, T. Sota, K. Wada, and S. Nakamura, “Exciton localization in InGaN quantum well devices,” *J. Vac. Sci. Technol. B*, vol. 16, no. 4, pp. 2204–2214, 1998.

[4] Y. Narukawa, Y. Kawakami, M. Funato, S. Fujita, S. Fujita, and S. Nakamura, “Role of self-formed InGaN quantum dots for exciton localization in the purple laser diode emitting at 420 nm,” *Appl. Phys. Lett.*, vol. 70, no. 8, pp. 981–983, 1997.

[5] D. Gerthsen, E. Hahn, B. Neubauer, A. Rosenauer, O. Schön, M. Heuken, and A. Rizzi, “Composition Fluctuations in InGaN Analyzed by Transmission Electron Microscopy,” *phys. stat. sol. (a)*, vol. 177, no. 1, pp. 145–155, 2000.

[6] Y.C. Cheng, E.C. Lin, C.M. Wu, C.C. Yang, J.R. Yang, A. Rosenauer, K.J. Ma, S.C. Shi, L.C. Chen, C.C. Pan, and J.I. Chyi, “Nanostructures and carrier localization behaviors of green-luminescence InGaN/GaN quantum-well structures of various silicon-doping conditions,” *Appl. Phys. Lett.*, vol. 84, no. 14, pp. 2506–2508, 2004.

[7] T.M. Smeeton, M.J. Kappers, J.S. Barnard, M.E. Vickers, and C.J. Humphreys, “Electron-beam-induced strain within InGaN quantum wells: False indium ”cluster” detection in the transmission electron microscope,” *Appl. Phys. Lett.*, vol. 83, no. 26, pp. 5419–5421, 2003.

[8] J. Narayan, H. Wang, J. Ye, S.J. Hon, K. Fox, J.C. Chen, H.K. Choi, and J.C.C. Fan, “Effect of thickness variation in high-efficiency InGaN/GaN light-emitting diodes,” *Appl. Phys. Lett.*, vol. 81, no. 5, pp. 841–843, 2002.

[9] U.T. Schwarz, E. Sturm, W. Wegscheider, V. Kümmler, A. Lell, and V. Härle, “Excitonic signature in gain and carrier induced change of refractive index spectra of (In,Al)GaN quantum well lasers,” *Appl. Phys. Lett.*, vol. 85, no. 9, pp. 1475–1477, 2004.

[10] C. Eichler, S.S. Schad, M. Seyboth, F. Habel, M. Scherer, S. Miller, A. Weimar, A. Lell, V. Härle, and D. Hofstetter, “Time resolved study of GaN-based laser diode characteristics during pulsed operation,” *phys. stat. sol. (c)*, vol. 0, no. 7, pp. 2283–2286, 2003.

MBE Growth of GaNAs and AlGaNAs Layers

Fernando Rinaldi and Susanne Menzel

The growth of GaNAs and of the quaternary AlGaNAs alloy by MBE (molecular beam epitaxy) with a nitrogen plasma source is described. Especially for AlGaNAs with very high aluminum content, there is only little information available in the literature. $Al_{0.8}Ga_{0.2}N_{0.03}As_{0.97}$ *layers were successfully grown in our system and characterized in detail using HRXRD (high resolution X-ray diffraction).*

1. Introduction

Dilute nitrides are playing an important role in optoelectronic device engineering, for example in order to produce long wavelength laser diodes. In this work, the growth of AlGaNAs with high aluminum concentration was demonstrated after growing some GaNAs test structures. While the properties of GaNAs and GaInNAs are well documented, just few authors are reporting about AlGaNAs layers [1, 2, 3]. This alloy could be interesting for strain compensation allowing to tune the material band gap by changing the aluminum content as well.

2. Growth Parameters

All samples were grown on GaAs (001) substrate at a growth rate of approximately 900 nm/h, the arsenic BEP (beam equivalent pressure) was about 10^{-5} Torr. The nitrogen was supplied via a HD25R plasma source from Oxford Applied Research working at 13.56 MHz, the coupled power was varied from 100 W to 300 W in order to increase the cracked nitrogen flux. The samples consist of a 200 nm GaAs buffer grown at 580 °C, followed by a 50 nm thick $Al_{1-x}Ga_xN_{1-y}As_y$ and a GaAs cap layer of the same thickness grown at 470 °C. Only in the sample X19, the last two layers have a thickness of 100 nm. GaNAs layers have already sucessfully been grown in our system with a nitrogen content up to 4.6%. Further details regarding our nitrogen source can be found in [4].

3. GaNAs Relaxed Sample

The first sample X19 was grown to calibrate the parameters of the nitrogen source and the growth process. In this sample, 100 nm GaNAs are capped by 100 nm GaAs. During growth, the transition to the 3D growth mode could clearly be observed on the RHEED

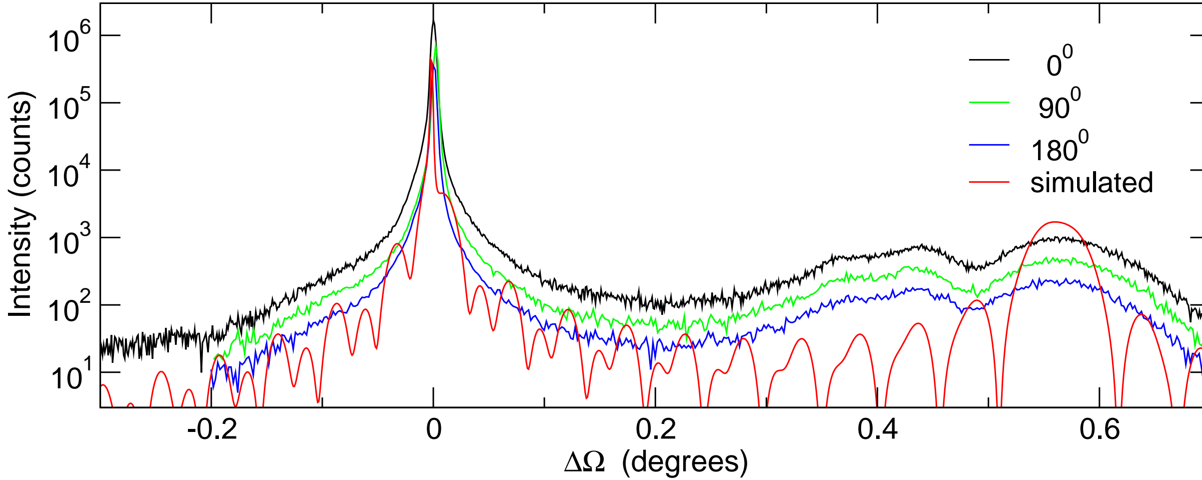

Fig. 1: HRXRD (004) reflection rocking curve on the sample X19: 100 nm GaNAs layer with approximately 4.0% nitrogen and 100 nm GaAs cap layer. The three upper curves were recorded at different azimuth angles and they prove that no tilt is present. A relevant relaxation is observed, since the simulated spectrum exhibits fringes that are not present in the experiment.

screen (reflection high energy electron diffraction) at a layer thickness of about 75 nm. The HRXRD (004) rocking curve in Fig. 1 clearly shows that the layers are not scattering coherently, the simulated curve shows interference fringes that are not present in the measured scans. In Fig. 1 three rocking curves were measured at three different azimuth angles. These curves are identical showing that the GaNAs layer is not tilted. This is an important starting point to analyze the RSM (reciprocal space map) recorded close to the (115) grazing incidence asymmetric reflection shown in Fig. 2. The GaAs cap layer and substrate peak show a complex structure, this is an artefact due to the beam conditioners on the X-ray source side. Two peaks are sligthly shifted to the left due to the partially relaxed GaNAs layer. This is a shift towards higher component of the transferred momentum parallel to the (110) direction. It is always very sophisticated to interprete or even simulate such a RSM, since the relaxation cannot be homogeneous during the growth of the layer. Probably the peak that shows a higher parallel component deviation can be attributed to the more relaxed upper side of the layer after the 3D growth transition. From Fig. 2, the lattice constants parallel and perpendicular to the (001) direction can be extracted easily, and using some basics of elasticity theory [5], a formula for the degree of relaxation can be written as

$$R = \frac{a_{l\parallel} - a_s}{\frac{a_{l\perp} + (2a_{l\parallel} - a_{l\perp})\sigma}{1+\sigma} - a_s} \quad . \tag{1}$$

R is the relaxation coefficient defined between 0 and 1 and σ is the Poisson ratio. The lattice constants a_s, $a_{l\perp}$ and $a_{l\parallel}$ correspond to the substrate and the layers perpendicular and parallel to the growth direction respectively. The value of σ in our case can be

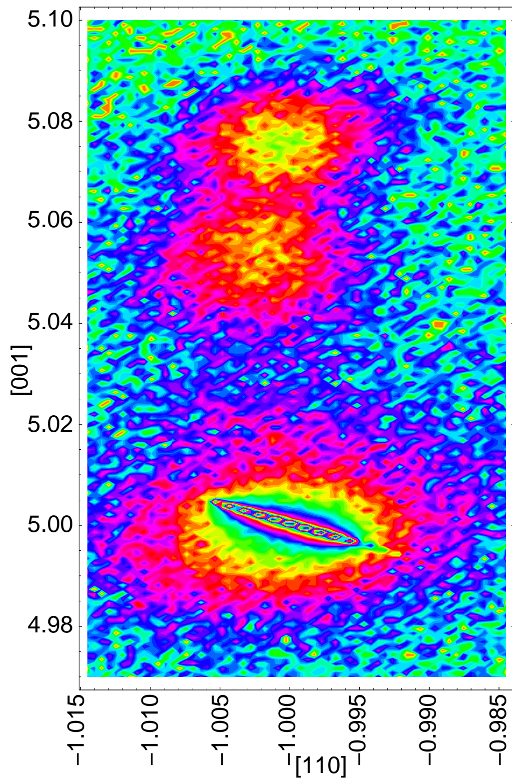

Fig. 2: Reciprocal space map of the sample X19 around the (115) grazing incidence asymmetric reflection. Signs of relaxation are evident in the picture. In fact, the three peaks are not exactly aligned on a vertical line but the minor peaks are shifted to the left showing a different lattice constant parallel to the (001) direction compared to the GaAs one. The very sharp peak at coordinate (−1.0000, 5.000) surrounded by the beam conditioner streak is due to the substrate and the cap layer. The peak situated at (−1.0025, 5.055) can be assigned to the top part of the GaNAs layer, the third peak at (−1.0005, 5.075) corresponds to its bottom part. The lattice constant perpendicular and parallel to the (001) direction can therefore easily be calculated.

calculated from the theory [6] and be expressed as

$$\sigma = \frac{C_{12}}{C_{11} + C_{12}} \simeq 0.311, \tag{2}$$

where we used the values of two components of the stiffness tensor C for GaAs [7, 8]. The formula (2) is consistent with the fact that in many solid bodies or in particular in many semiconductors σ is often very close to 1/3, which allows to simplify (1) into

$$R = \frac{a_{l\parallel} - a_s}{\frac{a_{l\perp} + a_{l\parallel}}{2} - a_s} \quad . \tag{3}$$

In this way, a value of 36% relaxation for the top part of the GaNAs layer can determined, while for the bottom part the calculations results in 6%. Calculating the strain of the layer we obtain -0.80%, corresponding to a nitrogen content of 4.0%.

4. AlGaNAs Samples

The calibration and the characterization of the X19 sample allow to design the layer structures containing pseudomorphic AlGaNAs layers. In Fig. 3, the critical thickness is plotted as a function of the tensile strain according to [9]. The samples X20, X21, X22,

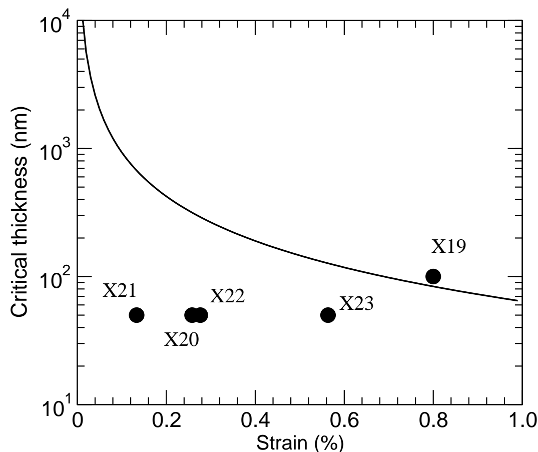

Fig. 3: Critical thickness diagram for a tensilely strained layer. In the calibration sample X19 the critical thickness is exceeded, while in all the others the strained layer is predicted to grow pseudomorphically. Note that X19, has exceeded the critical thickness at approximately 80 nm which is in qualitative agreement with the 3D growth mode transition observed by RHEED.

Fig. 4: Nomarsky contrast micrograph of the sample X19 at 1000 magnification. Due to the relaxation the surface is rough.

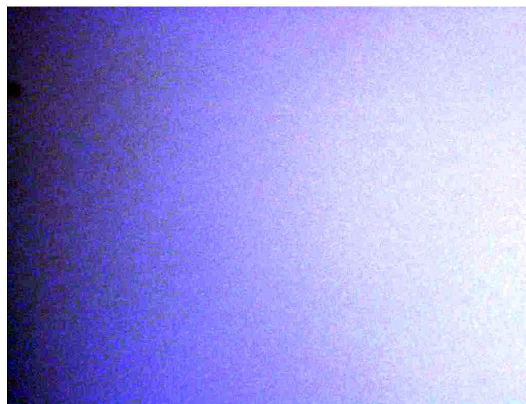

Fig. 5: Nomarsky contrast micrograph of the sample X23 at 1000 magnification, showing a smooth surface.

and X23 are perfectly pseudomorphic and they exhibit no surface roughness in constrast to X19 which is obvious comparing the morphology in Figs. 4 and 5. The rocking curves for the samples X20 to X23 are plotted in Figs. 6 and 7. The corresponding simulations result in the layer compositions shown in Tab. 1. All these rocking curves are well fitted by the simulations and the different layers are scattering coherently. Small disagreements in the simulation are originating from difficulties in predicting the X-ray scattering factor for AlGaNAs.

5. Conclusion

In our MBE system we have grown AlGaNAs layers with nitrogen contents between 1.0% and 4.0% and alumiunm contents between 0% and 80%. No growth problems were encountered when the predicted critical thickness was not exceeded. In the case of the first sample an exhaustive analysis of the relaxation was performed. Two 50 nm $Al_{0.80}Ga_{0.20}N_{0.035}As_{0.965}$ were successfully included in a disk laser structure as strain compensating layers [10].

Sample	Al (%)	Ga (%)	N (%)	As (%)
X20	0	100	1.5	98.5
X21	40	60	1.0	99.0
X22	80	20	1.5	98.5
X23	80	20	3.5	96.5

Tab. 1: Layer compositions of the samples.

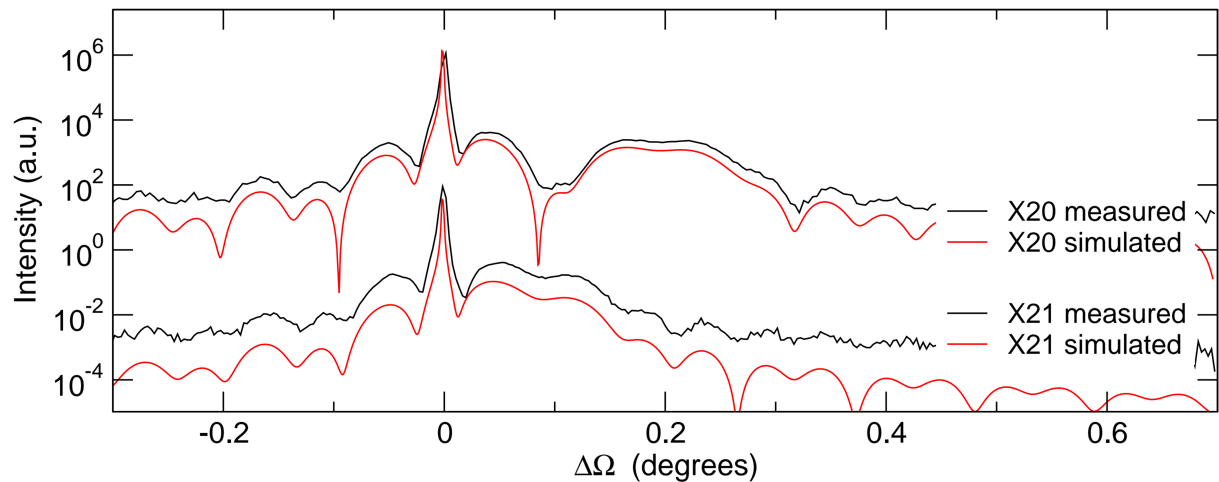

Fig. 6: HRXRD rocking curves of the samples X20 and X21 at the (004) reflection.

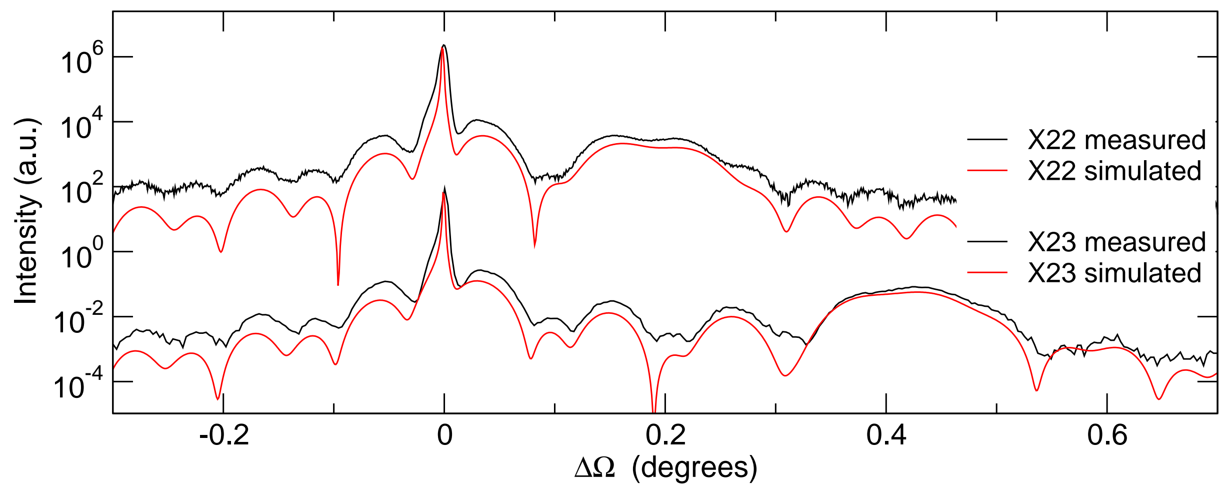

Fig. 7: HRXRD rocking curves of the samples X22 and X23 at the (004) reflection.

References

[1] T. Geppert, J. Wagner, K. Köhler, P. Ganser, and M. Maier, "Preferential formation of Al-N bonds in low N-content AlGaNAs," *Appl. Phys. Lett.*, vol. 80, no. 12, pp. 2081–2083, 2002.

[2] W. Shan, K.M. Yu, W. Walukiewicz, J.W. Ager III, E.E. Haller, and M.C. Ridgway, "Reduction of band-gap energy in GaNAs and AlGaNAs synthesized by N^+ implantation," *Appl. Phys. Lett.*, vol. 75, no. 10, pp. 1410–1412, 1999.

[3] W. Shan, W. Walukiewicz, K.M. Yu, J.W. Ager III, E.E. Haller, J.F. Geisz, D.J. Friedman, J.M. Olson, S.R. Kurtz and C. Nauka, "Effect of nitrogen on the electronic band structure of group III-N-V alloys," *Phys. Rev. B*, vol. 62, no. 7, pp. 4211–4214, 2000.

[4] I. Ecker, *Molekularstrahlepitaxie GaAs-basiender Mischungshalbleiter für 1300 nm-nahe Laserdiodenemission*. PhD thesis, University of Ulm, Ulm, Germany, October 2003.

[5] L.D. Landau and E.M. Lifshitz, *Theory of elasticity*. Oxford: Pergamon Press, 3. ed., 1986.

[6] P.F. Fewster, *X-ray scattering from semiconductors*. London: Imperial College Press, 2000.

[7] S. Adachi, "GaAs, AlAs, and $Al_xGa_{1-x}As$: Material parameters for use in research and device applications," *J. Appl. Phys.*, vol. 58, no. 3, pp. R1–R29, 1985.

[8] T.B. Bateman, H.J. McSkimin, and J.M. Whelan, "Elastic Moduli of Single-Crystal Gallium Arsenide," *J. Appl. Phys.*, vol. 30, no. 4, pp. 544–545, 1959.

[9] J.W. Matthews and A.E. Blakeslee, "Defects in epitaxial multilayers," *J. Crystal Growth*, vol. 27, pp. 118–125, 1974.

[10] M.C. Riedl and F. Rinaldi, "Strain compensated disk lasers structures," *Annual report 2004, Dept. of Optoelectronics, University of Ulm.*

Strain Compensated Disk Lasers Structures

Michael C. Riedl and Fernando Rinaldi

We describe the concept of strain compensated disk lasers. The incorporation of phosphorus and nitrogen was examined to achieve zero accumulated strain in the pump light absorbing and gain providing layers of our structures. X-ray diffraction measurements confirm a successful incorporation, but optimization is still in progress.

1. Introduction

High-power edge-emitting lasers are usually designed with a single quantum well in the epitaxial layer structure. In datacom applications, edge emitting lasers or VCSELs use up to 3 quantum wells. Semiconductor disk lasers employ at least 6 quantum wells in order to provide sufficient gain and their active area is significantly larger. Todays lasers largely utilize compressively strained quantum wells which exhibit an improved optical gain due to splitting of the hole states. With the large number of these strained quantum wells in a semiconductor disk laser, the accumulated compressive strain in the epilayers leads to dislocation lines that cause nonradiative recombination. During operation, additional dislocation lines are created leading to device degradation. Therefore, scaling of the active area to increase the output power is limited by the defect free area on the wafer and strain compensation becomes a relevant issue.

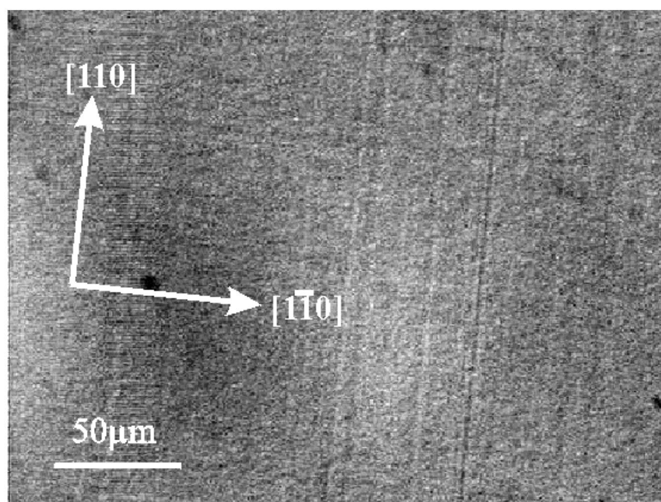

Fig. 1: Cross-hatch lines on an uncompensated disc laser.

2. Design and Growth

As the phosphorus content is crucial for a well defined strain compensation, a test sample featuring 20 repetitions of an InGaAs quantum well compensated by two GaAsP layers was grown to calibrate the phosphorus content with high precision. To balance the strain in a symmetric way, a phosphorus containing layer was placed on each side of each GaAs enclosed quantum well resulting in the perfectly symmetric layer structure as shown in Tab. 2.

	t nm	Composition	$\frac{\Delta d}{d_\perp}$ %
1x	10.0	GaAs	
20x	6.1	$GaAs_{0.82}P_{0.18}$	−1.222
	65.0	GaAs	
	8.0	$In_{0.17}Ga_{0.83}As$	+2.277
	65.0	GaAs	
	6.1	$GaAs_{0.82}P_{0.18}$	−1.222
1x	10.0	GaAs	

Tab. 2: Test structure with phosphorous compensation, quantum well strain under-compensated by 18 %.

	t nm	Composition	$\frac{\Delta d}{d_\perp}$ %
1x	8.0	GaAs	
	228.0	$Al_{0.30}Ga_{0.70}As$	*+0.080*
6x	69.0	GaAs	
	8.6	$In_{0.15}Ga_{0.85}As$	+2.068
	69.0	GaAs	
33x	70.0	$Al_{0.20}Ga_{0.80}As$	*+0.053*
	82.0	AlAs	*+0.271*
1x	8.0	GaAs	

Tab. 3: Standard disk laser without any strain compensation.

	t nm	Composition	$\frac{\Delta d}{d_\perp}$ %
1x	8.0	GaAs	
	211.0	$Al_{0.30}Ga_{0.70}As$	*+0.080*
6x	6.2	$GaAs_{0.81}P_{0.19}$	−1.290
	61.0	GaAs	
	7.5	$In_{0.15}Ga_{0.85}As$	+2.068
	61.0	GaAs	
	6.2	$GaAs_{0.81}P_{0.19}$	−1.290
33x	67.6	$Al_{0.20}Ga_{0.80}As$	*+0.053*
	78.5	AlAs	*+0.271*
1x	8.0	GaAs	

Tab. 4: Disc laser with phosphorus compensation, quantum well strain over-compensated by 3 %.

	t nm	Composition	$\frac{\Delta d}{d_\perp}$ %
1x	8.0	GaAs	
	165.0	$Al_{0.30}Ga_{0.70}As$	*+0.080*
	50.0	$GaN_{0.03}As_{0.97}$	−1.145
6x	72.5	GaAs	
	8.2	$In_{0.15}Ga_{0.85}As$	+2.068
	72.5	GaAs	
1x	50.0	$GaN_{0.03}As_{0.97}$	−1.145
33x	68.0	$Al_{0.20}Ga_{0.80}As$	*+0.053*
	52.2	AlAs	*+0.271*
1x	8.0	GaAs	

Tab. 5: Disc laser with nitrogen compensation, quantum well strain over-compensated by 13 %.

With this calibration and starting from the standard disk laser design as shown in Tab. 3, we were able to grow a phosphorus strain compensated disk laser structure according to Tab. 4. General considerations for the design of semiconductor disk lasers have been discussed in [1, 2] already, including the special non-uniform bragg mirror design also used in the laser samples discussed here.

Also a nitrogen strain compensated disk laser was grown but due to technical limitations with a different design as shown in Tab. 5. This design avoids the alternating sequence of quantum well and nitrogen containing layer and instead places two strain compensating layers surrounding the complete package of quantum wells.

As can be seen from the layer structures, the Al containing layers in the bragg mirrors also add some strain to the layer structure. In this work we focus on compensating the active layers. The small strain of the Al containing layers is therefore printed in italics and not considered in our calculations.

3. Strain Compensation

There are different ways to achieve strain compensation. We consider a system of epitaxial layers with each layer having a defined lattice parameter. This yields the definition of strain

$$\epsilon_i = \frac{a_i - a_\mathrm{s}}{a_\mathrm{s}} = \frac{1+\sigma}{1-\sigma} \cdot \frac{\Delta d}{d_\perp} \tag{1}$$

where a_i and a_s are the bulk lattice constants of the ith layer and the substrate material respectively. Using the Poisson ratio σ, the strain can be derived from X-ray measured variation of the distance of the crystal planes $\frac{\Delta d}{d_\perp}$ in the case of pseudomorphic growth. The value of σ in our case can be calculated from therory [3] and be expressed as

$$\sigma = \frac{C_{12}}{C_{11} + C_{12}} \approx 0.311 \tag{2}$$

where we used the values of two components of the stiffness tensor C for GaAs [4, 5]. For many solid bodies, in particular for semiconductors σ is often very close to $\frac{1}{3}$.

During pseudomorphic epitaxial growth, each layer is forced by internal stress to accomodate the lattice constant parallel to the growth surface to the value of the substrate material. Therefore a stress field results in the material. The theory for a complete understanding [6] is extremely difficult already for our case, so much easier approaches are often suggested. For example from [7, 8] the notion of effective strain is used to have a stability criteria for the growth of the nth layer

$$\epsilon_\mathrm{eff} = \frac{\sum_{i=1}^{n} \epsilon_i t_i}{\sum_{i=1}^{n} t_i} \tag{3}$$

where the sum is carried from the first strained layer grown to the nth layer. A plot of ϵ_eff for a compensated and an uncompensated layer structure is shown in Fig. 2.

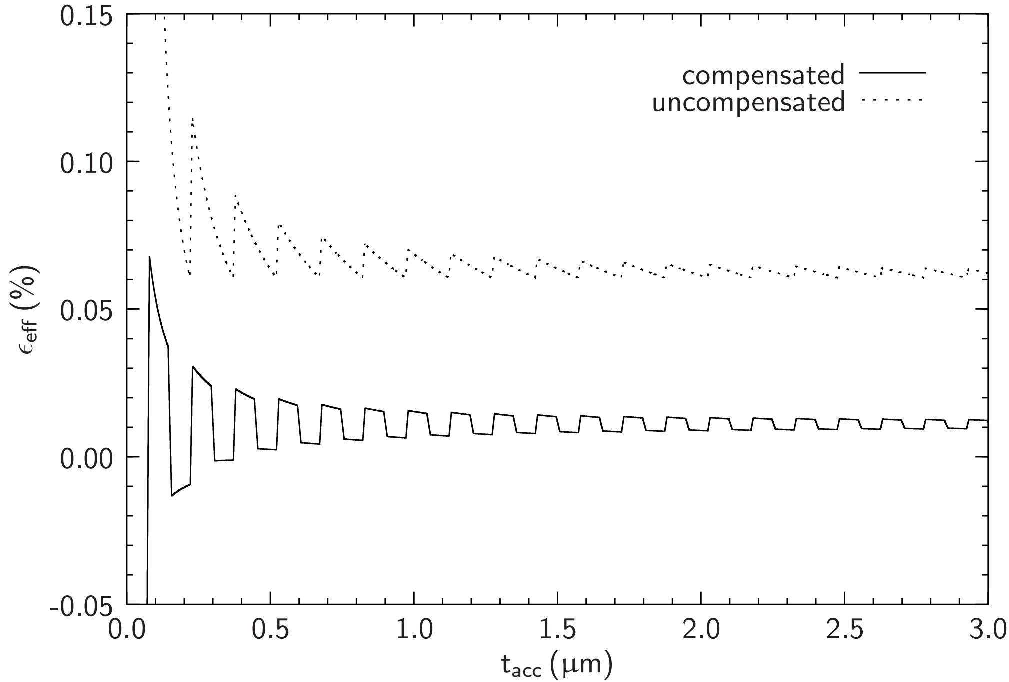

Fig. 2: Effective strain for a compensated structure according to Tab. 2 and an equivalent structure without any strain compensating layers. The accumulated thickness $t_{\text{acc}} = 0$ when growth of the first strained layer starts and increases in growth direction. Therefore for the compensated structure $\epsilon_{\text{eff}}(0) = -0.611\,\%$ and for the uncompensated one $\epsilon_{\text{eff}}(0) = +1.139\,\%$.

In our work we designed our layer structures so that the positive strain from the quantum wells cancels out with the negative strain from the compensation layers

$$\sum_{\text{qw}} \epsilon_i t_i + \sum_{\text{comp}} \epsilon_i t_i \; = \; 0 \tag{4}$$

which corresponds to 100 % compensation. The percentage of compensation is given for each layer structure.

4. HRXRD Characterization

To have a high precision strain measurement, HRXRD (high resolution X-ray diffraction) measurements were performed on the epitaxially grown samples. We have always chosen the symmetric (004) reflection, as in this condition a sensitivity of less than 10^{-4} is easy to achieve. The substrate peak was always normalized to 0.000°, and the dynamic theory was used for the simulations.

For the calibration test sample in Fig. 3, more than 50 satellite peaks are recorded and from the magnified view in the inset one can see that the 0th order is shifted to −0.010°. This shows that a complete compensation was not reached. The simulation yields a

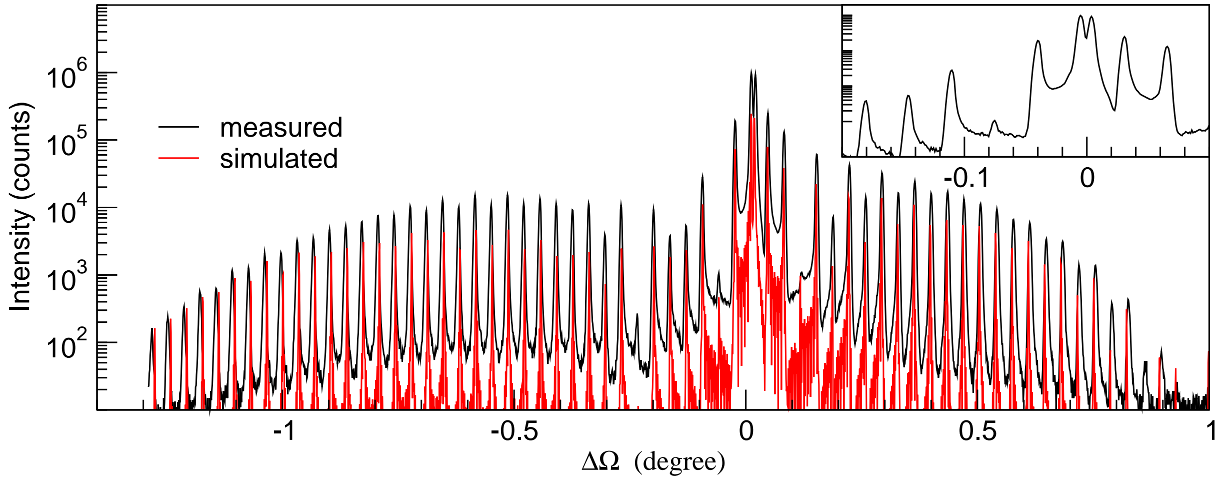

Fig. 3: HRXRD (004) rocking curve of the test structure according to Tab. 2.

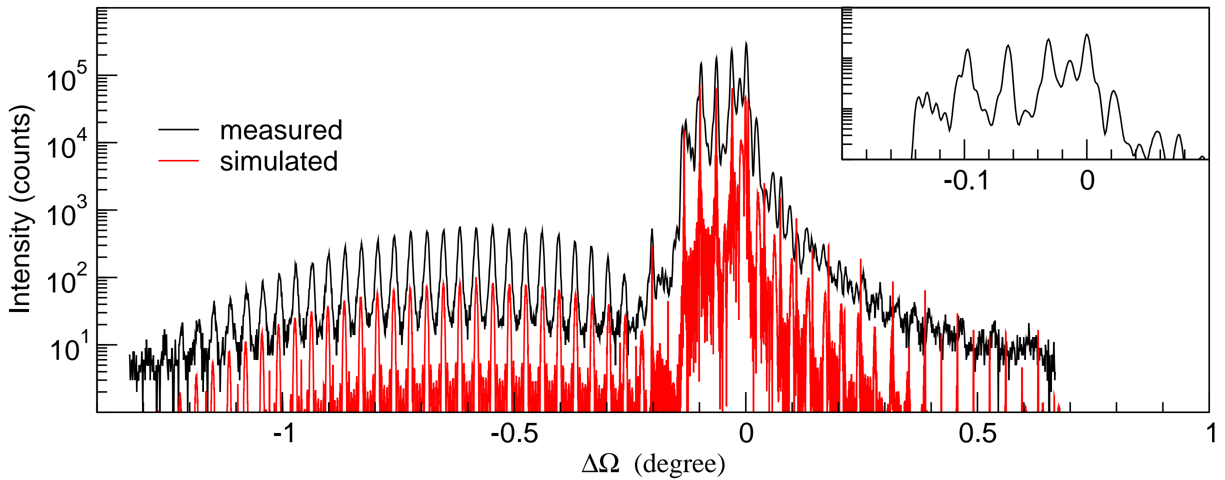

Fig. 4: HRXRD (004) rocking curve of the uncompensated disk laser according to Tab. 3.

perfect agreement with the measured data over the complete range. The separation of the satellites is a characteristic of the period of the structure. The indium containing layer shapes the envelope of the peaks on the lower angle side, the phosphorus containing the ones on the higher angle side referring to the substrate. Using (4) we determine that 12% of the strain remained. Although the strain compensation in the sample was not complete, we were able to grow 20 InGaAs QWs without any sign of relaxation.

The interpretation of a complete device structure is much more complicated. The layer sequence of the 33 pairs is not strictly periodic [1], creating another family of peaks which lead to a consistent braodening of the high order satellite peaks. In our simulation, the bragg mirror stack was considered to be perfectly periodic. This results in a certain disagreement on the large angle sides in Figs. 4 and 5 where many satellites peaks present in the simulation do not match with the measurement. Despite of this problem, the distance between the quantum wells, their composition and their thickness can be derived

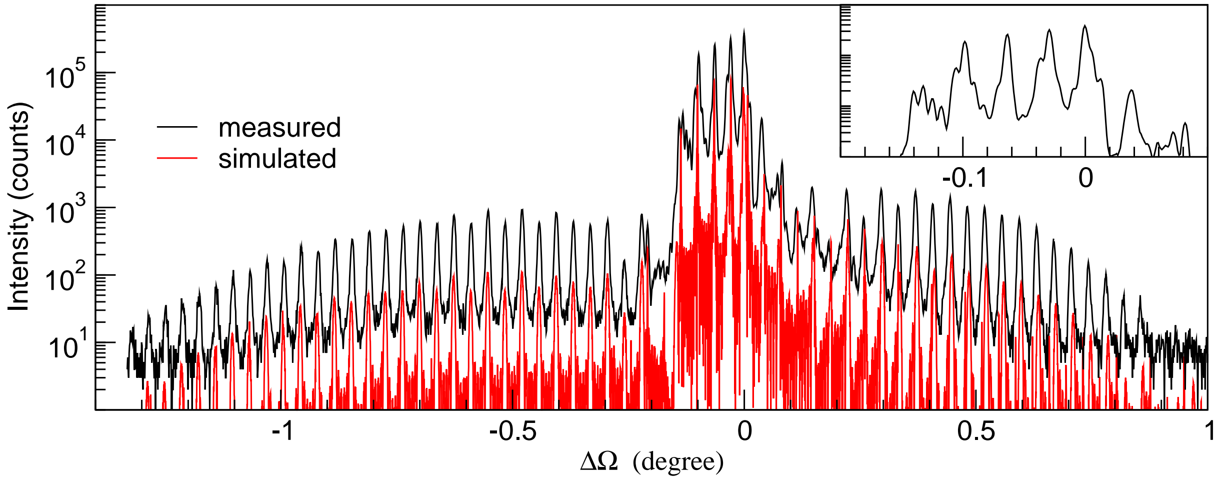

Fig. 5: HRXRD (004) rocking curve of the phosphorus compensated disk laser according to Tab. 4.

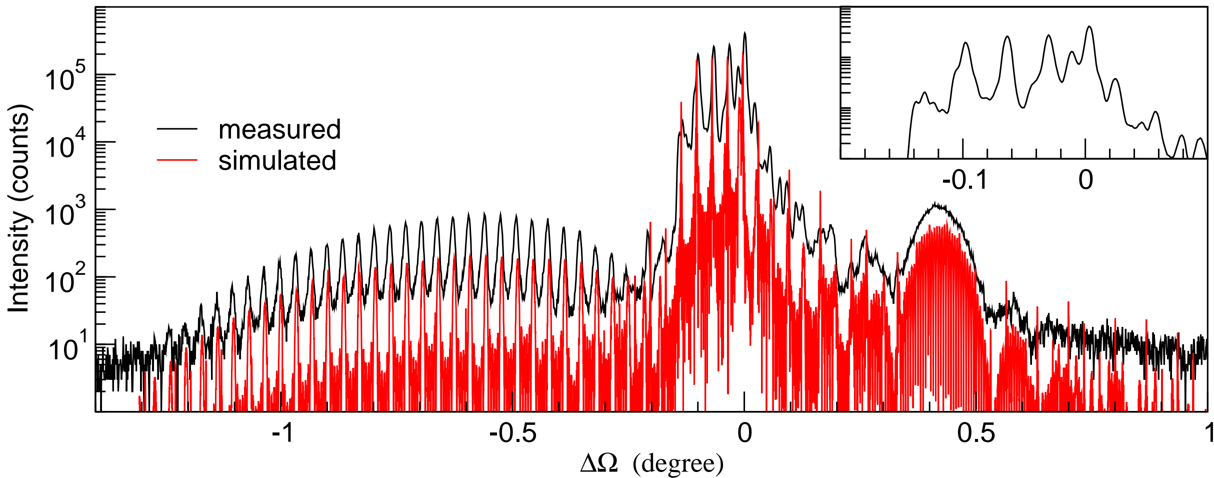

Fig. 6: HRXRD (004) rocking curve of the nitrogen compensated disk laser according to Tab. 5.

with high precision. In particular, from the two insets, it is again possible to distinguish the 0th order satellite of the 6 fold repeated quantum well region at approximately $-0.015°$ for the uncompensated structure, while for the phosphorus compensated one, the 0th relative satellite is merged to the substrate peak. For this device, the simulation shows that the strain was over-compensated by 3%.

As already described, the nitrogen containing sample is strain compensated using two AlGaNAs 50 nm thick layers around the periodic quantum well region. For this reason the compensating layers are not involved in the satellite pattern, and they are responsible for the typical broad peak in Fig. 6 situated at approximately $+0.450°$, again here the simulation allows to calculate that the InGaAs quantum well strain was over-compensated by 13%.

5. Conclusion and Outlook

We have sucessfully fabricated layer structures that are strain compensated up to an accuracy of 3% as measured by X-ray characterization. The uncompensated as well as the phosphorus compensated disk lasers operated in cw mode.

The nitrogen compensated disk lasers show only pulsed operation which is attributed to the technical limitations in the epitaxial growth, but these are overcome meanwhile. Therefore also the incorporation of nitrogen into the quantum wells might be an interesting approach.

It has not been shown yet that these layer structures can tolerate mechanical strain during mounting better than uncompensated ones. Also potential improvements in lifetime have not been proven up to now.

References

[1] F. Rinaldi, "Epitaxy and Structural Characterization of 980 nm Semiconductor Disk Lasers," *Annual Report 2003, Optoelectronics Department, University of Ulm*, pp. 29–34.

[2] E. Schiehlen and M.C. Riedl, "Diode-pumped Intra-cavity Frequency Doubled Semiconductor Disk Laser with Improved Output Beam Properties," *Annual Report 2002, Optoelectronics Department, University of Ulm*, pp. 63–68.

[3] P.F. Fewster, *X-ray scattering from semiconductors*. London: Imperial College Press, 2. ed., Aug 2003.

[4] S. Adachi, "GaAs, AlAs and $Al_xGa_{1-x}As$: Material parameters for use in research and device applications," *Appl. Phys. Lett.*, vol. 58, no. 3, pp. R1–R29, 1985.

[5] T.B. Bateman, H.J. McSkimin, and H.M. Whelan, "Elastic Moduli of Single-Crystal Gallium Arsenide," *J. Appl. Phys.*, vol. 30, no. 4, pp. 544–545, 1959.

[6] L.D. Landau and E.M. Lifshitz, *Theory of Elasticity*, vol. 7. Oxford: Pergamon Press, 3. ed., Dec 1986.

[7] D.C. Hougthon, M. Davies, and M. Dion, "Design criteria for structurally stable, highly strained multiple quantum well devices," *Appl. Phys. Lett.*, vol. 64, no. 4, pp. 505–507, 1994.

[8] G.A. Vawter and D.R. Myers, "Useful design relationships for the engineering of thermodynamically stable strained-layer structures," *J. Appl. Phys.*, vol. 12, no. 65, pp. 4769–4773, 1989.

[9] F. Rinaldi and S. Menzel, "MBE growth of GaNAs and AlGaNAs layers," *Annual Report 2004, Optoelectronics Department, University of Ulm*, pp. 65–70.

Semiconductor Disk Laser on Microchannel Cooler

Eckart Gerster

An optically pumped semiconductor disk laser with a double-band Bragg reflector mirror is presented. This mirror not only reflects the laser light at a wavelength of 980 nm but also the pump light at 808 nm. An inverted epitaxial layer sequence allows the complete removal of the GaAs substrate after the semiconductor laser disk has been mounted onto a water-cooled microchannel heat sink. Since the semiconductor disk has a thickness of around 7 µm, the optically pumped active area is much larger than the disk thickness resulting in a one-dimensional homogeneous heat flow through the semiconductor disk. In this case, the semiconductor disk laser can be scaled towards higher power levels. In first experiments, a continuous single-mode optical output power of 3.6 W has been achieved which was limited by the output power of the broad-area pump laser diode.

1. Introduction

Semiconductor lasers are gaining increasing interest because of their small size, a high electrical-to-optical power conversion efficiency, the excellent reliability of the devices, and the electronic modulation properties up to frequencies of several GHz. When properly designed, laser diodes exhibit single-mode beam properties at low output powers. At high output powers however, the beam properties are degraded due to filamentation effects. Additionally, the power is limited by device heating and Catastrophic Optical Mirror Damage (COMD) [1]. The optically pumped semiconductor disk laser is a novel approach which allows high optical output powers of semiconductor lasers while maintaining an excellent beam quality [2]. This type of laser unifies the benefits of solid-state thin-disk lasers [3] and Vertical-Cavity Surface-Emitting Lasers (VCSELs) [4]. The setup of a semiconductor disk laser is schematically illustrated in Fig. 1. The undoped epitaxial structure consists of a Bragg mirror and a resonant gain region which is optically pumped by a broad-area laser diode. The second mirror is an external concave dielectric mirror resulting in a stable concentric resonator configuration enforcing single-mode operation. Due to the external mirror, additional elements can be positioned inside the laser cavity like nonlinear crystals to achieve frequency doubling [5, 6]. The concept of this type of laser is scalable in output power [7, 8] if the heat extraction from the laser disk is homogeneous.

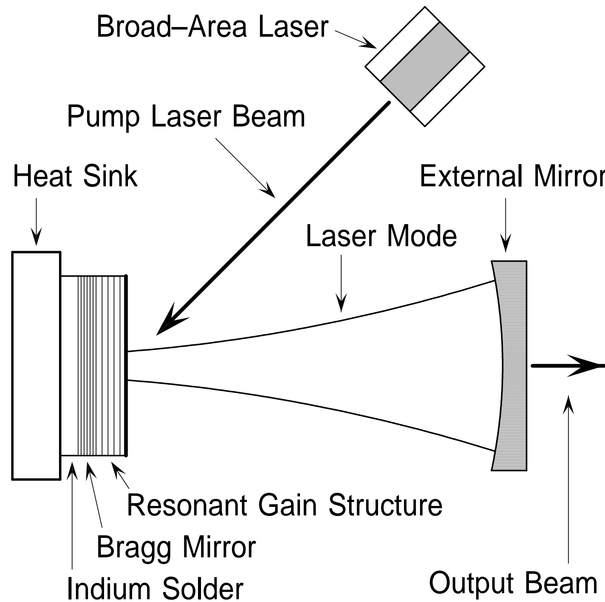

Fig. 1: Schematic drawing of the setup of an optically pumped semiconductor disk laser. The semiconductor disk consists of an epitaxially grown Distributed Bragg Reflector (DBR) and a resonant quantum-well gain structure. Together with an external concave mirror, a fundamental transversal mode develops in the laser resonator. The laser disk is optically pumped by a focused beam from a high-power broad-area edge-emitting laser diode.

2. Epitaxy

The epitaxial structure of the semiconductor disk lasers is grown by solid-source molecular-beam epitaxy on a GaAs substrate. An etch-stop layer is the first layer which is grown onto the substrate, followed by a window layer, six InGaAs quantum wells embedded in GaAs absorbing layers, and completed by AlGaAs/AlAs Bragg mirror layers. The AlAs etch-stop layer allows the complete removal of the substrate in a wet-chemical etching process. After substrate removal, the etch-stop layer is also removed in an additional etching step. The AlGaAs window layer prevents excited carriers from recombining at the wafer surface and is transparent for the pump wavelength. The gain is provided by six compressively strained InGaAs quantum wells in the antinodes of the standing-wave pattern of the laser light separated by GaAs absorbing layers. Electron–hole pairs are generated by the absorption of the pump light in the GaAs absorbing layers and relax into the InGaAs quantum wells where they undergo stimulated emission. The very strong absorption coefficient of the GaAs material yields to short absorption lengths for the pump light of only a few microns. A standing wave builds up within the resonator with the intensity maxima located in the quantum-well regions. The monolithically grown Bragg mirror consists of AlGaAs/AlAs layers. An aluminum content of 20 % in the AlGaAs mirror layers was chosen to to avoid absorption of the pump wavelength in the mirror layers. The double-band Bragg mirror is designed to reflect the laser wavelength of 980 nm at normal incidence and additionally the 808 nm pump beam under an angle of

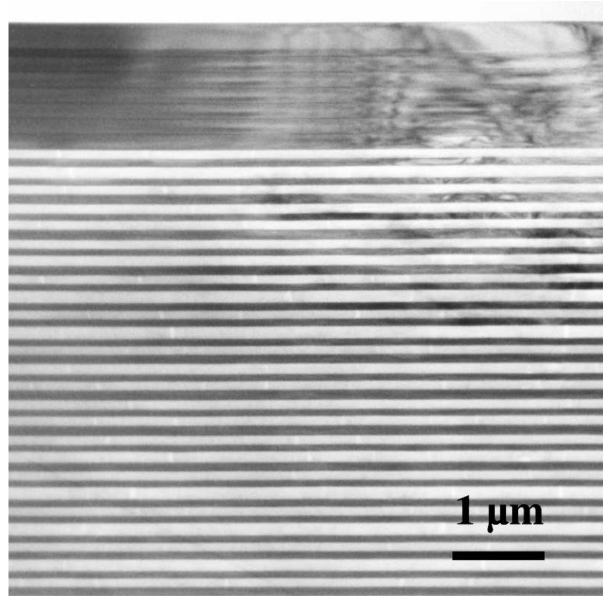

Fig. 2: The transmission electron micrograph shows a disk-laser structure having six quantum wells in the upper part of the image and a portion of the double-band Bragg mirror layer sequence.

45° back into the absorbing layers to enhance the absorption rate. Thus, heat generation in the Bragg mirror is almost avoided. A transmission electron micrograph (TEM) of the epitaxial layer sequence is show in Fig. 2.

3. Mounting

A semiconductor disk laser can be scaled to achieve higher output powers. This scaling is performed by increasing the pump power and the pumped area on the semiconductor disk by the same factor. In this case, the pump power density and the temperature of the

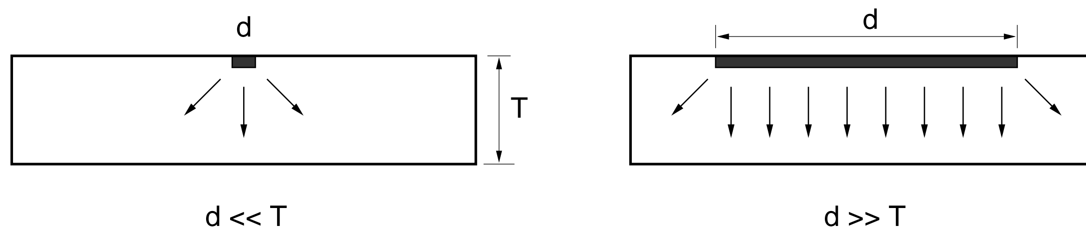

Fig. 3: Heat flow in a semiconductor disk laser. If the optically pumped active area size on the disk d is small compared to the disk thickness T as shown at the left-hand side of the illustration, the heat flow is three-dimensional. On the right-hand side, a nearly one-dimensional homogeneous heat flow for an active area size d which is much larger than the disk thickness T is depicted.

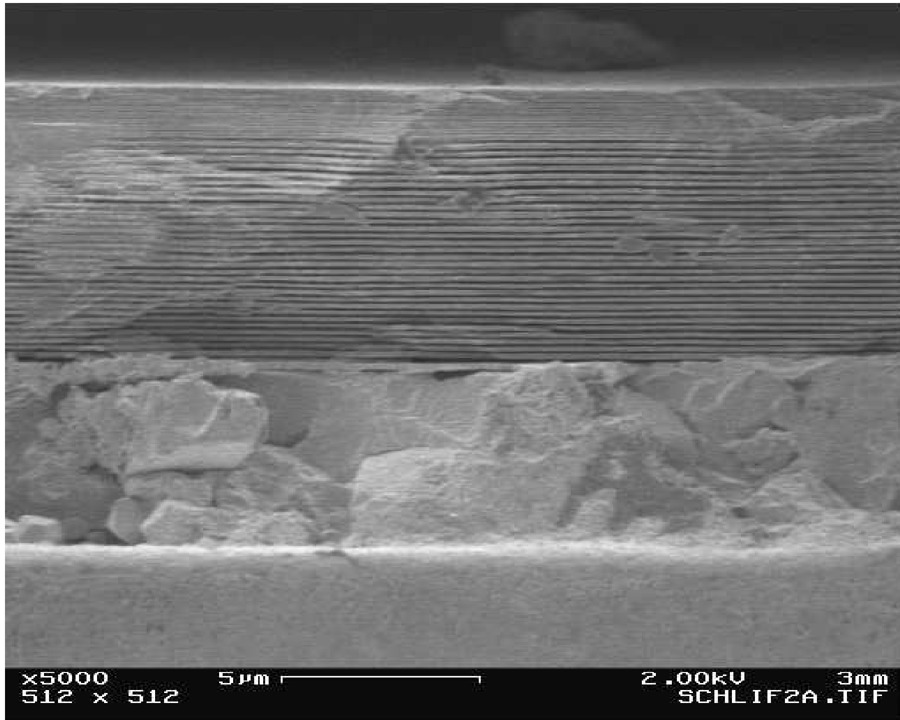

Fig. 4: Scanning electron micrograph showing a cross section of the disk laser after substrate removal and soldering onto the heat sink. The semiconductor disk laser has a thickness of 7.5 µm and the indium solder a thickness of 5 µm.

pumped laser-active area stays constant, which is only true if a top-head pump-light profile is used and the heat extraction from active area through the disk is homogeneous. As illustrated in Fig. 3, homogeneous one-dimensional heat flow can be achieved by making the disk thinner than the active area diameter. After epitaxial growth, the wafer has been soldered onto a water-cooled microchannel heat sink using an indium solder. Then, the substrate has been removed completely by a wet-chemical etching process resulting in a 7.5 µm-thick film of semiconductor material, which only consists of the epitaxial layer sequence. A cross sectional scanning electron micrograph (SEM) of the semiconductor disk, the solder, and the heat-sink surface is shown in Fig. 4. The photographic pictures in Fig. 5 show the microchannel-cooler heat sink with the mounted semiconductor disk-laser chip.

4. Characterization

The mounted semiconductor disk has been assembled into an experimental disk-laser setup. The continuous optical output power characteristics are shown in Fig. 6 for three different reflectivities R of the curved external resonator mirror. For a mirror reflectivity of 98 %, an output power of 3.6 W has been achieved for a pump power slightly below 12 W. This corresponds to a differential efficiency of $\eta_{\text{diff}} = 41\,\%$ and a differential quantum

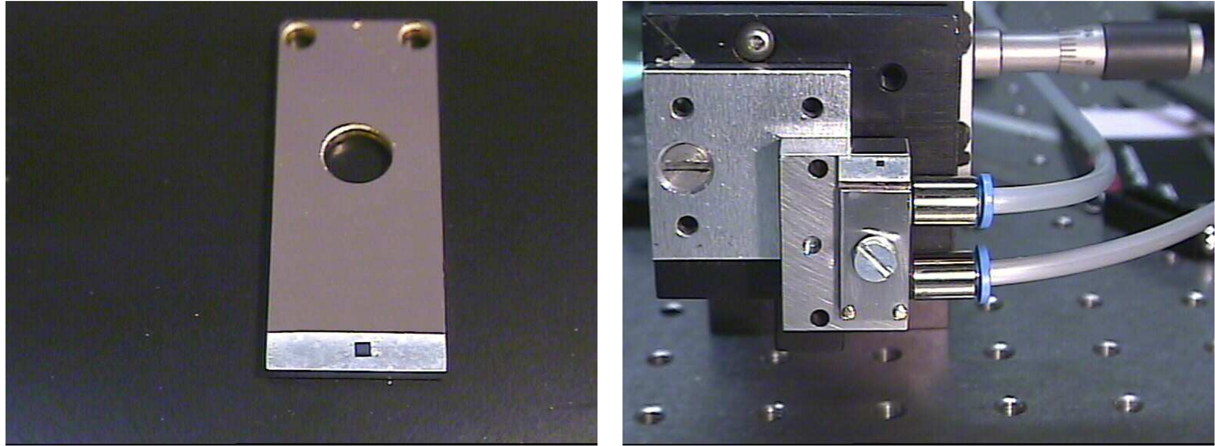

Fig. 5: Semiconductor disk laser mounted on a water-cooled microchannel heat sink. The photograph on the left-hand side shows the heat sink with the small quadratic semiconductor disk-laser chip in the lower edge. In the photograph on the right-hand side, the heat sink is connected to cooling water fittings and assembled in the experimental setup.

efficiency of 50 %. The output power is limited by the pump power which was available for the experiment.

References

[1] A. Moser and E.E. Latta, "Arrhenius parameters for the rate process leading to catastrophic damage of AlGaAs-GaAs laser facets," *J. Appl. Phys.*, vol. 71, no. 10, pp. 4848–4853, 1992.

[2] M. Kuznetsov, F. Hakimi, R. Sprague, and A. Mooradian, "Design and characteristics of high-power (>0.5-W CW) diode-pumped vertical-external-cavity surface-emitting semiconductor lasers with circular TEM_{00} beams," *IEEE J. Selected Topics Quantum Electron.*, vol. 5, no. 3, pp. 561–573, 1999.

[3] A. Giesen, "Results and scaling laws of thin disk lasers," *Proc. SPIE*, vol. 5332, pp. 212–227, 2004.

[4] B. Weigl, M. Grabherr, C. Jung, R. Jäger, G. Reiner, R. Michalzik, D. Sowada, and K.J. Ebeling, "High-performance oxide-confined GaAs VCSEL's," *IEEE J. Selected Topics Quantum Electron.*, vol. 3, no. 2, pp. 409–415, 1997.

[5] E. Schiehlen, M. Golling, and P. Unger, "Diode-pumped semiconductor disk laser with intracavity frequency doubling using lithium triborate (LBO)," *IEEE Photon. Technol. Lett.*, vol. 14, no. 6, pp. 777–779, 2002.

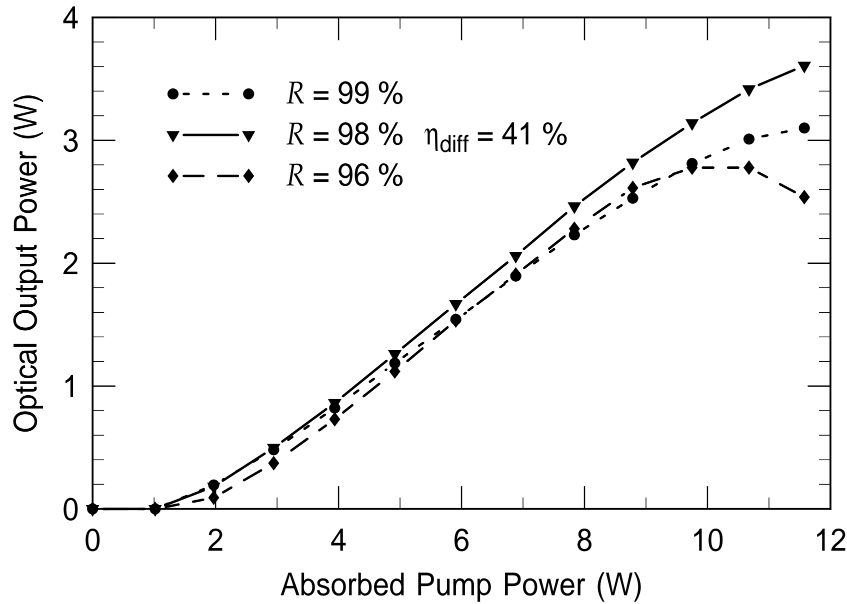

Fig. 6: Continuous output power of the semiconductor disk laser at a wavelength of 980 nm. For an external mirror having a reflectivity of $R = 98\,\%$, an optical output power of 3.6 W is achieved at a pump power of 12 W. The slope of the characteristics, called differential efficiency, has a value of $\eta_{\mathrm{diff}} = 41\,\%$ which corresponds to a differential quantum efficiency of 50 %.

[6] E. Gerster, I. Ecker, S. Lorch, C. Hahn, S. Menzel, and P. Unger, "Orange-emitting frequency-doubled GaAsSb/GaAs semiconductor disk laser,' *J. Appl. Phys.*, vol. 94, no. 12, pp. 7397–7401, 2003.

[7] S. Lutgen, T. Albrecht, P. Brick, W. Reill, J. Luft, and W. Späth, "8-W high-efficiency continuous-wave semiconductor disk laser at 1000 nm," *Appl. Phys. Lett.*, vol. 82, no. 21, pp. 3620–3622, 2003.

[8] J. Chilla, S. Butterworth, A. Zeitschel, J. Charles, A. Caprara, M. Reed, and L. Spinelli, "High power optically pumped semiconductor lasers," *Proc. SPIE*, vol. 5332, pp. 143–150, 2004.

Optimization of Process Parameters for Low-Absorbing Optical Coatings Fabricated by Reactive Ion-Beam Sputter Deposition

Steffen Lorch

The parameters of a reactive ion-beam sputter deposition system have to be optimized to achive layers with low absorption. For that, different materials have been deposited with variing the oxygen partial pressure to find the optimum for each material. Additionally, the position and the angle of the substrate related to the target have been changed to examine the influence on the absorption. The measurements have been performed using photothermal deflection which is a suitable method to determine such small absorption values.

1. Introduction

Optical coatings have a wide range of applications. For lasers, anti-reflection/highreflection coatings are used and laser amplifiers need coatings with reflectivities lower than 10^{-4}, additionally they should have a very low absorption to increase the threshold of the catastrophically optical mirrow damage (COMD). Low absorptions are also necessary for coatings on disk lasers because they are located in the cavity and, due to multi passes of the light, absorbing layers can inhibit lasing. To achieve optical coatings with low absorption, a reactive ion-beam sputter deposition (RIBSD) system is used because of the dense and stoichiometric layers [1, 2, 3, 4]. To optimize the coating parameters of such a system, the absorption of the coated layers has to be measured. For that, the photothermal deflection method [5, 6] has been used to measure such low absorption values.

2. Theory

The sputter process of a RIBSD system is schematically shown in Fig. 1. The argon ions are extracted from an ion-beam source, are neutralized by electrons, and strike the target. The sputtered target material is deposited on the substrate. During the sputter process, a part of the oxygen is lost (1) and the deposited material is understoichiometric, this results in absorbing layers. To avoid this, additional oxygen is introduced into the process chamber to increase the oxide state of the target and so the deposited material is stoichiometric and has a lower absorption. But with increasing the partial pressure of oxygen the absorption increases due to the higher amount of high-energetic oxygen

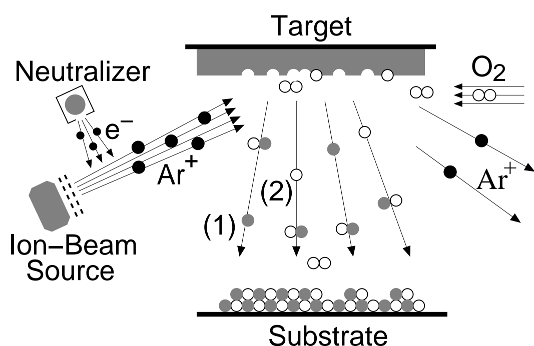

Fig. 1: Schematical drawing of the sputter mechanism. Possible absorption may be caused by insufficient oxygen (1) and damage by high-energetic oxygen (2).

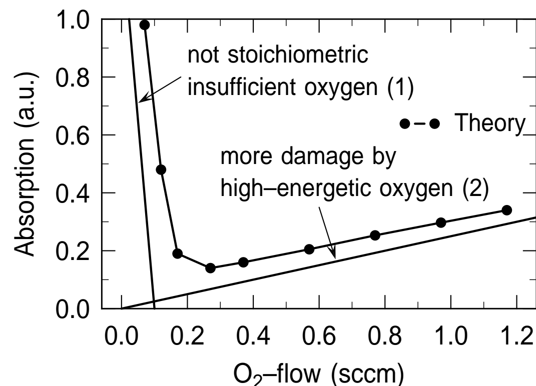

Fig. 2: Theoretical curve for the absorption over the oxygen partial pressure and the limiting effects.

bombardment (2) which brings damage on the deposited material. Thus, the absorption is a superposition of these two mechanisms and at the optimal partial pressure of oxygen, the absorption shows a minimum. This behavior is theoretically depicted in Fig. 2 [2].

3. Measurement Method

The absorption of metal-oxide coatings fabricated with reactive ion-beam sputter deposition has values in the range of $\alpha \approx 1\,\mathrm{cm}^{-1}$ ($k = 10^{-5}$ or 10 ppm for 100nm) and less. To measure such low values, the photothermal deflection method is used [5, 6]. In Fig. 3, the setup is depicted. The sample (coated layer on a glass substrate) is placed in a cuvette filled with CCl_4, which is mounted on an x–y stage. The choppered pump beam (45 mW laser at 685 nm, placed on a z stage) passes the sample perpendicularly and, due to the absorption in the layer, heat is generated. This results in a temperature gradient in the CCl_4 and thus in a gradient of the refractive index ($dn/dT_{\mathrm{CCl_4}} = 6.4 \cdot 10^{-4}$). A probe beam (5 mW laser at 633 nm) passes the sample parallel near the surface, is deflected by the gradient of the refractive index, and the deflection angle is measured with a 4-quadrant photo diode and a lock-in amplifier. The position of the pump and the probe beam to the sample is very critical and all parameters (x, y, and z) should be optimized to get a maximum in the signal.

The result for such a measurement (here exemplarily for Al_2O_3) is shown in Fig. 4. The thickness (deposition rate) and the refractive index are measured with an ellipsometer (633 nm). It can be seen that the deposition rate decreases with increasing the oxygen flow or rather the partial pressure. The refractive index shows a fast decrease and then stays constant with increasing the oxygen flow. The absorption is measured with the photothermal deflection and the curve looks similar to the theoretical one in Fig 2. With no oxygen in the chamber, the absorption is relatively high and decreases with a small

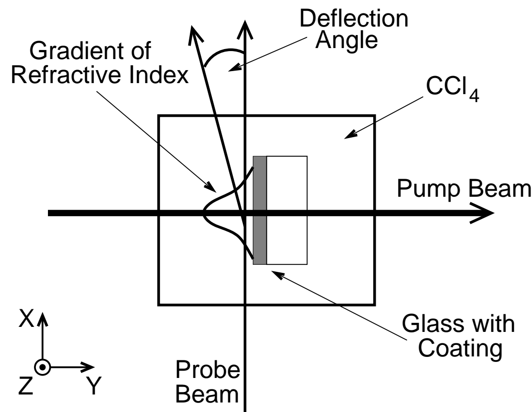

Fig. 3: Schematic view of the photothermal deflection measurement method.

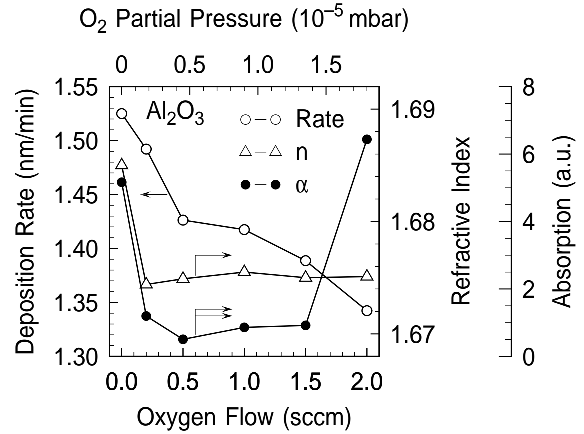

Fig. 4: Deposition rate, refractive index, and absorption depending on the oxygen partial pressure.

amount of oxygen. But with a higher oxygen flow the absorption starts to increase again. A minimum in the absorption can be found where the coating process should operate.

4. Measurement Results

The reactive ion-beam sputter deposition system used for these experiments has an inductively coupled plasma (ICP) ion-beam source and a water-cooled target holder for four targets. The following results are achieved with an ion-beam current of I_{B}=40 mA, a beam voltage of U_{B}=1000 V, and an acceleration voltage of U_{B}=120 V. Four different materials have been examined and the substrate position has been optimized.

4.1 Oxygen dependent absorption for different materials

For four different materials (SiO_2, Al_2O_3, Y_2O_3, and Ta_2O_5), the measurement of the deposition rate, the refractive index and the absorption has been performed as described before (see Fig. 4). The absorption of the different materials depending on the oxygen partial pressure can be seen in Fig. 5. Every material shows the same behavior, at low and high oxygen partial pressures a high absorption, and at a certain pressure a minimum. The difference of the value and the position varies with the material and also can be influenced by parameters like e. g. ion-beam current or total pressure.

In Fig. 6, the spectral refractive index of the four examined materials is shown. This values were measured and extracted with spectral ellipsometry [7] at L.O.T.-Oriel GmbH & Co KG.

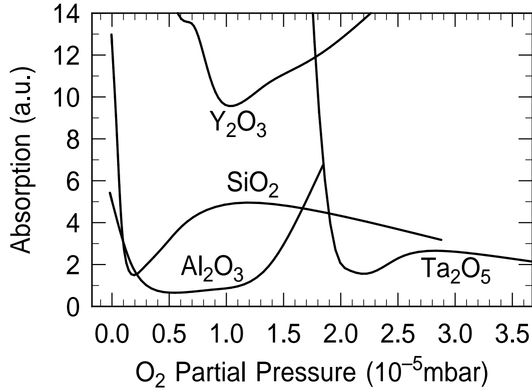

Fig. 5: Absorption over oxygen partial pressure for different materials.

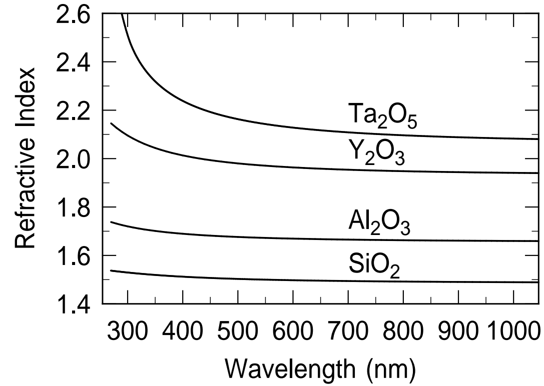

Fig. 6: Refractive index over wavelength for different materials determined with spectral ellipsometry.

4.2 Substrate position

In this section, the substrate position has been changed to optimize the coating parameters. For these experiments, only one material (Ta_2O_5) has been examined.

In Fig. 7, a schematic view of the system configuration in the x–z plane is shown. The Ar^+ ion beam strikes the target under an angle of 55° and the target normal is tilted 5° against the normal of the substrate. The reflected Ar^+ ions have about the same angle like the incident ions. The sputtered material, in contrast, leaves the target more or less perpendicular.

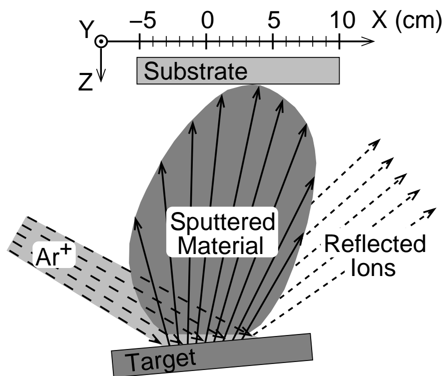

Fig. 7: Schematic view of the sputter system in the x–z plane.

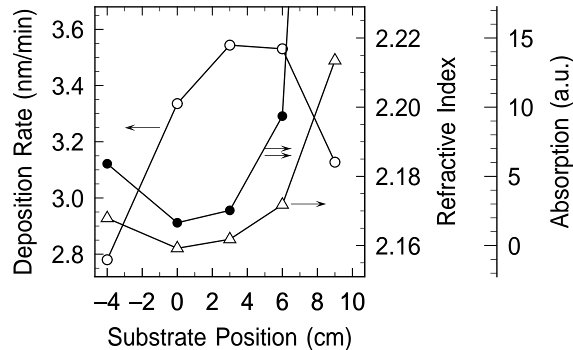

Fig. 8: Deposition rate, refractive index, and absorption depending on the substrate position for Ta_2O_5.

In Fig. 8, the results for different substrate positions on the x axis are shown. With increasing the x position the deposition rate increases and shows a plateau between 2 and 6 cm, in this region the homogeneity is quite good (±1.5 %). The absorption has a

minimum between -1 and 3 cm and increases rapidly to higher x values due to the disturbance of the reflected Ar^+ ions in this range. Also the refractive index behaves like the absorption and has for $x \leq 6$ cm a quite constant value with a deviation of less than ± 0.25 %. This results point out that the system is well designed and there is a window for the substrate position which shows a low absorption and a good homogeneity.

In Fig. 9, the system is shown in the y–z plane; the Ar^+ ion beam enters the plane from viewers point. The normal of the substrate can be varied against the normal of the target, at an angle of $\alpha = 0$, substrate and target are parallel in the y–z plane. There are three faces indicated. For example face a (parallel to the substrate) can be the facet of a laser, so face b and c (perpendicular to the substrate) are the n and p contact of the laser.

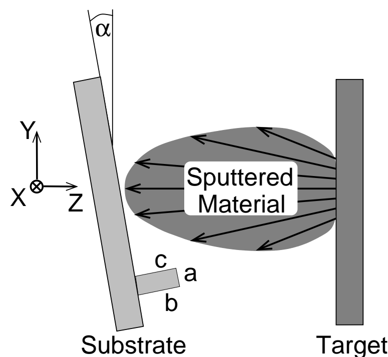

Fig. 9: Schematic view of the sputter system in the y–z plane.

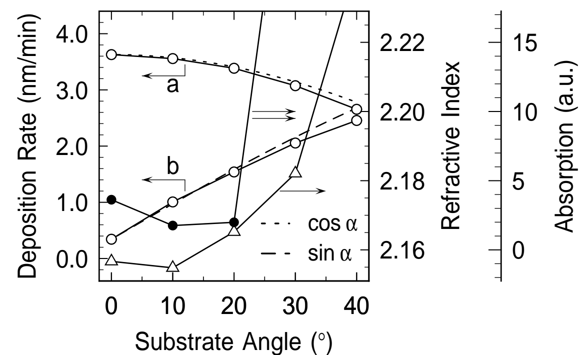

Fig. 10: Deposition rate, refractive index, and absorption depending on the substrate angle for Ta_2O_5.

Figure 10 shows, that the deposition rate of the face a decreases with increasing substrate angle, just like a cosine function; the face b, in opposite, increases just like a sine function. Face c decreases and at 10° no material is deposited anymore (not shown in the graph). In such a case one contact of a laser is not deposited and can be mounted without loosing thermal conductivity. The absorption shows a minimum in the range of 0° to 20° but beyond this angle it increases rapidly. The refractive index has a low deviation of ± 0.3 % in this low-angle range. This results show, that the angle of the substrate can be varied in the range of 0° to 20° without decreasing the quality of the coating but with preventing one face, e. g. of a laser, from getting deposited.

5. Conclusion

By using the photothermal deflection method, the absorption of coated layers has been measured and the process parameters have been optimized. During the sputter process, oxygen has to be introduced into the chamber to achieve stoichiometric and dense layers.

For four different materials, the optimized amount of oxygen to get minimum absorption has been figured out. The substrate position has been varied and there is range with minimum absorption and a good homogeneity. Also the substrate angle can be changed in a small range to prevent the perpendicular face from being coated and, simultaneous, keep a low value of the absorption.

References

[1] F.R. Flory, *Thin films for optical systems*, vol. 49. New York: Dekker, 1. ed., 1995.

[2] M. Tilsch, *Eigenschaften ionenstrahlgesputterter optischer SiO_2- and TiO_2- Schichten bei unterschiedlichen Wachstumsbedingungen und Veränderungen bei thermischer Nachbehandlung*. PhD thesis, University of Darmstadt, Darmstadt, Germany, Jan. 1997.

[3] J. Becker, "Ion-beam sputtering," ch. 7 in *Handbook of optical properties. Volume I: Thin films for optical coatings,* R.E. Hummel and K.H. Guenther (Ed.), Boca Raton: CRC Press, pp. 189–212, 1995.

[4] D.T. Wei, H.R. Kaufman, and C.-C. Lee, "Ion beam sputtering," ch. 6 in *Thin films for optical systems,* F.R. Flory (Ed.), New York: Marcel Dekker, pp. 133–201, 1995.

[5] W.B. Jackson, N.M. Amer, A.C. Boccara, and D. Fournier, "Photothermal deflection spectroscopy and detection," *Appl. Optics*, vol. 20, no. 8, pp. 1333–1344, 1981.

[6] E. Welsch and D. Ristau, "Photothermal measurements on optical thin films," *Appl. Optics*, vol. 34, no. 31, pp. 7239–7253, 1995.

[7] D.E. Aspnes, "The accurate determination of optical properties by ellipsometry," ch. 5 in *Handbook of optical constants of solids,* E.D. Palik (Ed.), Orlando: Academic Press, pp. 89–112, 1985.

External-Cavity Tapered Semiconductor Ring Lasers

Frank Demaria

Laser operation of a tapered semiconductor amplifier in a ring-oscillator configuration is presented. In first experiments, 1.75 W time-average optical output power has been achieved at room temperature. Results for different configurations and feedback ratios are shown and compared to the output characteristics of the same device in a master-oscillator power-amplifier configuration. Dynamical analysis of the optical signal reveals passively mode-locked operation. The repetition rate of the generated pulses of 214 MHz is determined by the round-trip time of 4.67 ns. Fourier-transformation of the frequency signal to the time-domain yields a pulse-duration of less than 80 ps.

1. Introduction

Tapered travelling-wave laser-amplifiers usually are part of a master-oscillator power-amplifier setup. Typical for such devices is the very low reflectivity of the facets, which is in the range of 10^{-4}. Besides the use of anti-reflection coatings, bent ridge-waveguides, which hit the facet under a tilt angle with respect to the normal, can be utilized to lower the residual reflectivity [1]. On the other hand, the same kind of device is often designed as a laser oscillator with a linear resonator, by applying mirrors in the form of coatings with higher reflectivities [2], DBR-mirrors [3][4], or by external mirrors which can be realized also in a wavelength selective version, using a grating in order to make the laser tunable [5]. Beyond that, the use of a tilted-stripe taveling-wave optical amplifier in a external-cavity ring laser setup has already been demonstrated [6].

Instead of a traveling-wave optical amplifier with stripe-geometry, we used a device having a tapered gain region in a ring laser setup. The astigmatism, or with other words, the position of the internal virtual source of a tapered amplifier strongly depends strongly on its saturation. With the setup presented here, an image of the internal virtual source is projected onto the input facet of the amplifier, which acts as a spatial mode filter. With a suitable alignment, only the emission of the highly saturated amplifier is efficiently coupled back into the amplifier. By that way, a saturable absorption mechanism is established. It is important to note, that this is only possible for the ring-resonator configuration of a tapered amplifier but not for any kind of linear resonator nor for stripe-geometry amplifiers in a ring resonator. The described behaviour is quite analog to kerr-lens mode locking (KLM) which is commonly utilized for the passive mode locking of solid-state lasers.

2. Device and Setup

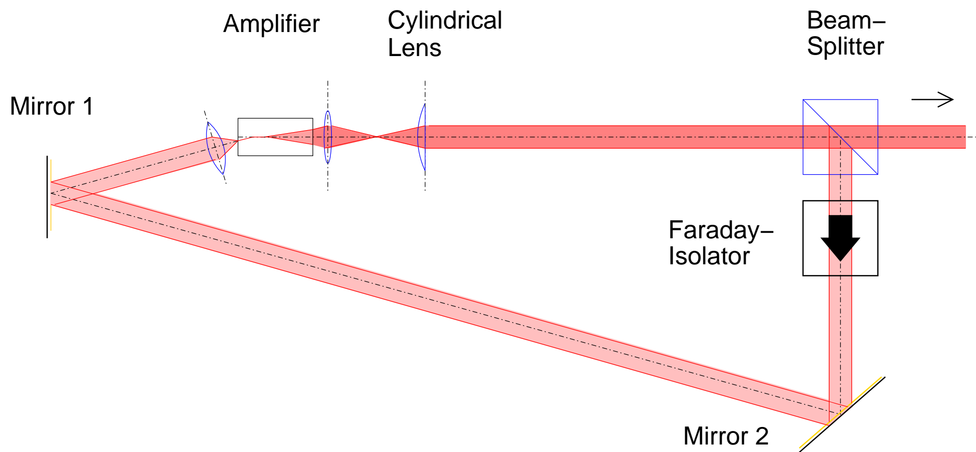

Fig. 1: Setup of the ring oscillator configuration with a tapered semiconductor laser amplifier. The aspherical lenses at the left ($f = 4.5$ mm) and at the right side ($f = 6.5$ mm) of the amplifier are collimating the beam in the fast-axis direction, which is pependicular to the drawing plane. The cylindrical lens with a focal length of 100 mm is necessary to compensate the astigmatism of the amplifer and to collimate the beam in the slow-axis direction.

Figure 1 shows the schematic diagram of the ring-oscillator setup. The laser active device is a 2.5 mm long tapered semiconductor amplifier with a 500 µm-long and 3.5 µm-wide ridge waveguide. The maximum gain of the amplifier at room temperature is at 920 nm. The geometrical round-trip length of the resonator is 1260 mm. By a Faraday isolator, clockwise circulation is ensured, which is essential, as only the broad output facet of the amplifier, which is orientated to the right side in Fig. 1, can withstand high optical powers of several watts, due to its width of 210 µm. The laser light which is emitted from this facet is collimated in the direction of the fast axis, which is perpendicular to the drawing plane, by a collimating lens system with a focal length of 6.5 mm and a high numerical aperture of 0.615. Because of the astigmatism of the tapered gain region, the vertically collimated beam is convergent in the horizontal direction and forms a intermediate focus there. At an adequate distance right after the intermediate focus, a 100 mm focal length cylindrical lens is located, in order to collimate the beam also in the horizontal direction. With a beam-splitter a 16.5 % fraction of the optical power is branched off in order to be fed back into the amplifier. The reflected beam is passing through a Faraday isolator and by two gold mirrors directed versus the input facet, to which the beam is focussed by a 4.5 mm-focal-length aspherical lens with a numerical aperture of 0.55. The bent ridge wavegide in the input section of the device meets the input facet under 4.5°, thus the incident angle of the beam has to be 15° due to the waveguide's high effective refractive index.

One severe practical problem is regarding the alignment of the optical components. Namely, that the beam can not be observed inside the resonator with a detector card, camera or scanning-slit system. With such a optical barrier inside the resonator, the amplifier

will switch to its non-feedback operation mode, where amplified spontaneous emission is dominant and the beam propagation is completely different compared to laser operation. In order to overcome that problem, we first coupled a signal from a master-oscillator into the amplifier, to perform an alignment and suitable collimation of the emitted beam. All optical components except Mirror 1 can be positioned and adjusted by that way. In a final step, the additon of Mirror 1 and its alignment can be performed easily.

3. Experimental Results

3.1 Quasi-statical behaviour

At first, the optical output of the ring oscillator was measured with a thermophile power detector. Despite this kind of detector is quite reliable for the measurement of optical powers of several watts, it has a multi second response time, therefore the optical powers which are presented in this subsection should always be mentioned to be long time averaged. Additionally, in Subsection 3.2 the results of the experimental investigation of the dynamical behavior will be presented.

As the threshold current depends on the feedback ratio, this can be affected by the use of beam-splitters with various splitting ratios. Figure 2 shows that for two different reflection ratios of 16.5 % and 4 %. For the lower reflectivity, we observed a less stable operation that led to deviatons in the corresponding graph. The tapered amplifer has

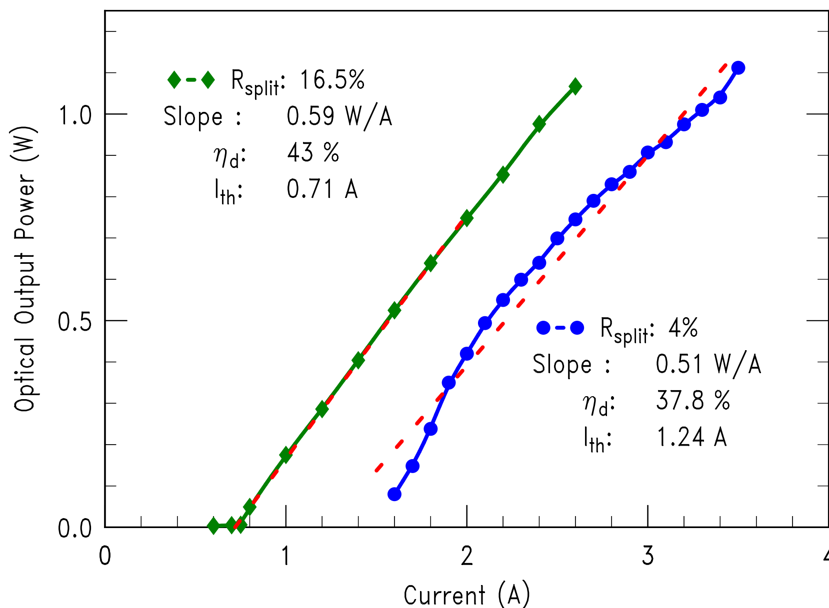

Fig. 2: Output characteristics with different beam splitting reflectivities.

also been characterized in a master-oscillator power-amplifier setup, where the emission of a single-mode ridge-waveguide laser has been used as a input signal. In Fig. 3 this

output characteristics with an optical input power of 10 mW is compared to that of the ring-oscillator setup. To demonstrate that the feedback was not established by any kind of a parasitical linear resonator, we interrupted the feedback path at different locations and measured the optical output with no feedback, which was constantly low in all cases. The corresponding graph in Fig. 3 reveals the difference to the case with feedback.

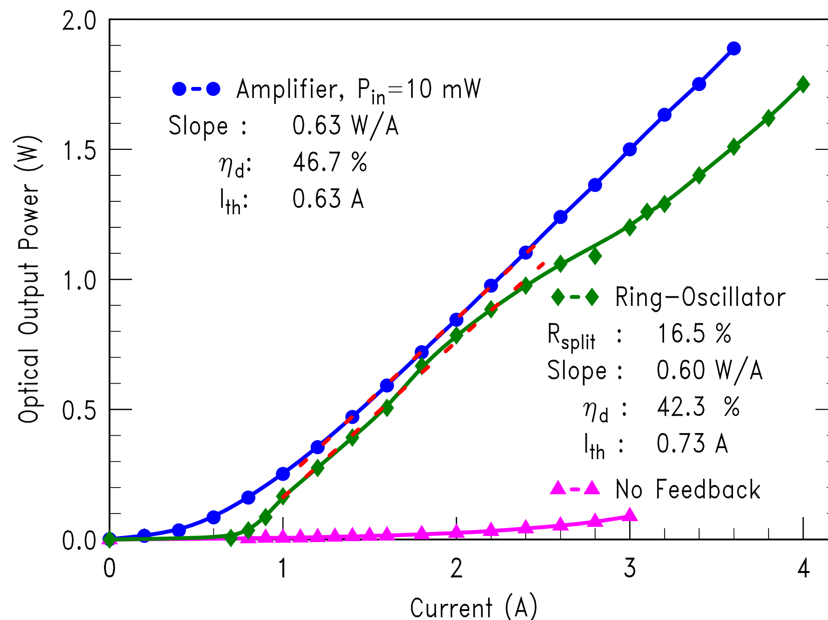

Fig. 3: Comparison of the optical output characterisics of the tapered laser in a master-oscillator power amplifier setup, and the same device in a ring laser configuration.

3.2 Dynamical behaviour

Because of the anticipated high repetiton rate and low pulse duration time, the time dependency can not simply be observed by a normal oscilloscope. Furthermore the lack of a trigger signal makes this measurement even more difficult. To decide whether the laser is runnig in constant-wave or pulsed mode, the electrical signal from a photo diode was analized with respect to its spectral behavior.

As Fig. 4 shows, this analysis reveals a distinct equidistant spectral coverage with harmonics over the whole measurement range from 0 to 20 GHz. The limitation to 20 GHz is due to the measurement-setup. For this measurement, the averaged optical power was 1.05 W at a current of 3.5 A. Harmonics can be observed over a wide range of different currents. The adjustment of the resonator was performed in order to achieve a high averaged optical power and distinct harmonics over the whole spectral range at the same time. Generally, the distribution and intensity of the harmonics depends on the adjustment of the feedback coupling. The separation of the different harmonics of 214 MHz corresponds to an optical round-trip length of 1.40 m. The spectral signal is Fourier-transformed to

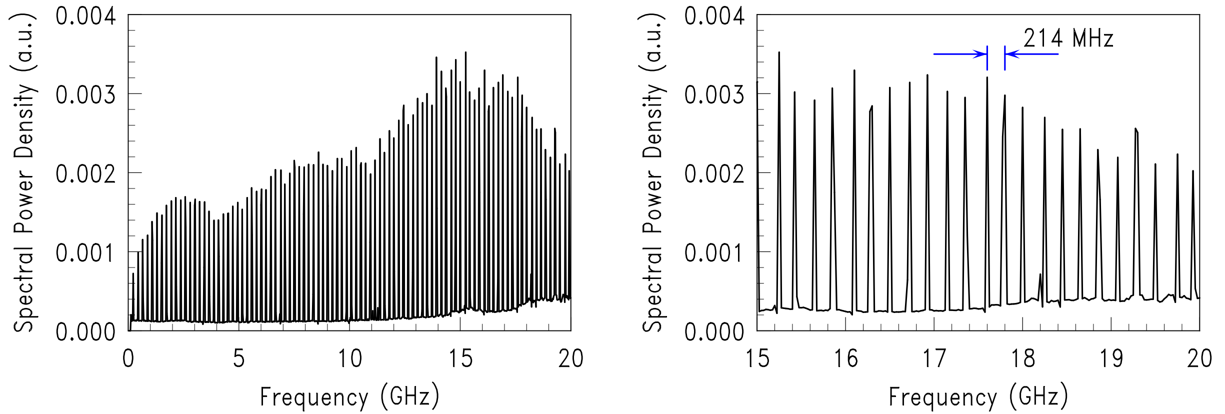

Fig. 4: Measured electrical spectrum of the time dependend ring-laser signal. The time averaged optical power is 1.05 W at a current of 3.5 A.

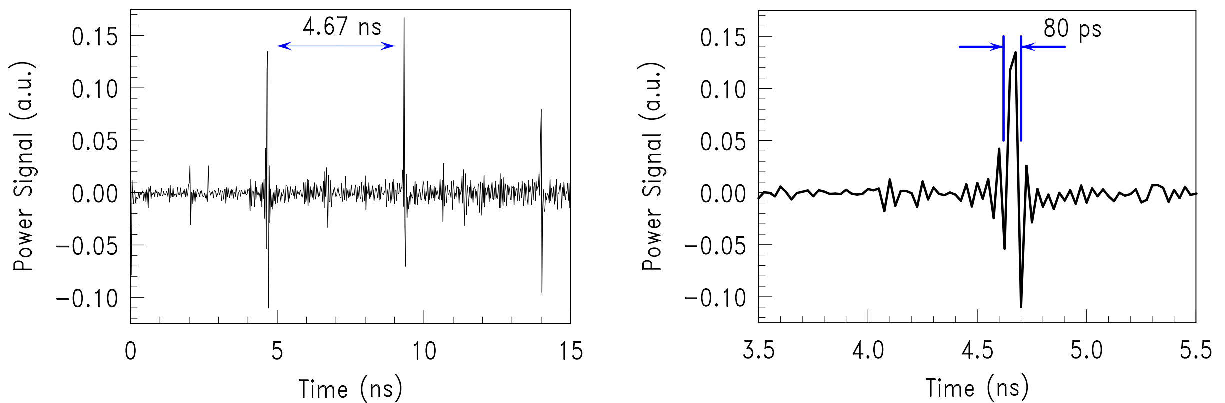

Fig. 5: Time signal reproduction by Fourier-transformation of the electrical signal from Fig. 4

the time domain numerically. The result is given in Fig. 5. The distinct peaks have a repetition time of 4.67 ns and a duration of less than 80 ps.

4. Conclusion and Discussion

For the first time, the use of a tapered semiconductor laser-amplifier, in a quite simple setup as a ring-oscillator and its capability of generating pico-second laser pulses by passive modelocking is demonstrated. The presented characteristics should be regarded as “first results”. From the averaged optical output power of 1.05 W, an amplified spontaneous emission power of 0.15 W and a duty cycle of less than 1:58, the peak power can be estimated to be at least 50 W, considering the fact that the measured pulse duration is limited by the bandwidth of the employed photo-diode. As a limiting factor for the real pulse duration time, the dispersion which is introduded by the amplifier should be mentioned and possibly compensated in a more improved setup. Together with the high spatial beam quality of tapered laser devices, the high peak power makes such a system an interesting laser source for the generation of pulses and second harmonic generation.

References

[1] M. Mundbrod, “Ridge-waveguide lasers with tiltet facets,” *Annual Report 2003, Dept. of Optoelectronics, University of Ulm*.

[2] H. Wenzel, B. Sumpf, G. Erbert, “High-brightness diode lasers”, *C. R. Physique*, vol. 4, pp. 649–661, 2003.

[3] D. Mehuys, S. O’Brien, R.J. Lang, A. Hardy, D.F. Welch ”5 W, diffraction-limited, tapered-stripe unstable resonator semiconductor laser”, *Electron. Lett.*, vol. 30, no. 22, pp. 1855–1856, 1994.

[4] S.R. Semic, G.A. Evans, T.M. Chou, J.B. Kirk, J.N. Walpole, J.P. Donelly, C.T. Harris, L.J. Missaggia, “Single Frequency 1550-nm AlGaInAs-InP Tapered High-Power Laser With a Distributed Bragg Reflector”, *IEEE Photon. Technol. Lett.*, vol. 14, no. 7, pp. 890–892, 2004

[5] S. Morgott, P. Charzan, M. Mikulla, M. Walther, R. Kiefer, R. Kiefer, J. Braunstein, G. Weimann, ”High-power near-diffraction-limited external cavity laser, tunable from 1030 to 1085 nm”, *Electron. Lett.*, vol. 34, no. 6, pp. 558–559, 1998.

[6] En T. Peng, C. B. Su,”Properties of an external-cavity traveling-wave semicondudtor ring laser”, *Opt. Lett.*, vol. 17, no. 1, 1992.

Ph.D. Theses

1. Marcus Andreas Scherer,
   Prozesstechnologie für GaN-basierende Leuchtdioden,
   January 2004.

2. Irene Ecker,
   Molekularstrahlepitaxie GaAs-basierender Mischungshalbleiter für 1300 nm-nahe Laserdiodenemission,
   January 2004.

3. Matthias Golling,
   Molekularstrahlepitaxie vertikal emittierender InGaAs-Laser-Strukturen mit periodischer Gewinnstruktur,
   March 2004.

4. Jürgen Joos,
   Technologien zur Realisierung langwellig emittierender Vertikallaserdioden,
   July 2004.

Diploma and Master Theses

1. Peter Brückner,
   Einfluß der Prozeßparameter beim epitaktischen Überwachsen von strukturierten GaN-Schichten mittels MOVPE,
   Diploma Thesis, Optoelectronics Department, January 2004.

2. Antonia Reeg,
   Aufbau eines Empfangsmoduls zur optischen Freiraumdatenkommunikation zwischen Fahrzeugen,
   Diploma Thesis, Optoelectronics Department, February 2004.

3. Christof Jalics,
   Entwicklung und Untersuchung von Prozessen zur Herstellung von VCSELn mit dielektrischen Oberflächengittern zur Polarisationskontrolle,
   Diploma Thesis, Optoelectronics Department, March 2004.

4. Markus Thal,
   Erstellung eines Messplatzes zur Bestimmung der Zuverlässigkeit von PIN-Photodioden für die optische Datenübertragung,
   Diploma Thesis, Optoelectronics Department, March 2004.

5. Martin Feneberg,
   Untersuchung von VCSELn mit einem dielektrischen Oberflächengitter
   Diploma Thesis, Optoelectronics Department, May 2004.

6. Michael Schumann,
   Prozessierung und Charakterisierung von kurzwelligen Laserdioden im Materialsystem AlGaAs,
   Diploma Thesis, Optoelectronics Department, May 2004.

7. Heiko Paul,
   n- und p-Dotierung von AlGaN mittels MOVPE,
   Diploma Thesis, Optoelectronics Department, July 2004.

8. Hayssam El- Hajj,
   Bended Waveguide Semiconductor Laser Amplifiers,
   Master Thesis, Optoelectronics Department, August 2004.

9. Onur Atilla,
   Minimization of the Absorption of Optical Coatings Using Photothermal Deflection Spectroscopy,
   Master Thesis, Optoelectronics Department, August 2004.

10. Tobias Fischer,
    Transistor- und Diodenmodelle für Hochspannungs-CMOS-Prozesse mit Trenchisolierung,
    Diploma Thesis, Optoelectronics Department, August 2004.

11. Lutz Stöferle,
    Untersuchung und Optimierung von Komponenten eines bidirektionalen optischen Übertragungssystems bei 850 nm Wellenlänge,
    Diploma Thesis, Optoelectronics Department, December 2004.

Semester Projects

1. Johanna May,
   Internal quantum efficiency of thin film solar cells on wafer and glass substrates — Measurement and simulation,
   May 2004,

2. Lutz Stöferle,
   Untersuchung zu temperaturabhängigen Eigenschaften von Metall-Halbleiter-Metall (MSM)-Photodioden,
   June 2004,

3. Thomas Wunderer,
   Optimierung der Montagetechnik GaN-basierender Laserdioden,
   August 2004

4. Joachim Hertkorn,
   Einsatz von Vertikal emittierenden Laserdioden in der optischen Partikeldetektion,
   November 2004,

5. Gregor Wendrock,
   Berechnungen zur optischen Leistungseinkopplung von Vertikallasern in Gradientenindexfasern,
   December 2004

Talks

[1] P. Brückner, F. Habel, and F. Scholz, “Epitaxie von defektreduzierten GaN Schichten”, *19. DGKK-Workshop Epitaxie von III/V-Halbleitern*, Freiburg i. Br. Germany, Dec. 2004.

[2] E. Gerster, “Intra-Cavity Frequency-Doubled Semiconductor Disk Laser Based on GaAsSb/GaAs”, ETH Zürich, Switzerland, Dec. 2004.

[3] C. Kirchner, P. Brückner, and F. Scholz, “Wachstum hoch Al-haltiger AlGaN- und AlN-Schichten mit MOVPE”, *19. DGKK-Workshop Epitaxie von III/V-Halbleitern*, Freiburg i. Br. Germany, Dec. 2004.

[4] R. Michalzik, “High-power semiconductor lasers: from horizontal to vertical cavities”, Center for Photonic Materials & Devices, Chonnam National University, Gwangju, Korea, June 2004.

[5] R. Michalzik, “Recent topics in short-wavelength VCSEL research”, Gwangju Institute of Science and Technology (GIST), Dept. of Materials Sci. & Eng., Gwangju, Korea, June 2004.

[6] R. Michalzik, “Ulm University and the cleanroom of the Faculty of Engineering Science”, Dongshin University (DSU), School of Health Science and Welfares, Dept. of Biomedical Engineering, Naju, Chonnam, Korea, June 2004.

[7] R. Michalzik, “VCSEL based optical interconnects”, Gwangju Institute of Science and Technology (GIST), Dept. of Information & Communications, Gwangju, Korea, June 2004.

[8] R. Michalzik, “Modern semiconductor lasers and communication applications”, *Physics Colloquium* of El Minia University, Minia, Egypt, Feb. 2004.

[9] R. Michalzik, “Vertical-cavity surface-emitting laser diodes for optical interconnects” (in German), *Technical Physics Seminar* of Würzburg University, Würzburg, Germany, Jan. 2004.

[10] B. Neubert, F. Habel, P. Brückner, F. Scholz, T. Riemann, and J. Christen, “Elektrolumineszenz von GaInN-Quantenfilmen auf Facetten von selektiv gewachsenen GaN-Streifen”, *19. DGKK-Workshop Epitaxie von III/V-Halbleitern*, Freiburg i. Br. Germany, Dec. 2004.

[11] J.M. Ostermann, “Current Research at the Optoelectronics Department, University of Ulm,” Chalmers University, Group Seminar of the Photonics Lab, Gothenborg, Sweden, Aug. 2004.

[12] J.M. Ostermann, P. Debernardi, Å. Haglund, G.P. Bava, A. Larsson, R. Michalzik, "VCSELs with an integrated grating relief for single-polarization and single-mode emission," *European Semiconductor Laser Workshop*, Särö, Sweden, Aug. 2004.

[13] J.M. Ostermann, "Diffractive Optics for Polarization Control of Vertical-Cavity Surface-Emitting Lasers (VCSELs)," Westfälische Wilhelms-Universität Münster, Institut für angewandte Physik, Group Seminar of the AG Nichtlineare Optik und Quantenoptik, Münster, Germany, Nov. 2004.

[14] F. Rinaldi, "Epitaxy and Characterization of Semiconductor Disk Lasers", *Deutscher MBE-Workshop*, Physikalisch-Technische Bundesanstalt, Braunschweig, Germany, Oct. 2004.

[15] F. Scholz, "Crystalline interfaces and Strain in Compound Semiconductors", Workshop of Graduiertenkolleg *"Interfaces in Crystalline Materials"*, Ellwangen. Feb. 2004.

[16] F. Scholz, F. Habel, and P. Brückner, "Defektreduzierung in GaN für optoelektronische Anwendungen", Seminar talk Uni/IAF Freiburg, June 2004.

[17] F. Scholz, F. Habel, and P. Brückner, "Preparation of GaN quasi substrates by HVPE and MOVPE", Aixtron User Meetings, Hsinshu and Tainan, Taiwan, Sept. 2004.

[18] F. Scholz, "Optoelectronics in Germany - an attempt to describe the current situation", Talk at Wuhan University of Science & Engineering, China, Oct. 2004.

[19] F. Scholz, "Studies at the faculty of Engineering at Ulm University", Talk at Wuhan University of Science & Engineering, China, Oct. 2004.

[20] F. Scholz, F. Habel, and P. Brückner, "Defect reduction in GaN structures on sapphire", OSRAM OS GaN Workshop Schloss Hohenkammer, Nov. 2004.

[21] F. Scholz, "GaN in neuen Spektralbereichen: Materialtechnische Herausforderungen und Grenzen", 2. Fachtagung *Innovative Beleuchtung*, Düsseldorf, Nov. 2004.

[22] P. Unger, "Halbleiter-Scheibenlaser", Ferdinand-Braun-Institut für Höchstfrequenztechnik (FBH), Berlin , May 2004.

[23] P. Unger, "Semiconductor Disk Lasers", Bookham Laser Enterprise, Zurich, Switzerland, July 2004.

[24] P. Unger, "Optically Pumped Semiconductor Disk Lasers", Emerging Technologies in Optical Sciences (ETOS) 2004, Cork, Ireland, July 2004.

[25] P. Unger, "Optically Pumped Semiconductor Disk Lasers", Université de Neuchâtel, Neuchâtel, Switzerland, Dec. 2004.

Publications and Conference Contributions

[1] C. Eichler, D. Hofstetter, W.W. Chow, S. Miller, A. Weimar, A. Lell, and V. Härle, "Microsecond time scale lateral-mode dynamics in a narrow stripe InGaN laser", *Applied Physics Letters*, vol. 84, pp. 2473–2475, 2004.

[2] C. Eichler, S.S. Schad, F. Scholz, S. Miller, A. Leber, A. Lell, and V. Härle, "Time Dependent Modal Behaviour of InGaN-based laser diodes", *International Workshop on Nitride Semiconductors, IWN 2004*, Pittsburgh, PA, USA, July 2004.

[3] P. Gerlach, M. Peschke, and R. Michalzik, "High-frequency performance optimization of DFB laser integrated electroabsorption modulators", in Proc. *Semiconductor and Integrated Optoelectronics Conf., SIOE 2004*, paper 41. Cardiff, Wales, UK, Apr. 2004.

[4] E. Gerster, S. Menzel, and P. Unger, "Intra-cavity frequency-doubled semiconductor disk laser based on GaAsSb/GaAs," *European Semiconductor Laser Workshop 2004*, Särö, Sweden, Sep. 2004.

[5] F. Habel, P. Brückner, and F. Scholz, "Marker layers for the development of a multistep GaN FACELO process", *12th Int'l Conference on Metal Organic Vapor Phase Epitaxy, ICMOVPE XII*, Lahaina, Hawaii, USA, *J. Crystal Growth*, vol. 272, pp. 515–519, 2004.

[6] F. Habel, P. Brückner, J.D. Tsay, W.Y. Liu, F. Scholz, D. Schmitz, A. Alam, and M. Heuken, "Hydride vapor phase epitaxial growth of thick GaN layers with improved surface flatness", *International Workshop on Nitride Semiconductors, IWN 2004*, Pittsburgh, PA, USA, July 2004, *phys. stat. sol. (c)* DOI: 10.1002, 2005.

[7] R. Michalzik, "Vertical-cavity surface-emitting lasers for optical interconnects" (invited), in Proc. *XXIV Conf. on Solid State Physics and Materials Science* of the Egyptian Materials Research Society, *Eg-MRS 2004* & Workshop on *Photonic Materials and Optoelectronic Devices*, p. 23. Safaga, Red Sea, Egypt, Febr. 2004.

[8] R. Michalzik, J.M. Ostermann, P. Debernardi, C. Jalics, A. Kroner, M. Feneberg, and M. Riedl, "Polarization-controlled monolithic oxide-confined VCSELs" (invited), in *Micro-Optics, VCSELs and Photonic Interconnects*, H. Thienpont, K.D. Choquette, M.R. Taghizadeh (Eds.), Proc. SPIE 5453, pp. 182–196, 2004.

[9] R. Michalzik, K.J. Ebeling, M. Kicherer, F. Mederer, R. King, H. Unold, and R. Jäger, "High-performance VCSELs for optical data links", in *High-Performance Backbone Network Technologies*, N. Yamanaka (Ed.), pp. 1005–1013. New York: Marcel Dekker, Inc., 2004. Previously published in *IEICE Trans. Commun.*, vol. E84-B, pp. 1255–1264, 2001. Also published in *IEICE Trans. Electron.*, vol. E84-C, pp. 629–638, 2001.

[10] B. Neubert, F. Habel, P. Brückner, F. Scholz, T. Riemann, and J. Christen, "Electroluminescence from GaInN quantum wells grown on non-(0001) facets of selectively grown GaN stripes", *MRS Fall Meeting 2004*, paper E11.32., Boston, MA, USA, Nov. 2004, accepted for publication in *MRS Symp. Proc. GaN, AlN, InN, and Their Alloys*, 2005.

[11] J.M. Ostermann, P. Debernardi, C. Jalics, A. Kroner, M. Feneberg, M. Riedl, and R. Michalzik, "Monolithic polarization control of multimode VCSELs by a dielectric surface grating", in *Vertical-Cavity Surface-Emitting Lasers VIII*, C. Lei and S.P. Kilcoyne (Eds.), Proc. SPIE 5364, pp. 201–212, 2004.

[12] J.M. Ostermann, P. Debernardi, C. Jalics, M. Feneberg, A. Kroner, M.C. Riedl, M. Golling, and R. Michalzik, "High single-mode power, monolithic polarization-controlled oxide-confined grating relief VCSELs", in Proc. *19th IEEE Int.'l Semicond. Laser Conf.*, pp. 109–110. Kunibiki Messe, Matsue-shi, Simane Pref., Japan, Sept. 2004. For corrections see URL http://www-opto.e-technik.uni-ulm.de/forschung/ram/pub/islc2004.html .

[13] M. Peschke, P. Gerlach, B. Saravanan and B. Stegmüller, "Thermal crosstalk in integrated laser-modulators", IEEE Photon. Technol. Lett., vol. 16, no. 11, pp. 2508–2510, 2004.

[14] M. Peschke, B. Saravanan, C. Hanke, T. Knödl, and B. Stegmüller, "Investigation of the capacitance of integrated DFB-EAMs with shared active layer for 40 GHz bandwidth", in Proc. *IEEE Lasers and Electro-Opt. Soc. Ann. Meet., LEOS 2004*, pp. 673–674. San Juan, Puerto Rico, Nov. 2004.

[15] H. Roscher and R. Michalzik, "Toward redundant 2-D VCSEL arrays for optical datacom", in *Micro-Optics, VCSELs and Photonic Interconnects*, H. Thienpont, K.D. Choquette, M.R. Taghizadeh (Eds.), Proc. SPIE 5453, pp. 170–181, 2004.

[16] S.S. Schad, B. Neubert, J. Brüning, C. Eichler, F. Habel, F. Scholz, P. Unger, and D. Hofstetter, "Absorption in InGaN-on-sapphire LED-structures: Comparison between the Photocurrent Measurement Method (PMM) and the Photothermal Deflection Spectroscopy" in *Light Emitting Diodes: Research, Manufacturing, and Applications*, E.F. Schubert (Ed.), Proc. SPIE 5336, 2004.

[17] S.S. Schad, B. Neubert, C. Eichler, M. Scherer, F. Habel, M. Seyboth, F. Scholz, D. Hofstetter, P. Unger, W. Schmid, C. Karnutsch, and K. Streubel, "Absorption and light scattering in GaN-on-sapphire- and AlGaInP-based light-emitting-diodes", *IEEE J. Lightwave Technol.*, vol. 22, pp. 2323–2332, 2004.

[18] M. Stach, F.I. Pomarico, D. Wiedenmann, and R. Michalzik, "High-performance low-cost optical link at 850 nm with optimized standard singlemode fiber and high-speed singlemode VCSEL", in Proc. *30th Europ. Conf. on Opt. Commun., ECOC 2004*, vol. 3, pp. 712–713. Stockholm, Sweden, Sept. 2004.

[19] P. Unger "Optically Pumped Semiconductor Disk Lasers", Proc. *Emerging Technologies in Optical Sciences (ETOS) 2004*, Page 103, July 26–29. Cork, Ireland, 2004.

[20] P. Unger "Semiconductor Lasers", in *Lasers and current optical techniques in biology*, pp. 77–95, edited by G. Palumbo and R. Pratesi, *Comprehensive Series in Photochemistry and Photobiology*, vol. 4, Royal Society of Chemistry (RSC), Cambridge 2004.

[21] K.E. Alameh, K. Eshraghian, S. Ahderom, M. Raisi, M.M.-O. Lee, and R. Michalzik, "Integrated MicroPhotonic broadband smart antenna beamformer", in Proc. *2nd International Workshop on Electronic Design, Test & Applications, DELTA 2004*, pp. 208–212. Perth, Western Australia, Jan. 2004.

[22] K.E. Alameh, K. Eshraghian, S. Ahderom, M. Raisi, M.M.-O. Lee, and R. Michalzik, "MicroPhotonic broadband null steering", in Proc. *The International Conference on Cybernetics and Information Technologies, Systems and Applications: CITSA 2004*, pp. 34–38. Orlando, FL, USA, July 2004.

[23] M. Arizaleta, M. Camarena, H.J. Unold, J.M. Ostermann, R. Michalzik, H. Thienpont, and K. Panajotov, "Optical feedback from extremely short external cavity in VCSEL", in *Micro-Optics, VCSELs and Photonic Interconnects*, H. Thienpont, K.D. Choquette, M.R. Taghizadeh (Eds.), Proc. SPIE 5453, pp. 217–228, 2004.

[24] J. Danckaert, M. Peeters, C. Mirasso, M. San Miguel, G. Verschaffelt, J. Albert, B. Nagler, H. Unold, R. Michalzik, G. Giacomelli, and F. Marin, "Stochastic polarization switching dynamics in vertical-cavity surface-emitting lasers: theory and experiment", *IEEE J. Select. Topics Quantum Electron.*, vol. 10, pp. 911–917, 2004.

[25] P. Debernardi, J.M. Ostermann, G.P. Bava, and R. Michalzik, "Vertical cavity laser with polarization defined by an integrated dielectric grating" (in Italian), in Proc. *XV National Meeting on Electromagnetism*, pp. 305–308. Cagliari, Italy, Sept. 2004.

[26] U. Haboeck, A. Hoffmann, T. Riemann, J. Christen, F. Habel, P. Brückner, and F. Scholz, "Evolution of the Optical Properties in thick HVPE GaN on Sapphire", *International Workshop on Nitride Semiconductors, IWN 2004*, Pittsburgh, PA, USA, paper A11.2, July 2004.

[27] C. Hanke, T. Knödl, B.K. Saravanan, and M. Peschke, "Investigation of the high-frequency performance of monolithic integrated laser-modulators", in Proc. Joint Symposium on Opto- and Microelectronic Devices and Circuits, SODC 2004. Wuhan, China, March 2004.

[28] T. Knödl, C. Hanke, B.K. Saravanan, M. Peschke, R. Schreiner, and B. Stegmüller, "Integrated 1.3 μm InGaAlAs–InP laser-modulator with double-stack MQW layer structure," in *Integrated Optics and Photonics Integrated Circuits,* G.C. Righini, S. Honkanen (Eds.), SPIE Proc. 5451, pp. 1–7, 2004.

[29] T. Knödl, C. Hanke, B. Saravanan, M. Peschke, R. Macaluso, and B. Stegmüller, "40 GHz monolithic integrated 1.3 µm InGaAlAs–InP laser-modulator with double stack MQW layer structure", in Proc. *IEEE Lasers and Electro-Opt. Soc. Ann. Meet., LEOS 2004*, pp. 675–676. San Juan, Puerto Rico, Nov. 2004.

[30] H. Lindberg, M. Strassner, E. Gerster, and A. Larsson, "0.8 W optically pumped vertical external cavity surface emitting laser operating CW at 1550 nm," *Electron. Lett.*, vol. 40, no. 10, pp. 601–602, 2004.

[31] S.W.Z. Mahmoud and R. Michalzik, "Oxide confined vertical-cavity surface-emitting laser diodes for optical fiber communications", in Proc. *XXIV Conf. on Solid State Physics and Materials Science* of the Egyptian Materials Research Society, *Eg-MRS 2004* & Workshop on *Photonic Materials and Optoelectronic Devices*, p. 72. Safaga, Red Sea, Egypt, Febr. 2004.

[32] A. Neyer, S. Kopetz, E. Rabe, W.J. Kang, M. Stach, and R. Michalzik, "10 Gbit/s electrical-optical circuit board based on new polysiloxane waveguide technology", in Proc. *30th Europ. Conf. on Opt. Commun., ECOC 2004*, vol. 4, pp. 814–815. Stockholm, Sweden, Sept. 2004.

[33] K. Panajotov, M. Arizaleta, M. Camarena, H. Thienpont, H.J. Unold, J.M. Ostermann, and R. Michalzik, "Polarization switching induced by phase change in extremely short external cavity vertical-cavity surface-emitting lasers", *Appl. Phys. Lett.*, vol. 84, pp. 2763–2765, 2004.

[34] B. Stegmüller, C. Hanke, T. Knödl, M. Peschke, B. Saravanan, P. Gerlach and R. Schreiner, "Integrated DFB laser electro-absorption modulator based on identical MQW-double-stack active layer for high-speed modulation beyond 10 Gbit/s", in Proc. *16th International Conference on Indium Phosphide and Related Materials IPRM 2004*, paper TP-30. Kagoshima, Japan, May 2004.